UNIVERSITY OF BERGEN

Department of Physics and Technology

MASTERS THESIS

Prompt and non-prompt J/ψ cross-sections in proton-proton collisions at $\sqrt{s}$ = 5.02 TeV with ALICE

Author: Jon-Are Sætre

Supervisor: Dieter Röhrich

Co-supervisor: Fiorella Maria Celeste Fionda

June 3, 2019

Abstract

The study presented in this thesis is about the measurement of J/ψ production in proton-proton collisions at center-of-mass energy $\sqrt{s}$ = 5.02 TeV with the ALICE detector at the LHC, with a focus on the separation between prompt J/ψ and non-prompt J/ψ, the latter originated from beauty-hadron decays. Statistics collected during 2017 with the minimum bias trigger ($L_{\rm int}$ = 19.4 nb^{-1}) is the base for the measurement described in this thesis that is performed at central rapidity ($|y| < 0.9$) in the dielectron channel (J/$\psi \rightarrow e^+e^-$). The fraction of non-prompt J/ψ is determined on a statistical basis down to $p_{\rm T}$ = 2 GeV/c, through the use of a maximum-likelihood fit procedure. The value of the non-prompt J/ψ fraction integrated over $p_{\rm T}$ is: $f_{\rm b}(2 < p_{\rm T} < 10{\rm GeV}/c) = 0.103 \pm 0.022({\rm stat}) \pm 0.011$ (syst). The non-prompt J/ψ fraction is further measured in four bins of transverse momentum and compared to similar measurements from other experiments. The non-prompt J/ψ fractions, both $p_{\rm T}$-differential and $p_{\rm T}$-integrated, are combined with the corresponding inclusive J/ψ cross-section measurements, providing prompt and non-prompt J/ψ cross-sections. The $p_{\rm T}$-integrated cross section for prompt J/ψ is: $\sigma_{\rm prompt J/\psi}(2 < p_{\rm T} < 10$ GeV/$c, |y| < 0.9) = 5.09 \pm 0.69$ (stat.) ± 0.49 (syst.) μb. For non-prompt J/ψ the corresponding cross section is: $\sigma_{{\rm J/\psi} \leftarrow h_{\rm B}}(2 < p_{\rm T} < 10\,{\rm GeV}/c, |y| < 0.9) = 0.58 \pm 0.15$ (stat.)± 0.08(syst.) μb. Prompt and non-prompt J/ψ cross-section measurements are finally compared to several QCD-based models.

Acknowledgment

The past five years, and this last one in particular, have been a great learning experience for me.

I would like to thank my supervisor Professor Dieter Röhrich for giving me a chance to work in such an exciting field of physics. To my co-supervisor Fiorella Fionda, I am grateful for the past year. You have been present and eager to help from the very start to the end. For me that really did not know too much about this particular field before, it took time to gain a proper understanding. Ionut Arsene, your answers and comments have been important. I am also thankful for being allowed to be part of the Norwegian analysis group, and also the JPsi2ee PAG group.

I would also like to thank my fellow master students that I have shared office with for the past two years. To the people that were willing to spend some of their time reading through drafts of what I wrote, I am very grateful. Thank you to my parents and my closest family and friends for the ongoing encouragement during this year and in general.

J.-A.S.

Contents

List of Figures

List of Tables

Chapter 1

Strongly interacting matter

This chapter serves as an introduction to some fundamental concepts of hadronic interactions linked to the work presented in this thesis. In the first part the basic notions of strong interaction will be introduced, with a particular focus on the strong coupling constant, α_s. Afterwards the concept of the Quark-Gluon Plasma (QGP) will be introduced and discussed, along with an explanation of the current understanding of the phase diagram of QCD matter. Furthermore, the experimental access to this particular state of matter through heavy-ion collisions will be introduced, with a brief explanation of the main experimental signatures. Finally the motivations along with the outline of this thesis will be discussed.

1.1 Quantum Chromodynamics

In analogy to Quantum Electrodynamics (QED), the theory which describes electromagnetically interacting systems, the Quantum Chromodynamics (QCD) is a gauge field theory developed to describe the strong interaction. In QED, the interaction between electrically charged particles is mediated through virtual photons. In QCD, the color charged elementary constituents, quarks, have six flavors and are classified in three "generations". The quarks carry strong color charge in three different "color" types (red, green and blue in addition to the corresponding anti-colors for anti-quarks). Their interactions are mediated through "gluons", which come in eight color combinations and play the same role as the photon does for electromagnetism. One of the main differences between QCD and QED is that the intermediate gauge bosons in QCD carry a color charge themselves and can therefore interact with each other. As a consequence, the intensity of the strong force varies in a different way as a function of the distance between the interacting partons, leading to some important consequences briefly discussed later in this section.

The properties of QCD can be described mathematically by a gauge invariant QCD Lagrangian [46]:

$$\mathscr{L}_{\mathrm{QCD}} = \overline{\psi}_i [i(\gamma^\mu \mathrm{D}_\mu)_{ij} - m\delta_{ij}]\psi_j - \frac{1}{4}\mathrm{G}^a_{\mu\nu}\mathrm{G}_a^{\mu\nu}, \tag{1.1}$$

where $\psi_i(x)$ is the Dirac spinor of the quark field in the fundamental representation of the SU(3) gauge group. The quark mass is represented by m. The four-vector D_μ is the covariant derivative, and the gluon field strength tensor is represented by $\mathrm{G}_{\mu\nu}$. Dirac matrices, γ^μ, connect the spinor representation to the vector representation of the Lorentz group.

The intensity of each interaction is described by the specific coupling constant. In QED at low energies, the coupling is of the order of the fine structure constant $\alpha \sim 1/137$ and it increases with Q^2, the momentum transferred in the interaction. Nevertheless the weakness of the electromagnetic coupling ($\alpha << 1$) facilitates the application of perturbation theory. The cross-sections are computed as an expansion in powers of α. Since α is small, the higher orders (next-to-leading order(s)) can be neglected.

Similarly the dimensionless strong coupling constant a_s defines the strength of the strong interaction. It also depends on the square of momentum that is transferred during the interaction and it is described through the renormalization group equation:

$$\alpha_{\mathrm{s}}(Q^2) = \frac{\alpha_{\mathrm{s}}(\Lambda^2_{\mathrm{QCD}})}{1 + \frac{33-2N_f}{12\pi}\alpha_{\mathrm{s}}(\Lambda^2_{\mathrm{QCD}})\ln\frac{Q^2}{\Lambda^2_{\mathrm{QCD}}}} \approx \frac{4\pi}{(11-\frac{2}{3}N_f)\ln\frac{Q^2}{\Lambda^2_{\mathrm{QCD}}}}. \tag{1.2}$$

The number of flavors in Eq. 1.2 is represented by N_f ($N_f < 16$) and Λ_{QCD} is the QCD scale ($\Lambda_{\mathrm{QCD}} = 217^{+25}_{-23}$ MeV).

Even if the theory does not predict the actual value of the coupling constant, it can be fixed through experimental measurements at a certain energy scale, and then evaluated at any other energy scale Q^2 through the renormalization equation. The experimental confirmation of the "running" of the strong coupling constant through a wide series of measurements over different energies, is reported in Fig. 1.1 and represents one of the most impressive successes of QCD theory.

Due to the momentum dependence of α_{s}, the QCD cross-sections can be computed within the perturbative QCD (pQCD) only at high Q^2 (hard processes), where $\alpha_{\mathrm{s}} << 1$. At small Q^2 (soft processes), non-perturbative theories, such as lattice QCD, have to be used. Furthermore, the decrease of a_s at very short distances could lead to a quasi-free behavior of the quarks, called "asymptotic freedom". At longer distances, and thus for lower energies, the strong coupling constant has large values ($\alpha_{\mathrm{s}} >> 1$). This is responsible of the "confinement" of quarks in neutral color states (baryons and mesons), which is an important concept for introducing the QGP in section 1.2.

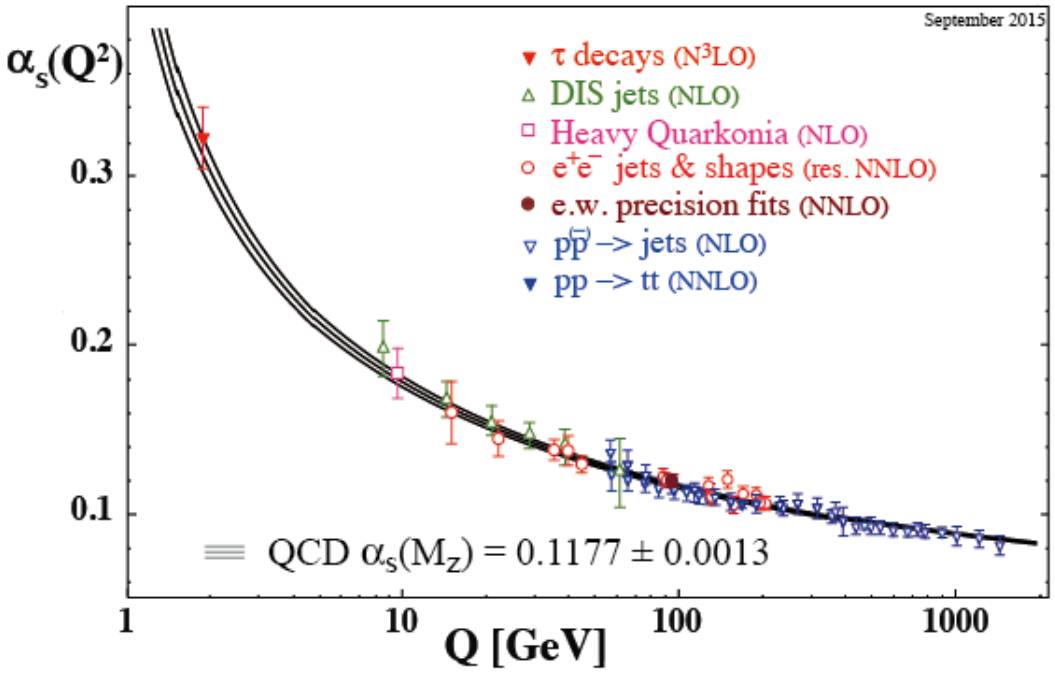

Figure 1.1: Summary of measurements of α_s as a function of the energy scale Q. The respective degree of QCD perturbation theory used in the extraction of α_s is indicated in brackets (NLO: next-to-leading order; NNLO: next-to-next-to leading order; res. NNLO: NNLO matched with resummed next-to-leading logs; N 3 LO: next-to-NNLO). [39]

To understand the concept of confinement, one can look at a static quark potential, which can describe the binding potential within a bound system of a heavy quark-antiquark pair:

$$V_{q\bar{q}}(r) = -\frac{4\alpha_s}{3r} + kr\,. \tag{1.3}$$

Here the intensity of the binding is expressed as a function of the separation r between the two quarks. For high values of r, the linear part is dominant. One can imagine that the quarks are bound by a color string with string tension k. When the separation grows, the energy in the gluon field that connects the quarks will increase as well. The energy will grow linearly until it is more energetically favorable to create a new quark-antiquark pair out of the field. Consequently the string will split when above a certain energy threshold, and the $q\bar{q}$ pair created will be merged with the original quarks, creating two mesons. An illustration of such a process is shown in Fig. 1.2 and because of this, “free” quarks are not observed in nature.

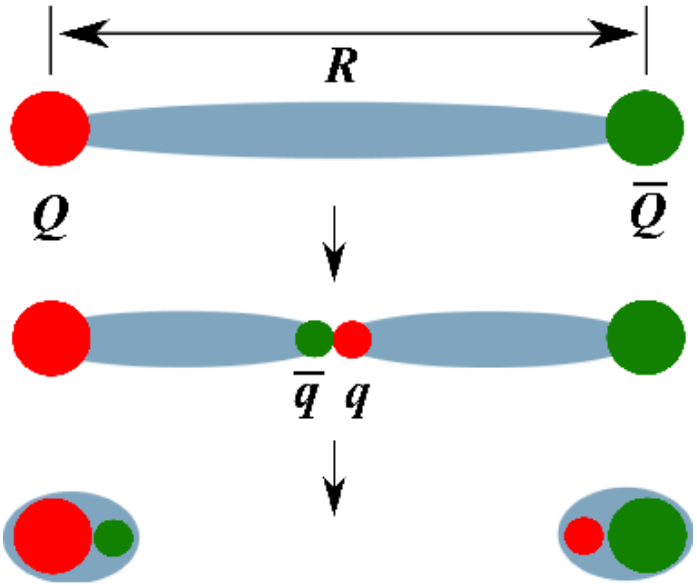

Figure 1.2: An illustration of the confinement.

1.2 The Quark-Gluon Plasma

1.2.1 Phases of QCD matter

On the basis of thermodynamical considerations and of QCD calculations, strongly interacting matter is expected to exist in different states.

Its behaviour can be characterized in the (T,μ_B) phase-space where T is temperature and μ_B[1] represents the baryon chemical potential, related to the net baryon density. It is known as QCD phase-space diagram and it is shown in Fig. 1.3. At low temperatures and for $\mu_B \sim 940$ MeV, we have ordinary matter. Increasing the energy density of the system, by compression (towards the right) or by heating (upward), a hadronic gas phase is reached in which nucleons interact and form pions, excited states of the proton and of the neutron (Δ resonances) and other hadrons. If the energy density is further increased, the transition to the deconfined Quark-Gluon Plasma (QGP) phase is predicted: the density of partons (quarks and gluons) becomes so high that the confinement of quarks in hadrons vanishes. The phase transition can be reached along different "paths" in the phase diagram. The state of the primordial Universe is believed to be composed of deconfined gluons and quarks and the transition QGP-hadrons, i.e. from the deconfined to the confined phase, took place at $\mu_B \sim 0$. On the other hand, in the formation of neutron stars, the gravitational collapse causes an increase in the baryonic density at temperatures very close to zero.

[1]The baryonic chemical potential of a system is defined as the change in the energy E of the system when the total baryonic number N_B (baryons - anti-baryons) is increased by one unit: $\mu_B = \partial E/\partial N_B$.

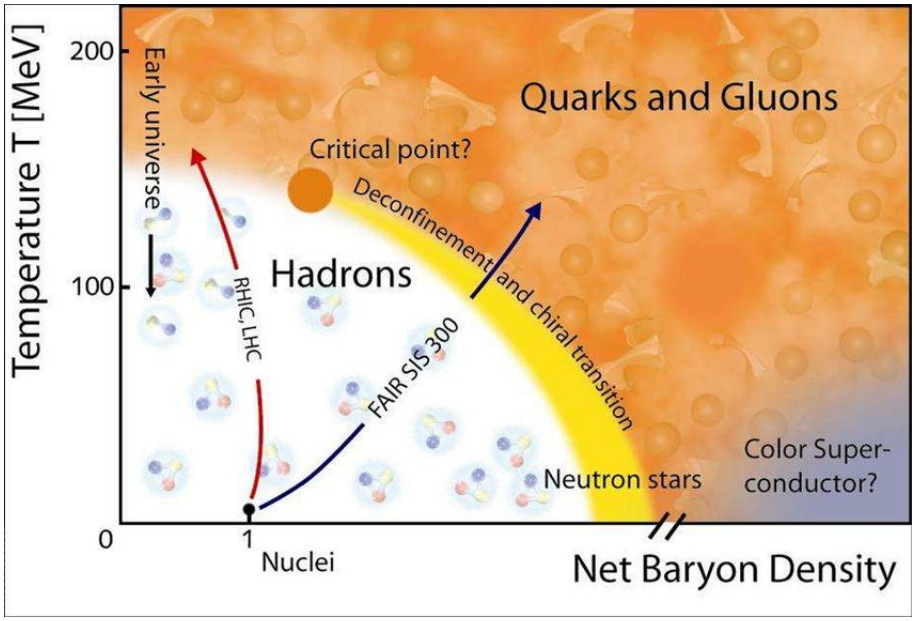

Figure 1.3: Phase diagram of strongly interacting matter in thermal equilibrium.

Besides thermodynamical considerations discussed above, making quantitative predictions about nuclear matter phase transition is indeed a challenging task. Simple models, such as the MIT Bag model [32], provide qualitative arguments to identify both critical temperature (T_c) and critical energy density (ϵ_c), which define the thresholds for the phase transition. Nevertheless, as QCD is generally considered the correct theory for interactions of quarks and gluons, it is necessary to study the phase of nuclear matter using full QCD. Equilibrium and phase transitions involve quarks and gluons interacting over a large distance scale, indicating the importance of non-perturbative physics. It is for this purpose that QCD calculations on a space-time lattice have been developed. The QGP phase is indeed predicted by Lattice Quantum Chromodynamics (LQCD) calculations. Predictions from recent LQCD calculations, obtained assuming vanishing baryo-chemical potential and employing (2+1) flavored QCD with realistic values for the mass of the strange and lighter quarks, show that thermodynamical quantities such as the pressure, the energy, and entropy density, which describe the equation of state of the quantum system, exhibit a rapid and simultaneous increase above a critical temperature of $T_c \sim 154$ MeV. How the transition from QGP into hadrons and reverse happens, is still discussed. The nature of the transition probed by LQCD simulations is dependent on the mass of the quarks, as well as on the baryo-chemical potential of the system. One possibility could be a n^{th}-order phase transition from a discontinuity of derivatives of free energy F up to the n^{th}-order. However, for physical values of the quark masses and vanishing μ_B simulations agree that the transition occurs as continuous cross-over (no discontinuous derivative of F).

1.2.2 Heavy-ion collisions

The only experimentally known way of creating QGP in the laboratory is by performing collisions of heavy nuclei at very high energies. Heavy-ion collisions have been investigated at the alternating gradient synchrotron (AGS) at BNL and at higher energies ($\sqrt{s_{\mathrm{NN}}}$ of about 17 GeV) at the the Super Proton Synchotron (SPS) at CERN. Investigations at SPS experiments hinted at the formation of the QGP. Relativistic Heavy Ion Collider (RHIC) detector at Brookhaven National Laboratory (BNL) increased the energy to $\sqrt{s_{\mathrm{NN}}}$ = 200 GeV, and since its completion in 2001 several interesting properties of this state of matter have been found. With the new era of the LHC, the ALICE collaboration can investigate this matter at an order of magnitude larger energy compared to RHIC.

Fig. 1.4 is a schematic representation of heavy-ion collisions and the space-time evolution in the Bjorken scenario [7]. The vertical y-axis represents the time and at y = 0 the collision between the two nuclei happens at τ = 0. The left side shows the collision without the formation of a QGP which has a color neutral pre-hadronic phase. The right side of the illustration includes the formation of a QGP where the degree of freedom are provided by quarks and gluons. There are four stages that can describe the evolution of the collision for the formation of QGP. These four stages are described in sequential order below:

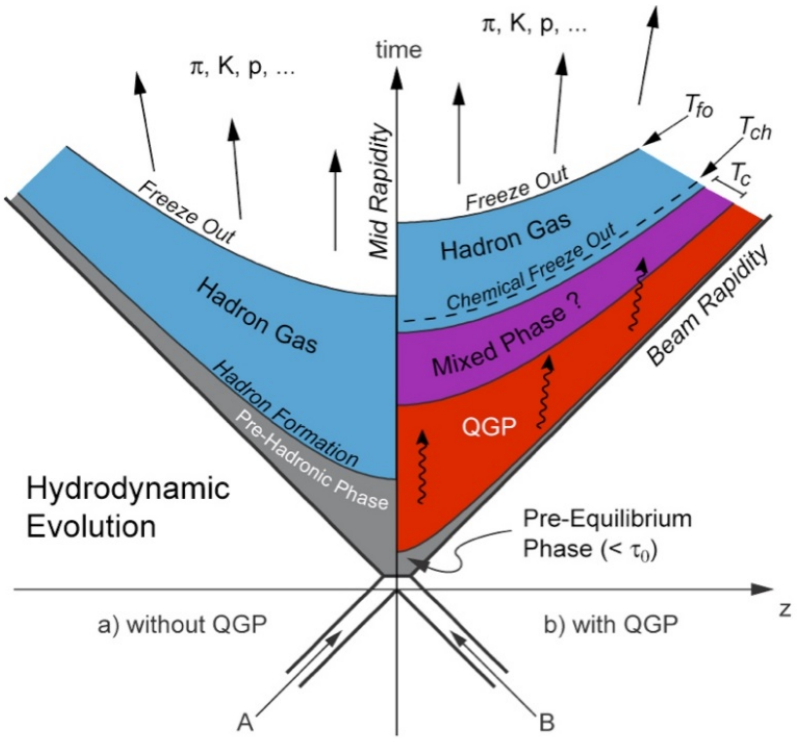

Figure 1.4: Space-time evolution of collisions of heavy ions. [7]

Stage 1: The system undergoes the so called "pre-equilibrium" phase. In this phase multiple hard scatterings between the partons of the two incoming nuclei take place and hard probes, such as high momentum particles and heavy-quarks, are produced.

Stage 2: System thermalizes as a results of rescatterings among partons, evolving towards a local "thermal equilibrium" state ($t \sim \tau_0$). In case the energy density and temperature of the system exceed the critical values ϵ_c and T_c, the nuclear matter can undergo color-deconfinement and the QGP is formed. The hot medium created, also known as the "fireball", expands and decreases in temperature.

Stage 3: The pressure of the system relatively to the surrounding vacuum induces its collective expansion. As a consequence of the expansion the energy density and temperature of the system goes down, up to the point where the nuclear matter can no longer be deconfined ($T < T_c$). At this point hadrons are formed from quarks and gluons, either instantly or through a mixed phase. When there are no more inelastic scatterings and the number of particle species is fixed, the "chemical freeze-out" occurs.

Stage 4: The matter, now only hadronic, expands and the hadrons can still interact elastically, exchanging energy and momentum. Hadronic elastic scatterings stop when particles are too far away from each other for any kind of interaction and momentum exchange. Now the system reaches the "kinetic freeze-out". The hadrons decouple and their momenta are fixed.

1.2.3 Experimental signatures of QGP formation

It is not possible to observe directly the QGP state in an experiment since it is a very short-lived state, so only indirect observables are studied to understand its properties. The experimental study of the QPG relies on a broad set of different observables that can be approximately divided in two main categories: hard and soft probes.

The **hard probes** are created in high momentum transfer processes. These probes are only created in hard scatterings during the first stages of the collisions and consist of high p_T particles, heavy-flavor particles, quarkonia, and jets. The study of hard probes allows for probing the microscopic properties of the QGP. Transport models that simulate heavy quarks traversing the QGP and interacting elastically and inelastically with the medium constituents, for example, allow the prediction (when compared to experimental measurements) of quantities like mean free path and transport coefficient of the QGP.

The **soft probes** come from processes with low momentum transfer and can be created at all stages of the collisions. They consist of light-flavor and low momentum particles. Soft probes allow to access global properties of the QGP by testing theoretical hydrodynamic description of

the medium and its evolution, from which quantities like temperature, viscosity, density, and expansion velocity can be predicted.

1.3 Outline of the thesis

In this thesis the production of prompt J/ψ and the beauty hadrons ($h_{\rm B}$) will be studied in proton-proton collisions at $\sqrt{s}$ = 5 TeV through the study of the inclusive decay channel $h_{\rm B} \rightarrow$ J/ψ + X, where the J/ψ is reconstructed in the e^+e^- decay channel. These measurements are of great importance for the ALICE (and the LHC) physics program for two reasons.

Prompt J/ψ and beauty hadrons belong to the categories of quarkonia and open-heavy flavor hadrons, respectively. As discussed in the previous section, these "hard probes" are crucial to characterize the properties of the QGP created in heavy-ion collisions. However, in order to correctly interpret results in large systems and quantify hot medium effects, a proper reference should be provided. The production measurements in pp collisions represent the baseline for heavy-ion studies, since no QPG formation is expected in small systems. In particular the measurements provided in this thesis can serve as a reference for future prompt and non-prompt J/ψ measurements in Pb-Pb collisions at $\sqrt{s_{NN}}$ = 5.02 TeV.

Furthermore, measurements in pp collisions represent a benchmark test for QCD based models in different energy domains, since for the production of open-heavy flavor and quarkonia both perturbative and non-perturbative aspects of the theory of the strong interaction are involved. The measurements provided by this thesis will be compared with the corresponding QCD models, thus providing additional constraints useful for their further tuning.

In chapter 2 the production mechanisms of open-heavy flavor hadrons and quarkonia in proton-proton collisions, along with some examples of experimental measurements showing the state of art, will be discussed. In chapter 3 the ALICE detector will be described, focusing on the performance in terms of impact parameter resolution of single tracks and particle identification. The analysis technique employed to determine the fraction of J/ψ originated from long-lived beauty-hadron decays is discussed in chapter 4. Prompt and non-prompt J/ψ are separated on a statistical basis, through an un-binned two dimensional log-likelihood fit procedure, exploiting the distance between the primary event vertex and the production vertex of the J/ψ candidate. In chapter 5 a certain number of systematic uncertainties, which account for possible improper description of fitting components, will be evaluated and discussed. In chapter 6 the measured non-prompt J/ψ fraction will be compared with similar measurements performed at several center-of-mass energies by other experiments. Furthermore the non-prompt J/ψ fractions will be combined with the corresponding published inclusive J/ψ cross-section results in

order to compute prompt and non-prompt J/ψ cross-sections. These will be compared to QCD-inspired models, pointing to the importance of higher-order corrections. An outlook for future possibilities based on the work presented in this thesis will also be discussed.

Chapter 2

Open heavy-flavor and quarkonium production in proton-proton collisions

Open and hidden heavy-flavor hadrons contain either charm or bottom quarks. These hadrons represent an important tool to test the theory of QCD in practice over different systems and energy regimes. Heavy-quark production requires large momentum transfer ($Q^2 > 4M^2_{\mathrm{c,b}}$). Therefore, the elementary partonic process can be computed in the framework of perturbative QCD down to low p_{T}. In opposition, the hadronization mechanisms, which are responsible for the formation of quarkonium states and open-heavy-flavor hadrons, or the momentum distributions of partons inside a nucleon, are described through semi-phenomenological models, due to the impossibility of applying perturbative QCD. The simultaneous comparison of both open and hidden heavy flavor measurements with theoretical predictions is therefore crucial to constrain QCD based models in both perturbative and non-perturbative regimes, improving our understanding of particle production in elementary collisions.

This chapter will first discuss the process of heavy-quark pair production in pp collisions, in particular how to compute the production cross-sections through the use of QCD. Afterwards the production of open-heavy flavor hadrons will be described and examples of comparisons between QCD models and experimental results will be shown. Finally charmonium production mechanisms will be discussed providing examples of comparisons with experimental measurements.

2.1 Heavy-quark production in pp collisions

A heavy-quark pair $q\overline{q}$ is formed through the strong interaction process. The simplest case of heavy-quark production in a collision between protons, illustrated in Fig. 2.1, is through the pro-

cess of hard partonic scattering, where the participants can be pairs of either gluons or quarks (partons).

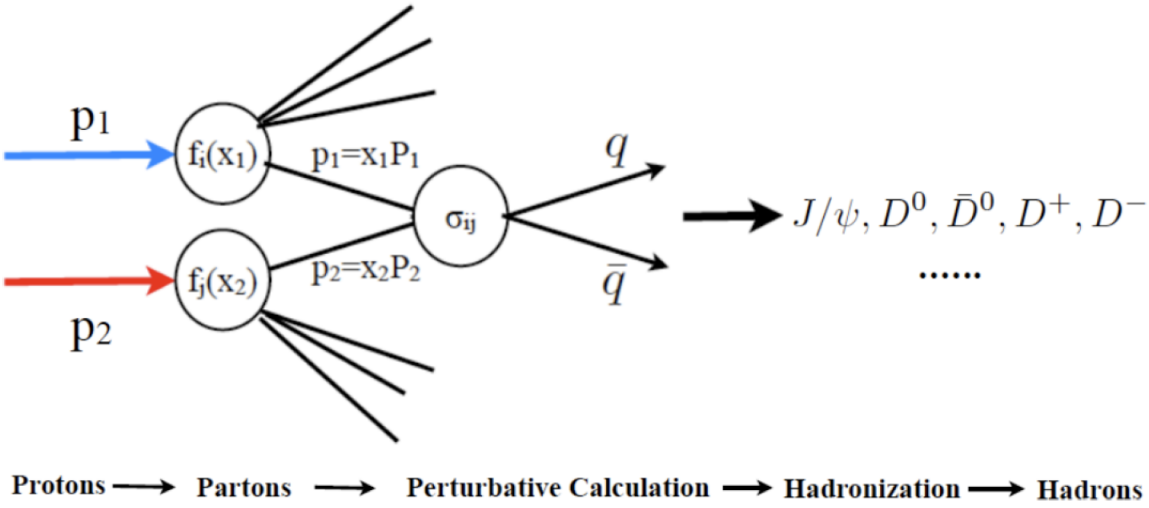

Figure 2.1: An illustration of a hard scattering process. Two particles collide and a heavy-quark pair is formed.

In order to compute the production cross-section of such processes, an important ingredient is represented by the momentum of the two incoming partons. The first principles of QCD do not predict the momentum distributions of the partons inside a free nucleon. Because of this, experimental measurement results are the basis for the study of these processes. The distributions of momentum of partons inside a nucleon are described through Parton Distribution Functions (PDFs). In particular the PDFs $f_i(x, Q^2)$ define the probability for each parton species i to carry a fraction x of the nucleon longitudinal momentum. The variable i can be either a gluon or a quark. Using a "collinear" approach, the PDFs can be looked at as independent from the scattering process. However, since the process occurs at a specific energy scale Q^2, the PDFs need to be determined accordingly. Deep Inelastic Scattering (DIS) experimental results provide a nice and clean extraction basis for the PDFs. The PDFs measured at a specific energy scale can be evolved to a different energy scale Q^2 with a perturbative approach, using the DGLAP[1] evolution equation, that works well with high Q^2. In this way the PDFs measured at lower energy DIS experiments can be used to calculate observables at higher energy hadron-hadron colliders. Uncertainties on the evaluation of PDFs are represented by the experimental uncertainties of the input measurements in addition to DGLAP assumptions. The evaluations of PDFs are often updated with either new experimental data, or new model developments. Popular choices at hadron colliders are parametrizations such as CTEQ [53], HERAPDF [17], MRS [52] and NNPDF [25]. An example derived from fits of H1 and ZEUS data at HERA is shown in Fig. 2.2.

[1]Short for Dokshitzer-Gribov-Lipatov-Altarelli-Parisi

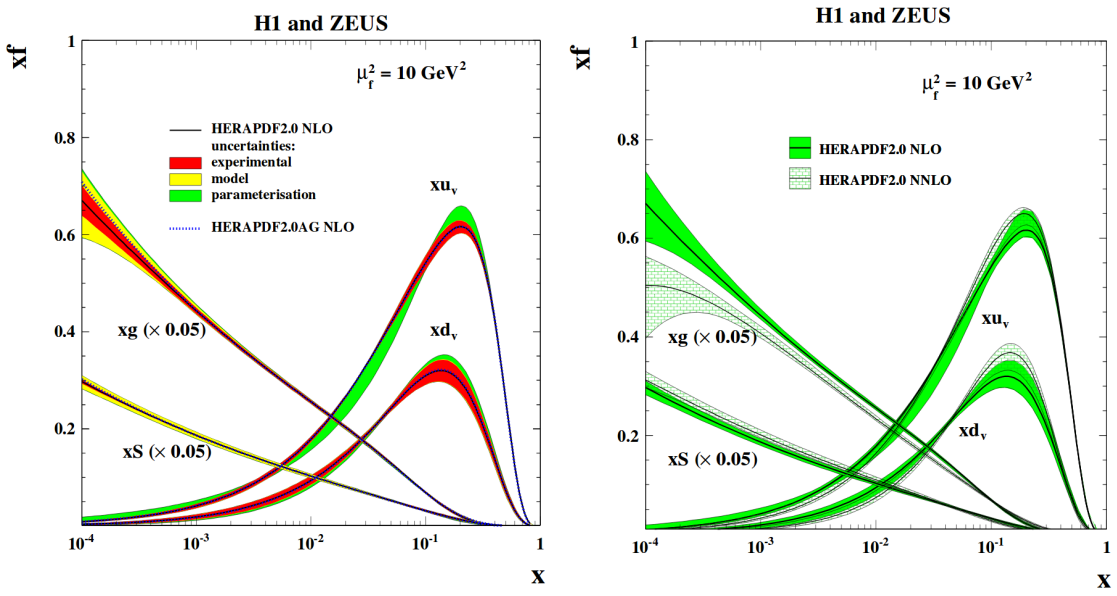

Figure 2.2: PDFs for the valence (xu_v, xd_v) sea quarks ($xS = 2x(\overline{U}+\overline{D})$), and for the gluons (xg) as computed by the HERAPDF group from fits of H1 and ZEUS data at $Q^2 = \mu_F^2 = 10\ \mathrm{GeV}^2$. The gluon and sea quark densities can be thought as being generated by radiative processes from the valence quarks and constitute the dominant contribution at low x values, carrying about half of the momentum of the proton. Their distribution has been scaled by a factor 1/20 for visibility. Left panel shows the computations at NLO of DGLAP framework along with the related experimental, model, and parametrization uncertainties. Right panel shows the comparison between the computations performed at NLO and NNLO. Figure from [17].

Assuming that the kinematic conditions and momentum distributions of the partons are known, the production cross-section for a heavy $q\overline{q}$ pair production process can be computed in the framework of perturbative QCD. An infinite number of scattering matrix elements contribute to the cross-section, making it impossible to calculate the exact cross-section out of the first principles of QCD. Although the exact value of the cross-section is not reached, a finite number of terms are sufficient to find a very good approximation. The numerical power-expansion of the cross-section evaluation can be represented as through a set of elementary different QCD processes. Each QCD process corresponds to a Feynmann diagram, as shown in Fig. 2.3, where both LO and NLO contributions (pair production with gluon emissions, flavor excitation and gluon splitting) are shown. The number of vertices is proportional to the power of α_s.

The running coupling constant needs to be small. This is ensured by requiring $Q^2 \gg \Lambda_{QCD}$ (see section 1.1). Perturbative QCD (pQCD) can be applied, and the numerical power-expansion converges. The dominant processes are hence the first-order processes, (a) and (b) in Fig. 2.3. A higher order of α_s contributes less to the overall amplitude. Because of this, even higher order contributions can be neglected.

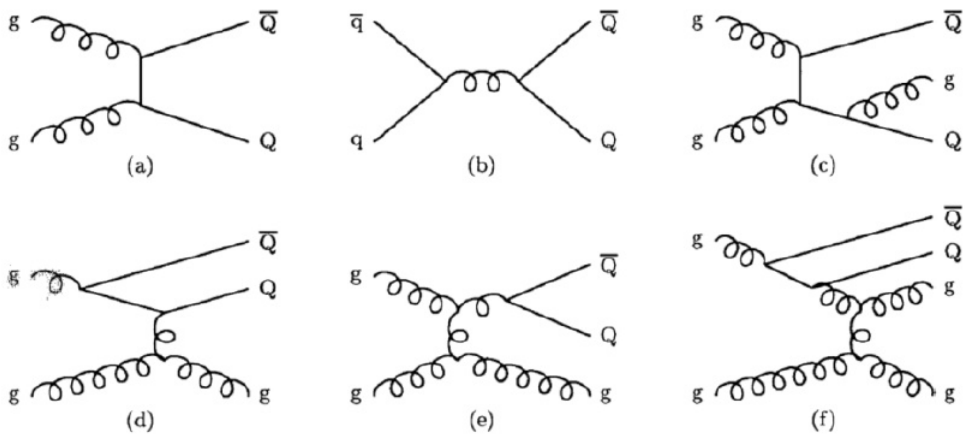

Figure 2.3: An overview of Feynmann diagrams relevant to the computation of a heavy-flavor quark pair production. Leading order (LO) contributions are shown in panels (a) and (b). Next-To-Leading Order (NLO) contributions are seen in panels (c), (d) and (e). These contributions represent pair production with gluon emissions, flavor excitation and gluon splitting processes. The last panel (f) represents higher order flavor excitation events.

Assuming that the probabilities of extracting a parton from the incoming nucleons are independent from the scattering process, the cross-section $\sigma^{q\overline{q}}(\mathrm{P_1},\mathrm{P_2})$ for the production of a $q\overline{q}$ pair from the collision of two nucleons 1 and 2, with four-momenta P_1 and P_2, can be computed within the collinear-factorization framework:

$$\sigma^{q\overline{q}}(\mathrm{P_1},\mathrm{P_2}) = \sum_{\mathrm{i,j}} \int \mathrm{dx_1 dx_2 f_i^1}(\mathrm{x_1},\mu_\mathrm{F}^2)\mathrm{f_j^2}(\mathrm{x_2},\mu_\mathrm{F}^2)\cdot\hat{\sigma}_{\mathrm{i,j}}^{\mathrm{q\overline{q}}}(\mathrm{p_1},\mathrm{p_2},\mathrm{Q}^2,\alpha_\mathrm{s}(\mu_\mathrm{R}^2);\mu_\mathrm{F},\mu_\mathrm{B})\,. \tag{2.1}$$

In Eq. 2.1 $p_1 = x_1 \cdot \mathrm{P_1}$ and $p_2 = x_2 \cdot \mathrm{P_2}$ are the momenta of the scattering partons, expressed in terms of their corresponding x fractions x_1 and x_2. $f_i^1(x_1,\mu_\mathrm{F}^2)$ represents the PDFs for the parton species i in the nucleons. Lastly, $\hat{\sigma}_{i,j}^{q\overline{q}}$ describes the short-distance cross-section for the scattering partons i and j.

The collinear approach, also known as "factorization theorem", justifies that the short-distance dynamics of the hard scattering process can be factorized out of the long-distance PDFs. This is the simplest conceptual scheme for the development of heavy-flavor hadron production models. The only ingredient to be calculated at a fixed order in pQCD, is the partonic short-distance cross-section $\hat{\sigma}_{i,j}^{q\overline{q}}$. The factorization scale μ_F and the renormalization scale μ_R are two QCD scale parameters that the cross-section depends on.

μ_R represents the "renormalization scale" introduced in order to avoid divergences in the computation of elementary cross-sections. There are divergences in QCD power-expansions from either soft and collinear real gluon emissions or from virtual loops in the corresponding Feyn-

mann diagrams. However, since QCD is a renormalizable quantum field theory, the divergences can be canceled through a mathematical re-formulation of the theory, called "renormalization", which implies the redefinition of the strong coupling constant at $\alpha_s(\mu_R)$. In this way the divergent contribution from virtual loops is canceled.

The factorization scale μ_F is introduced in the perturbative DGLAP evolution of the scale-dependent PDFs at the value of $f_i(x_1, \mu_F^2)$. The factorization scale μ_F can be taken as the scale that separates both the long- and short-distance dynamics that are calculable in pQCD. When possible, the value of μ_F is set equal to $\alpha_s(\mu_R)$.

Even though the computed physical cross-sections in theory should not depend on the choice of the QCD scale parameters, some dependence is observed. This dependence is a significant source of uncertainties in the theoretical predictions, especially when higher-order perturbative calculations are dropped out. Quark masses are another source of uncertainties. Fig. 2.4 shows the $c\bar{c}$ and $b\bar{b}$ production cross-sections in pp collisions computed with a collinear-factorization approach. A PYTHIA program with the CTEQ5L set for the nucleon PDFs is used for this. In addition, energy dependence of the different NLO contributions on the total cross-section is shown as well.

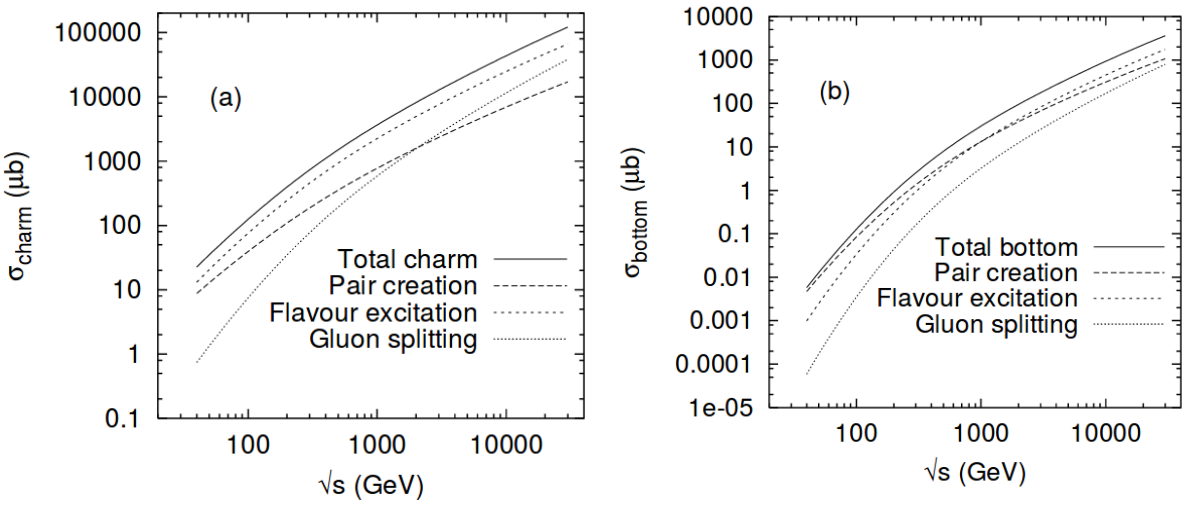

Figure 2.4: Energy dependence of the total cross-sections for charm (a) and beauty (b) quarks in pp collisions. These are results from PYTHIA computations presented in [54]. The contributions from pair creation, flavor excitation and gluon splitting are shown separately.

The framework of collinear-factorization describes high-Q^2 processes excellently in experiments for DIS, weak-gauge bosons, jets, and Higgs production processes at hadron colliders. However, in the very low x region it is expected that the gluon densities become so high that their wave functions completely overlap each other, reaching a saturation in terms of momentum phase-space. In this regime the PDFs evolution described in the collinear framework is expected not

to work anymore. Alternatives to the collinear framework are developed, in particular the Color Glass Condensate (CGC) [44] provides an appropriate description of PDFs in such conditions.

2.2 Open-heavy flavor production

The initial hard parton scattering produces heavy-quarks that evolve from free colored objects to color-singlet hadrons, because of color confinement. This transition is called "fragmentation" and it is outside the realm of pQCD as it is a long-distance mechanism occurring via soft-momentum transfers, leading to the strong coupling constant α_s rising. The fragmentation occurs on a larger time scale compared to the hard scattering process. Because of this, one can treat fragmentation as an independent process using phenomenological models.

The fragmentation function $D_q^h(z,\mu_F)$ describes the probability for a quark q to produce a hadron h, with a momentum fraction $z = p_h/p_q$:

$$D_q^h(z,\mu_F) = \int_z^1 D_q(x,\mu_F)\cdot D_q^h(z\mid x)\,dx. \tag{2.2}$$

In Eq. 2.2 there is the convolution of two terms. The perturbative term $D_q(x,\mu_F)$ describes the short-range fragmentation of the heavy quark q. It accounts for the parton shower processes that include successive splittings and gluon emissions. The variable x represents the fraction of the momentum of the quark which survives after parton shower processes. These are treated perturbatively by means of the DGLAP evolution equations, down to the limit $\mu_F \sim \Lambda_{QCD}$. Below such a limit the perturbative approach becomes unreliable.

The phenomenological function $D_q^h(z\mid x)$ represents the probability for a hadron h to be produced with a fraction z of the momentum of the quark, providing that a fraction x had survived after the parton shower processes.

Assuming the fragmentation scheme, the fragmentation functions are independent of the initial process of hard scattering. Because of this, the fragmentation functions are universal and adapted from e^+e^- or ep collision results to describe the measurements performed at hadron colliders.

Example of QCD models and comparison with experimental results.
By convoluting the differential $q\overline{q}$ pQCD cross-sections with the fragmentation functions, one can produce predictions for inclusive single hadron production. However, for transverse momenta that is much larger than the quark mass, some logarithmic terms proportional to the ratio $\frac{p_T}{m_q}$ appear in the power expansion, becoming eventually too large at all orders in the per-

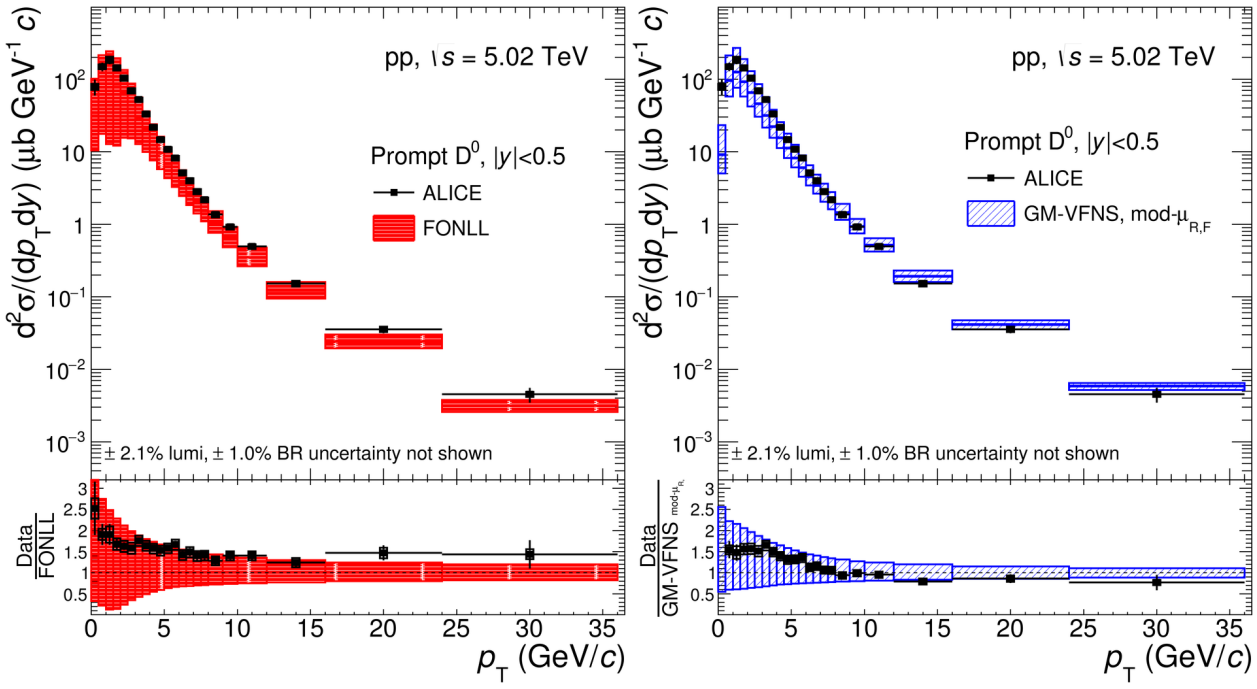

Figure 2.5: Production cross-section of D^0 mesons in pp collisions at $\sqrt{s}$ = 5 TeV measured at mid-rapidity by the ALICE experiement. The results is compared to FONLL (left) and GM-VGNS pQCD (right) calculations. [21]

tubation theory.

Through the Fixed-Order Next-To-Leading-Logarithm (FONLL) framework, the quark-mass logarithms are handled in the perturbative expansion. The prescription of FONLL consists in a separate resummation (RS) of Next-Leading-Order (NLO) calculations for low p_{T} and Next-To-Leading-Log (NLL) calculations for the high p_{T} region. In this way the convergence of the series expansion is recovered. FONLL allows the evaluation of a single inclusive distributions of either heavy-quarks or hadrons by including the convolution with a non-perturbative fragmentation function.

Another pQCD based calculation scheme is the General-Mass Variable-Flavor-Number Scheme (GM-VFNS) [47, 48]. Like FONLL, the approach of GM-VFNS performs a resummation up to NLL. One advantage with this approach is that it provides predictions for the production cross-section of baryons, something FONLL does not.

Both of these two calculations have a good agreement with experimental measurements. An example is shown in Fig. 2.5 where p_{T}-differential production cross-sections of prompt D_0 mesons at mid-rapidity in pp collision at $\sqrt{s}$ = 5 TeV, measured by ALICE, are compared with theoretical predictions from FONLL (left) and GM-VFNS (right). The theoretical models are compatible with data within uncertainties in the whole p_{T} range, although the data points are located at the

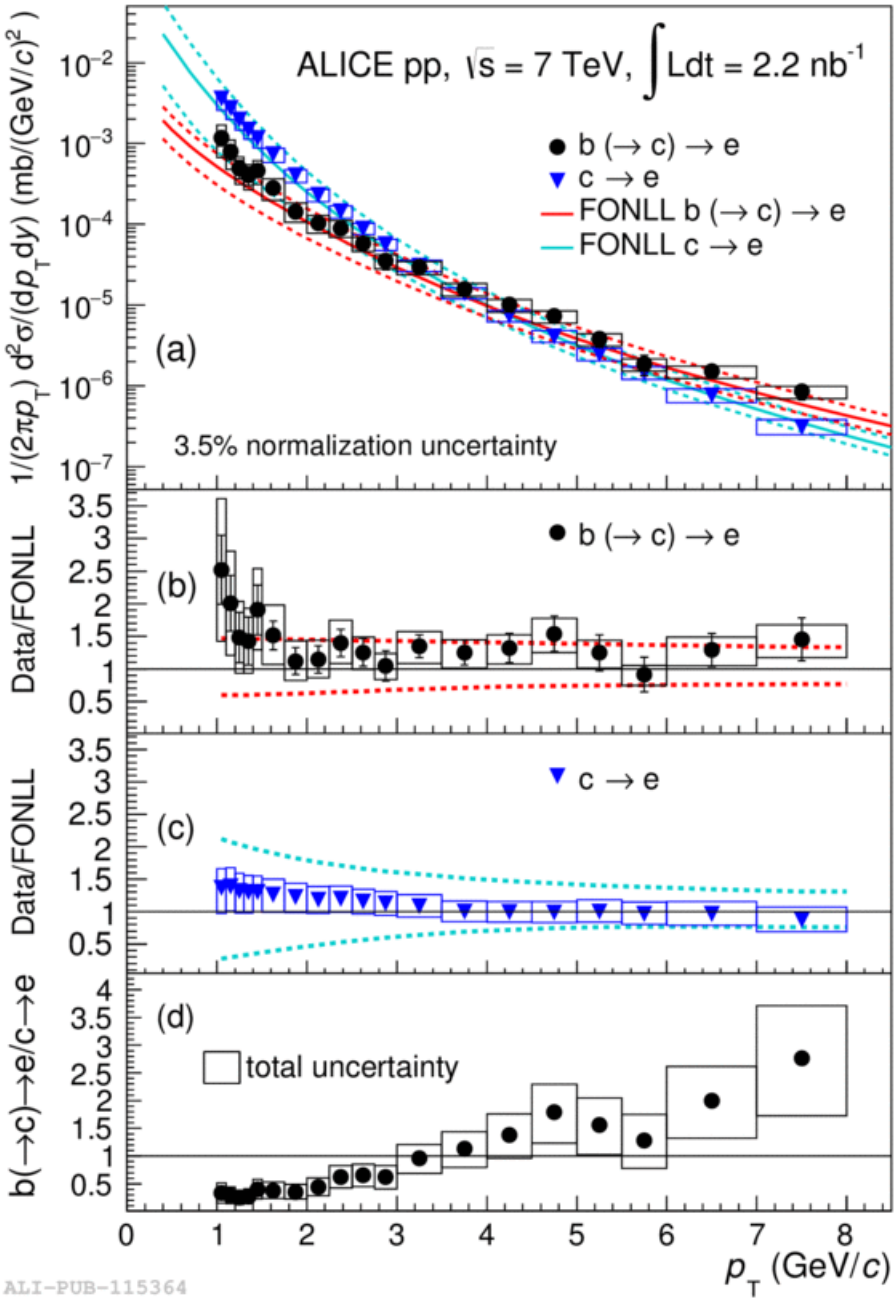

Figure 2.6: (a) pt-differential invariant cross-sections of electrons from beauty and from charm hadron decays. The error bars (boxes) represent the statistical (systematic) uncertainties. The solid (dashed) lines indicate the corresponding FONLL predictions (uncertainties). Ratios of the data and the FONLL calculations are shown in (b) and (c) for electrons from beauty and charm hadron decays, respectively, where the dashed lines indicate the FONLL uncertainties. (d) Measured ratio of electrons from beauty and charm hadron decays with error boxes depicting the total uncertainty. [13]

upper band of both FONLL and GM-VFNS uncertainties.

Regarding the testing of beauty hadron production at low p_{T} and mid-rapidity, the only measurements available at the LHC are performed by the ALICE collaboration. Besides non-prompt J/ψ measurements, beauty hadron cross-sections can be tested in ALICE at mid-rapidity measuring electrons from heavy-flavor decays. The cross-sections of electrons from beauty hadron decays (b → c → e) and also the one of electron from charm hadron decays (b → c → e) in pp collisions at $\sqrt{s}$ = 7 TeV are shown in Fig. 2.6. The separation of beauty and charm electrons relies on fitting procedures that use the impact parameter of single tracks. The measurements are compared to FONLL predictions, showing a good agreement within uncertainties over a wide p_{T} range, although there are large uncertainties at low p_{T}. In the bottom panel (d) the ratio between beauty and charm decay electrons shows that the contribution from beauty is significant and overcomes prompt charm for $p_{\mathrm{T}} > 4$ GeV/c.

2.3 Charmonium production mechanisms

In addition to the ability to combine with other light quarks to form open B or D mesons, the heavy-quark pair produced in a hard scattering can bind together to form a quarkonium state ($\mathrm{b\bar{b}}$ or $\mathrm{c\bar{c}}$). The fundamental mechanisms of quarkonium state production is regarded as an intermediate between the perturbative and non-perturbative QCD regimes. As described in section 2.1, the production of the heavy-quark pair involves large momentum transfers, implying perturbative QCD can be used. However, the evolution of the heavy-quark pair towards the bound quarkonium state happens over large time scales and long distances, with soft momentum interactions with the surrounding color field. The nature of this is non-perturbative. The production mechanism of quarkonia are also based on a factorization between the quark pair production and its subsequent binding. The difference of the models usually stems from how the hadronisation process is handled.

Since the argument of this thesis is related to the study of prompt and non-prompt J/ψ, a short description of the properties of the J/ψ meson is added before discussing the different production models for charmonia.

2.3.1 Properties of the J/ψ

The J/ψ meson is flavor-neutral and consists of a charm quark-antiquark pair $\mathrm{c\bar{c}}$. Mesons formed by a bound state of $\mathrm{c\bar{c}}$ are considered "charmonium", with J/ψ being the most common due to the low rest mass of 3.1 GeV [56]. The J/ψ is the s-wave orbital state, the ground state, of char-

monia. The properties of J/ψ contain a spin of 1, odd parity and zero charge.

The mass is small enough to be below the open charm threshold, meaning the mass required to form a pair of mesons of a charm and a light quark, i.e. D-mesons. As a consequence, $c\bar{c}$ annihilation is the only way the J/ψ decays. Because of the color-singlet state of the J/ψ, it cannot decay into hadrons through a single gluon line. Having odd parity, only an odd number of gluon lines is allowed in the strong decay of the J/ψ. Thus, the decay requires a minimum of three gluon lines, and the coupling becomes proportional to that of the electromagnetic decay channel, resulting in a high branching ratio for decay into lepton [56].

At the LHC energies a sizable fraction of J/ψ ($\sim$ 10%) at low p_{T} originates from the decay of beauty hadrons [14]. The importance of measuring this fraction for the correct understanding of prompt charmonium production models will be clarified in chapter 4.

2.3.2 Color Evaporation Model

The Color Evaporation Model (CEM) is a simple phenomenological model that predicts charmonium production cross-sections. It was proposed by Fritzsch in 1977 [42]. The model assumes that a heavy-quark pair with a mass smaller than the open-heavy-quark threshold has a statistical probability to evolve into a quarkonium state, regardless of the quantum state in which the pair was produced. The total charmonium cross-section is computed by integrating the differential heavy-quark pair production cross-section $\left(\frac{d\sigma_{c\bar{c}}}{dm}\right)$ between the threshold to produce a charm pair ($2m_{\mathrm{c}}$) and the one for producing the lightest open-charm hadron pair ($2m_D$):

$$\sigma_{\mathrm{onium}} = \frac{1}{9}\int_{2m_{\mathrm{c}}}^{2m_{\mathrm{D}}} dm \frac{d\sigma_{\mathrm{c\bar{c}}}}{dm}. \tag{2.3}$$

The color "evaporates" through soft gluon emissions and the state becomes colorless. The probability to evolve into a specific quarkonium state is assumed to be the same at different collision energy, collision system, and kinematic variables. CEM is a very simple model that predicts accurately as the only free parameters are the relative abundances of different quarkonia states. An example of comparison between J/ψ measurements performed by ALICE at forward rapidity [19] and the CEM model is shown in Fig. 2.7. The experimental data points are placed around the edge of the upper end of the large uncertainty band of the CEM predictions.

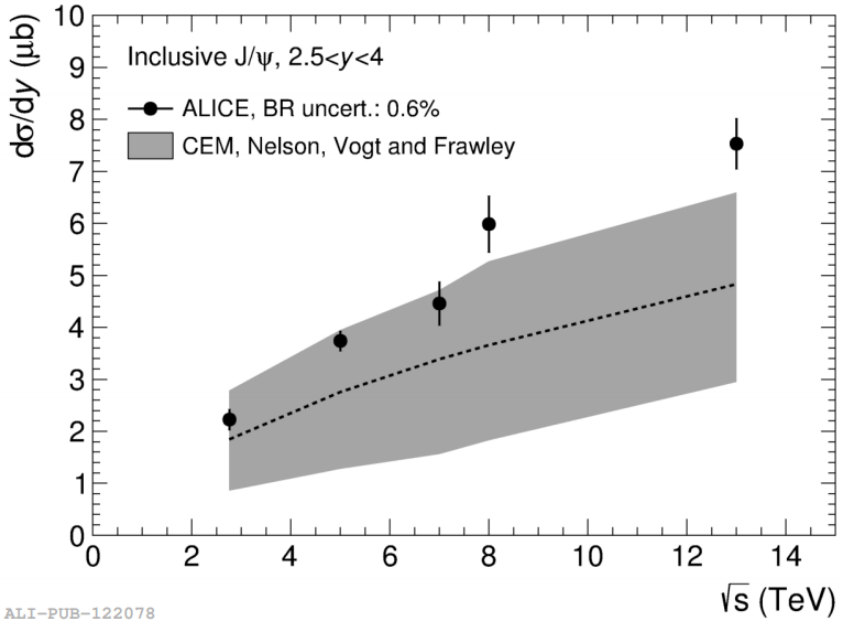

Figure 2.7: Total J/ψ cross-section at forward rapidity as a function of collision energy, compared to a prediction from the Color Evaporation Model. [19]

2.3.3 Color-Singlet Model

The Color-Singlet Model makes an assumption that the quantum state of the produced quark pair does not change during the binding stage, neither in spin nor in color. Because the physical state is color neutral, the pair produced is then required to be a color-singlet state. At collider energies, such as at the LHC, processes involving gluons are most relevant. The process at the lowest order is shown on the left in Fig. 2.8.

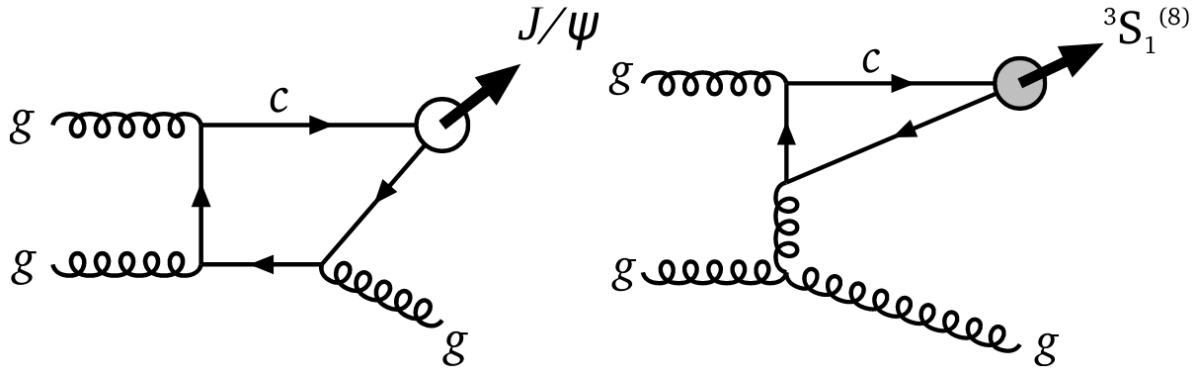

Figure 2.8: Two typical J/ψ production processes. Left: Lowest order color-singlet channel. Right: Color-octet production from gluon splitting channels. [49]

The evolution to a bound charmonium state can be obtained from potential model calculations. In order to proceed to a bound charmonium state, the heavy quarks have to be close to each other. This implies that the velocity of the constituents has to be small in the meson reference frame. The probability for a heavy-quark pair to form a quarkonium state is proportional to the radial wave function of the $c\bar{c}$ pair at the origin $R_S(0)$ for S-wave states, and to the first derivative of the wave function $R'_p(0)$ for a P-wave state. The wave functions can be extracted from the leptonic decay widths (Γ_{ee}) of the corresponding state. For example for the J/ψ meson:

$$\Gamma_{ee} \equiv \Gamma(J/\psi \rightarrow l^+ + l^-) \approx 4\frac{\alpha^2}{9m_c^2}|R_{J/\psi}(0)|^2. \tag{2.4}$$

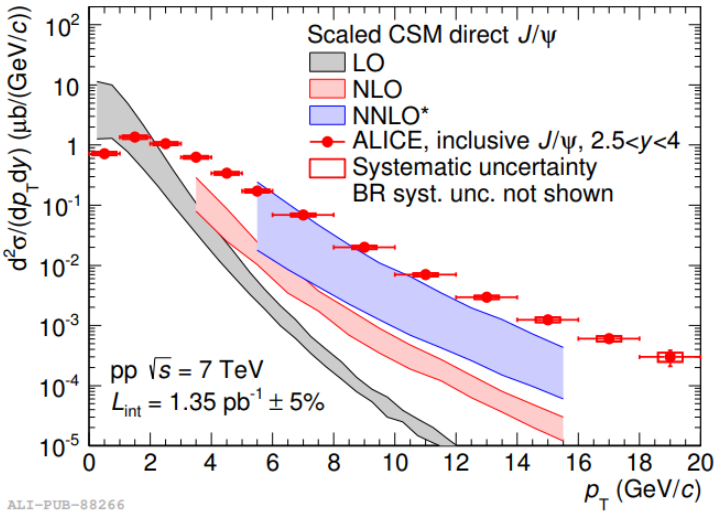

Figure 2.9: J/ψ production cross-section as a function of transverse momentum at forward rapidity in proton-proton collisions at $\sqrt{s}$ = 7 TeV, compared to predictions from the Color Singlet Model at leading order (LO), next-to-leading order (NLO), and NLO with leading p_T next-to-next-to-leading order contributions (NNLO*). Figure taken from [15]

.

While initially at lower collision energies a very good description of experimental data could be achieved with CSM [24], the cross-sections are severely underestimated at higher energies. However, the discrepancies can be fixed with color-octet process inclusion. An example of such data-model comparison is shown in Fig. 2.9. In this figure, the measured p_T differential J/ψ cross-section measured by ALICE at forward rapidity in pp collisions at $\sqrt{s}$ = 7 TeV is compared to CSM calculations. The greyed area is CSM calculation predictions at leading order (LO), the pink area complete next-to-leading-order (NLO), and leading p_T next-to-next-to-leading order contributions (NNLO*). The data is described better with the increasing order. However, tensions between data and model are still present even considering the higher order calculations.

2.3.4 Non-Relativistic Quantum Chromodynamics

The most careful approach yet to model charmonium production is the Non-Relativistic QCD (NRQCD) effective field theory. In this model there are three different energy scales that are highly relevant for hadronic quarkonium production. The first one is the heavy quark mass M. The second one is the typical momentum of the heavy quark Mv. Finally the typical energy of the heavy quark inside the quarkonium Mv^2. The probability to produce a charmonium state H can be split into the product of the short-distance perturbative cross-section to produce a heavy-quark pair in a specific quantum state, and the non-perturbative probability to evolve into the charmonium state under consideration. The sum over all possible quantum states in which the heavy-quark pair can have been produced, constitutes the total cross-section:

$$d\sigma(H) = \sum_{\kappa} d\sigma_{\kappa} < \iota_{\kappa}^{H} > . \tag{2.5}$$

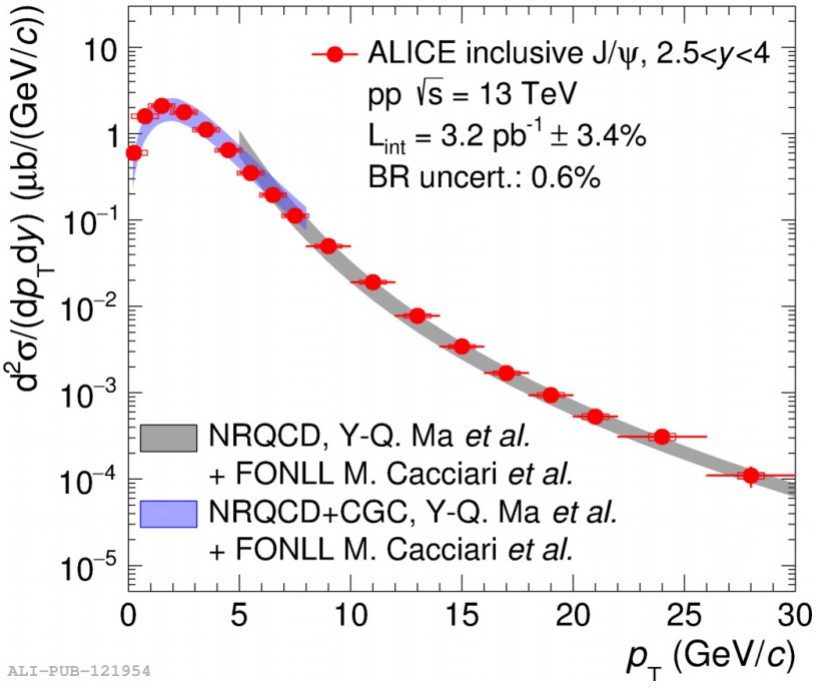

Figure 2.10: J/ψ production cross-section as a function of transverse momentum at forward rapidity in proton-proton collisions at $\sqrt{s}$ = 13TeV, compared to predictions from NRQCD. In NRQCD+CGC, effects from the CGC model are included at low p_{T}. The non-prompt contribution is taken from FONLL. [19]

In Eq. 2.5 one sums over the quantum number of the produced heavy-quark pair state $\kappa = {}^{2s+1}L_J^{[c]}$. The color state is either color-octet or color-singlet and is represented by c. The spin is

described by s. The short range production amplitudes for a heavy-quark pair in the given state, are denoted by $d\sigma_\kappa$. These are convoluted with the PDFs. Finally, $\iota_\kappa^{\mathrm{H}}$ are the corresponding non-perturbative long-distance matrix elements (LDMEs). The LDMEs decribe the transition from the heavy-quark pair to a quarkonium state.

The LDMEs are expanded in powers of the heavy quark velocity v, as opposed to the heavy-quark production cross-sections that come from a perturbative expansion in α_{s}. The LDMEs are assumed to be universal, which gives the model predictive power for cross-sections at different energies or collision systems. The LDMEs can be obtained from experimental data. For example, the LDMEs can be retrieved from decay rates of beauty mesons to charmonia.

In the NRQCD approach one also considers the pQCD processes that produce heavy-quark pairs in a color-octet state. This is not the case for the CSM model. One recovers the CSM if only the processes at the lowest order of v are considered. The right panel on Fig. 2.8 shows an example of a process not included in the CSM as it can only produce color-octet states.

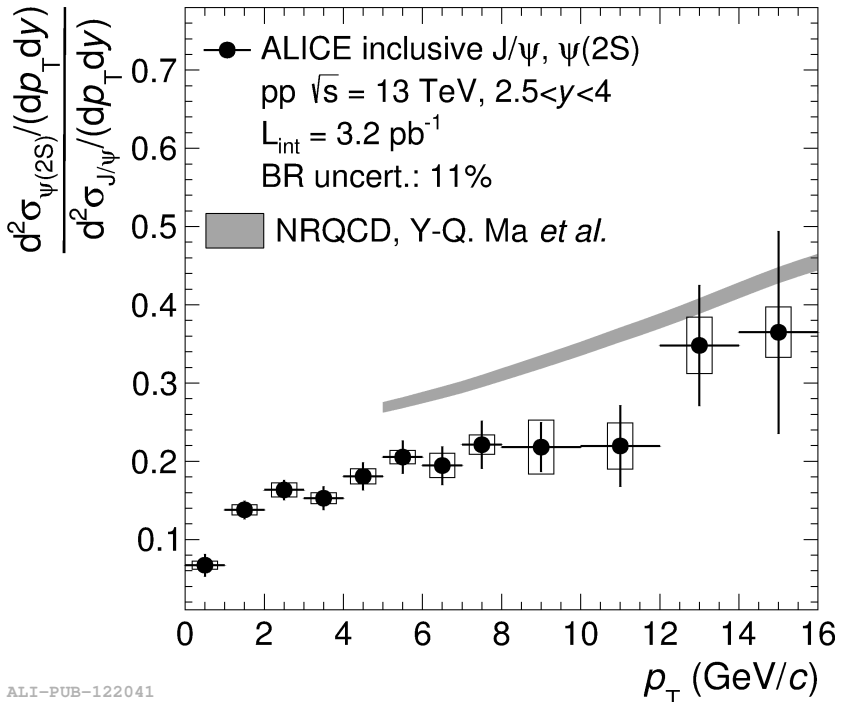

Figure 2.11: Comparisons between ALICE inclusive $\psi(2S)$-to-J/ψ cross-section ratio as a function of p_{T} in pp collisions at $\sqrt{s}$=13 TeV [19] and NRQCD model calculation [2]

NRQCD gives accurate predictions and fit well with data for high p_{T}. Through the inclusion of initial effects from the CGC framework into the short-range heavy-quark production amplitudes, one gets a description of the data that is equally good. The inclusive J/ψ cross-section at forward rapidity as a function of p_{T} in pp collisions at $\sqrt{s}$ = 13 TeV is shown in Fig. 2.10. Predictions from two models are also shown: one NRQCD-based model predicting the cross-

section at high p_{T}, and one model that combines NRQCD and CGC, and predicts cross-sections down to low p_{T}. FONLL calculates the non-prompt contribution that is added to the prompt J/ψ cross-section. In this way, one can precisely describe the cross-section over the full transverse momentum range of the measurement.

However, there are still tensions between data and models. This is shown for example in Fig. 2.11, where the ratio $\psi(2S)$-to-J/ψ measured by ALICE at forward rapidity [19] is compared to NRQCD model. Tensions between data and NRQCD based model are also observed for polarization measurements performed by ALICE in pp collisions at $\sqrt{s}$ = 8 TeV [18] at forward rapidity.

The results shown in this section clearly show that charmonium production in pp collisions is not fully understood yet, since currently none of the models can describe all experimentally observed features simultaneously, such as production cross-sections and polarization.

Chapter 3

The ALICE detector

The work presented in this thesis is based on the analysis of data collected by ALICE (A Large Ion Collider Experiment) during the year 2017. This section contains a brief description of the experimental setup used for data taking. In the first section there is a short introduction to the Large Hadron Collider (LHC). The following section provides an overview of the ALICE detector. In particular a more detailed description is provided for the Inner Tracking System (ITS) and Time Projection Chamber (TPC) which are the most relevant detectors for the analysis presented in this thesis. Some relevant details about Particle Identification (PID) based on TPC and tracking reconstruction in ALICE are also provided.

3.1 The Large Hadron Collider

The Large Hadron Collider (LHC) is a circular particle accelerator located below ground-level in the area near Geneva, having a circumference of 27 kilometers. A schematic view of the whole LHC accelerator chain is shown in Figure 3.1. Almost 1200 supraconductive magnets provide a 8 T magnetic field. Two beams are kept seperate except for the crossing points, four areas where each of the four main experiments in CERN is located:

- ATLAS (A Toroidal LHC Apparatus)[34] and CMS (Compact Muon Solenoid)[36] are two experiments that both are designed to search for dark matter, supersymmetry, Higgs boson, in short new physics. The discovery of the Higgs boson came from these two experiments.
- LHCb (Large Hadron Collider beauty)[37] studies the CP violation in heavy flavor hadron decays. Our understanding of the asymmetry of matter and anti-matter in the Universe might be dependent on CP violation.

- ALICE (A Large Ion Collider Experiment)[33] is investigating dense and hot medium that is created in collisions of ultrarelativistic nuclei. This analysis is taking ALICE data and this experiment will be discussed more in the coming sections.

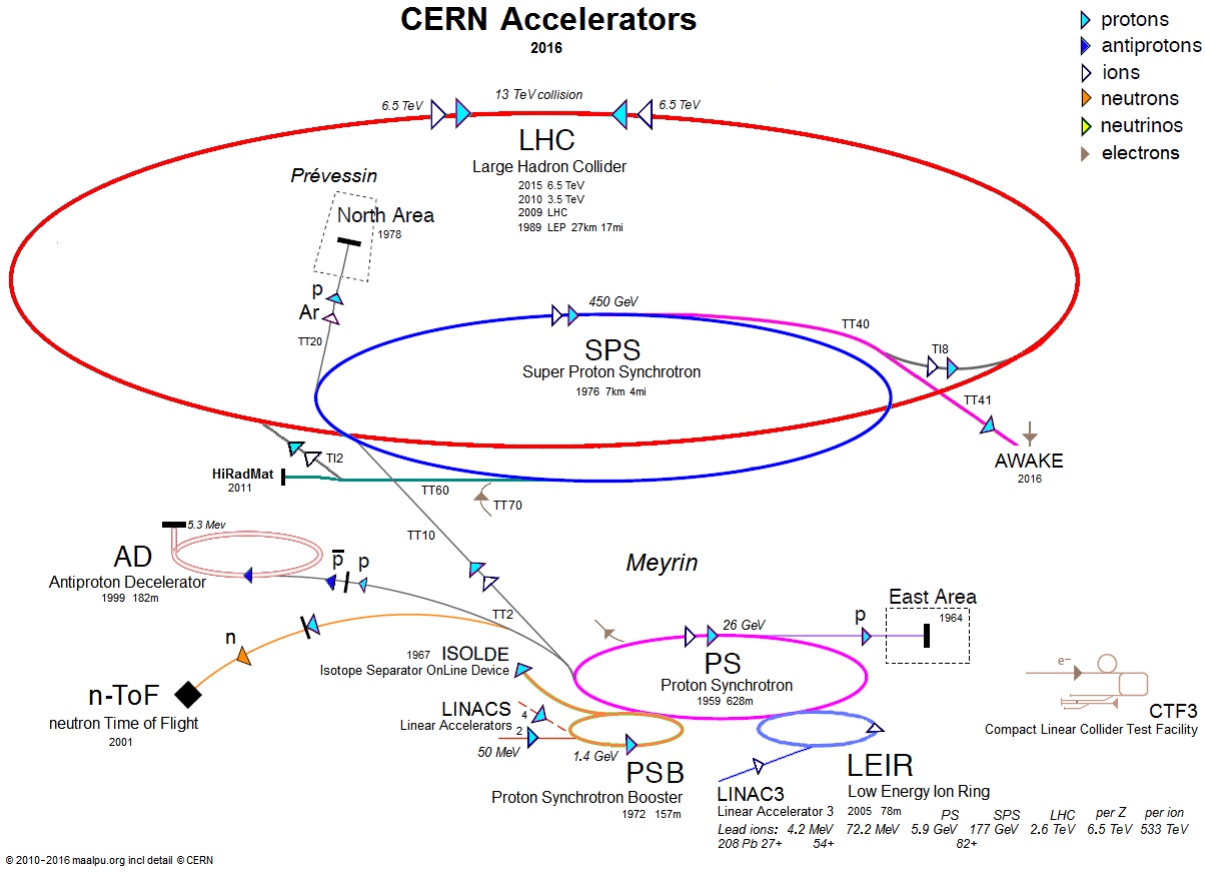

Figure 3.1: Schematic overview of the Large Hadron Collider.

3.2 The ALICE Detector

ALICE is a general-purpose, heavy-ion dedicated detector at the CERN LHC. In particular ALICE addresses physics of strongly interacting matter and quark-gluon plasma at very high energy density and temperature in nucleus-nucleus collisions. Besides heavy-ion physics, there are also important proton-proton (pp) and p-Pb programs. A special request for the ALICE detector is the capability to track and identify particles in a wide transverse momentum range, and down to very low momenta (~100 MeV/c). Precise tracking is required to reconstruct and separate the primary vertex of interaction from secondary vertices from heavy-flavor hadron decays. Both low momentum track reconstruction and precise tracking lead the request of a low material budget detector as well as a low magnetic field (0.5 T).

Central Barrel Detectors	Forward Detectors
Inner Tracking System (ITS)	Muon Spectrometer
Time Projection Chamber (TPC)	V0
Time of Flight (TOF)	T0
Transition Radiation Detector (TRD)	Zero Degree Calorimeters (ZDC)
Electronmagnetic Calorimeter (EMCal)	ALICE Diffractive (AD)
High Momentum Particle Identification detector (HMPID)	
Di-jet Calorimeter (DCal)	
Photon Spectrometer (PHOS)	
Photon Multiplicity Detector (PMD)	

Table 3.1: An overview of the subsystems of ALICE. The dimensions of ALICE are (16 x 16 x 26)m^3 and the weight is around 10 000 tons.

In ALICE there are 18 detector systems which are summarized in Tab. 3.1. Two main sections can be identified: a central barrel covering the full azimuth in the acceptance region $|\eta| < 0.9$ and several forward systems. Because of the physics requirements, each one has its own specific technology and design constraint.

The ALICE layout is shown in figure 3.2. The detector systems more relevant for the analysis presented in this thesis will be discussed in the following sub-sections.

3.2.1 Inner Tracking System

The Inner Tracking System (ITS) is the detector closest to the beam-pipe and covers a pseudo-rapidity range of $|\eta| < 0.9$. The layout of the ITS is shown in Fig. 3.3. It consists of six layers of silicon detectors that are divided into three subsystems which employ three different detector technologies. The two layers closest to the beam pipe are equipped with Silicon Pixel Detectors (SPD), then Silicon Drift Detectors (SDD) and Silicon Strip Detectors (SSD) follow with two layers each.

The main geometrical parameters of the three subsystems (inner radius, outer radius and covered pseudo-rapidity range) are summarised in table 3.2.

layers	r_{in} [cm]	r_{out} [cm]	η_{in}	η_{out}
SPD (1,2)	3.9	7.6	2.0	1.4
SDD (3,4)	15.0	23.9	0.9	0.9
SSD (5,6)	38.0	43.0	1.0	1.0

Table 3.2: Main geometrical parameters of the six layers of the ITS.

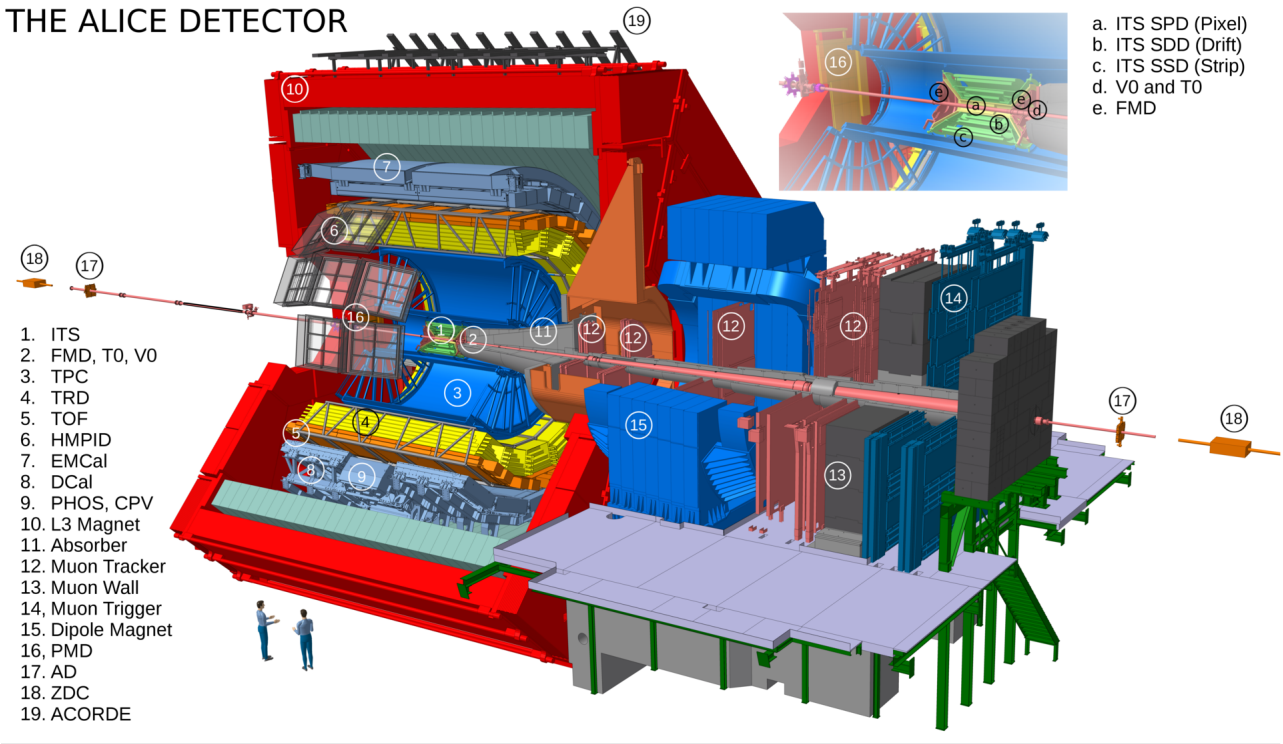

Figure 3.2: Schematic overview of the ALICE detector during the Run 2 data taking.

The number, position, and segmentation of the ITS layers, as well as the detector technologies, have been optimised in order to provide efficient track finding in the high multiplicity environment predicted for central Pb-Pb collisions at LHC, which was estimated up to 8000 particles per unit of rapidity at the time of ALICE design [38]. In addition, the ITS provides high resolution on the track impact parameter[1] and momentum measurements. The momentum and impact parameter resolution for low-momentum particles is dominated by multiple scattering effects in the material of the detector; therefore the amount of material in the active volume is kept to a minimum. In particular the total material budget for perpendicular tracks equal to 7.66% of one radiation length (X_0). In terms of position measurements, the two layers of SPD provide an excellent spatial resolution of the order of about 15 μm in the $r\phi$ plane, while the two layers of SDD have spatial precision of 28 μm in the z-direction. The two outer layers are made of double-sided silicon micro-strip detectors and have 20 μm spatial precision in the $r\phi$ plane. The most important tasks of the ITS are:

- Reconstruction of primary and secondary vertices from weakly decaying particles such as hyperons[2] and open heavy-flavored hadrons.

[1] The impact parameter is defined as the distance of closest approach of the track to the primary vertex. See also section 3.3.

[2] Baryons containing one or more strange quarks, but not charm, bottom or top.

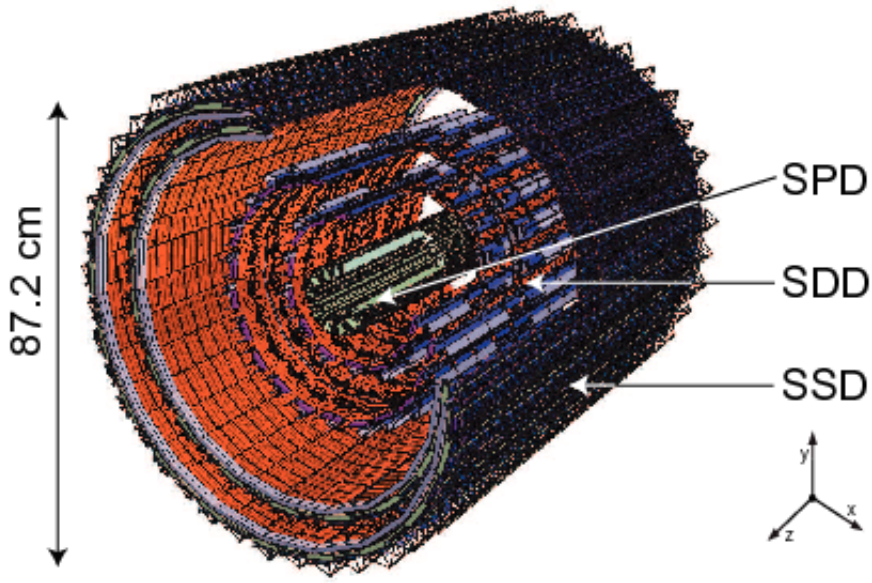

Figure 3.3: The Inner Tracking Systems with its three layers.

- Reconstructon and identification of low-momentum tracks with p < 100-200 MeV/c which are too bent by the magnetic field to be reconstructed by the TPC. The particle identification is provided by SDD and SSD layers via dE/dx measurements.
- Reconstruction and identification of those particles which traverse the dead region of the TPC.
- Improvement of the overall momentum and angular resolution of particles with high transverse momentum traveling across the TPC.

3.2.2 Time Projection Chamber

The main tracking detector in ALICE is the Time Projection Chamber, a cylindrical ionization chamber placed around the ITS. A schematic view of the detector is shown in Fig. 3.4. Although slow, the TPC is sturdy and guarantees reliability when dealing with tens of thousands of charged particles within its geometrical acceptance. The TPC provides measurement of momentum, track finding and also particle identification through specific energy loss (dE/dx) measurements.

The TPC covers the whole azimuthal angle (2π). In terms of track transverse momentum measurements, the TPC can cover from about 150 MeV/c up to several hundreds of GeV/c with good resolution. The inner and outer radius are 80 cm and 250 cm respectively. They have been chosen in order to have an average particle path length in the chamber sufficient to get a dE/dx

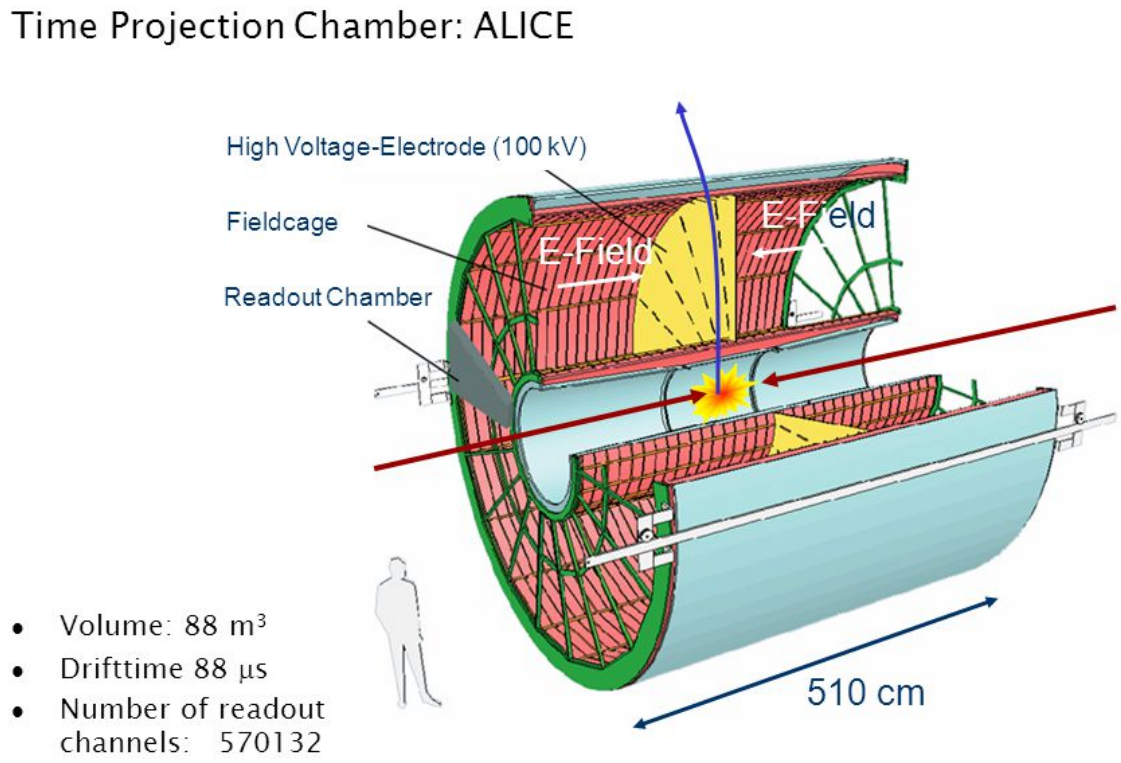

Figure 3.4: A view of the Time Projection Chamber.

resolution better than 10%. 510 cm of total active length in the z direction provides an acceptance in the pseudorapidity range $|\eta| < 0.9$. A central drift electrode divides the TPC cage, generating a drift electric field in the region of 400 V/cm. A gas-mixture of Ar (90%) and CO_2 (10%) provides the volume in which charged particles travel through in order to ionize. Free electrons then drift towards the multi-wire-proportional chambers (MWPC) situated at the endcaps with a maximum drift time of 92 μs. The signal read out by the MWPC is strengthened because of the creation of avalanches when electrons drift through the gas. From the cluster drift time and the readout position, 3D space-time points are determined in order to reconstruct particle tracks through the TPC. The transverse momentum is determined from the curvature of these tracks in the transverse plane. Low momentum leads to a stronger curve which limits the radial distance traveled in the TPC.

TPC Particle Identification

There are several subdetectors that provide PID within ALICE. The main PID detector is the TPC, which in addition to providing tracking and momentum measurement also measures the specific energy deposition of charged particles. The average energy loss for the TPC is expressed by a modified Bethe-Bloch formula [26]. The velocity of the moving charged particle is represented like this:

$$\beta = \frac{v}{c} \tag{3.1}$$

The corresponding Lorentz factor is then:

$$\gamma = \frac{1}{\sqrt{1-\beta^2}} \tag{3.2}$$

The modified Bethe-Bloch formula is:

$$\left\langle \frac{dE}{dx} \right\rangle \propto \frac{z^2}{\beta^2}(\log \frac{\sqrt{2m_e c^2 E_{\text{cut}}}\beta\gamma}{I} - \frac{\beta^2}{2} - \frac{\delta}{2}) \tag{3.3}$$

The expression yields the restricted average energy loss. The rest mass of the electron is represented by m_e, while its charge is z. The Bethe-Bloch curve is only depending on β for a given material. From this we can identify different types of particles when we know the momentum and charge. The effective excitation energy of the absorber material is represented by I, which also defines the strength of the curves. At $\beta\gamma < 0.5$ the curve decrease proportional to $1/\beta^2$. There is a broad minimum when $\beta\gamma \approx 4$. At higher $\beta\gamma$ the energy loss rises with $\log(\beta\gamma)$. δ is a correction term and parameterizes a density effect of the surrounding atoms. These get polarized by traversing charged particles and shorten the relativistic growth of energy loss at higher energies.

The analog read-out pads measure charge information associated to the clusters of a track. PID in the TPC is then made by calculating this PID signal. The read-out pads can provide up to 159 samples per track. After using a truncated mean approach, the PID signal from the distribution is extracted. This shortened PID signal can be used to separate different particle species both in the relativistic rise region and in the low momentum region of the Bethe-Bloch curve. In general, Bremsstrahlung gives an additional challenge when dealing with relativistic electrons due to their low mass. However, Eq. 3.3 parameterizes electrons well in addition to heavier particles.

It is manageable to seperate pions from electrons at low and mid momenta in the TPC with an upper limit of about 10 GeV/c. TPC also give a resolution on the specific energy deposition of

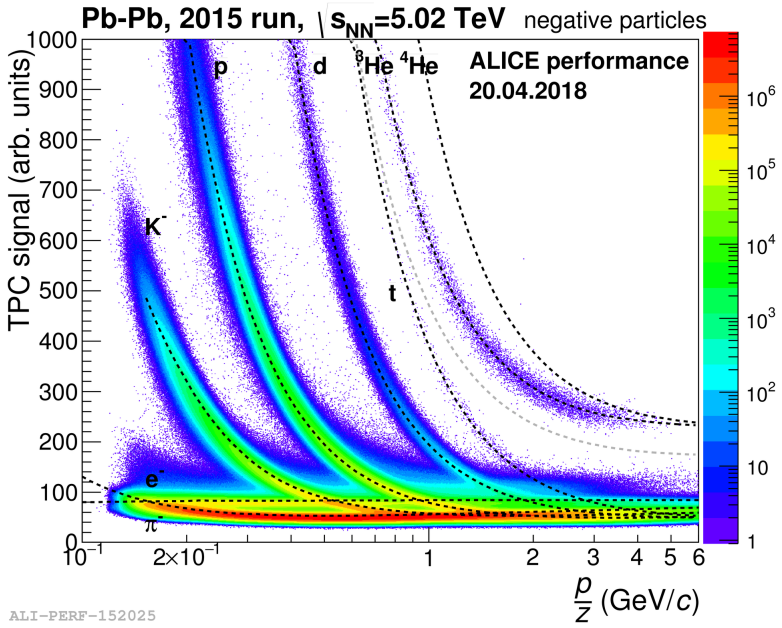

Figure 3.5: TPC-dE/dx distribution as a function of momentum for charged particles in Pb-Pb collisions at $\sqrt{s_{\mathrm{NN}}}$ = 5.02 TeV. The solid lines correspond to the calculated value of the Bethe-Bloch parametrization for different particle species. [8]

5.5%, measured by pp data and cosmic ray tracks. In Fig. 3.5 the average energy loss per track length dE/dx for given particle momentum is shown and demonstrates the particle separation power of the TPC.

3.3 Track reconstruction in central barrel

The track reconstruction in ALICE is performed using the Kalman filter approach [43], which is a robust method for statistical estimations and predictions. The Kalman Filter can be used for both track finding and track fitting simultaneously, and also provides a natural way to find extrapolation of a track from one measuring layer to another. Track reconstruction in ALICE is performed in the following steps:

1. A preliminary determination of the interaction vertex is the first action when reconstructing particle tracks. This is achieved by extrapolating linearly correlated hit pairs (tracklets) in the SPD layers.

2. A Kalman filter algorithm is used to reconstruct the tracks in the TPC. They are found by combining clusters at the outer edge of the TPC, moving towards the beam and using the primary vertex position from the previous step as seed.

3. The tracks of the TPC are then used to find tracks in the ITS, using the same method. TPC reconstructed tracks are matched to the SSD layers and followed down to the innermost SPD layer. This is done in two steps: in the first the vertex position is used, to guide track finding and maximise the efficiency for primary tracks while in the second it is not employed to recover also tracks displaced from the collision point (i.e. secondary tracks).

4. Once again the Kalman filter is used, but now information on tracks are used to propagate the track outwards to the outermost layer of the ITS and then to the outermost radius of the TPC. The tracks then try to match hits registered in the TRD and TOF subsystems.

5. The final action is to once again refit reconstructed tracks inwards in TRD, TPC, and ITS and are propagated to the primary vertex reconstructed in the first step.

6. The last step is the primary vertex recalculation using tracks. From this the precision of the determination of interaction vertex becomes higher compared to the original estimate.

At the end of the track finding procedure, the majority of the reconstructed global tracks come from the primary interaction vertex. The remaining secondary tracks, discarded or suppressed in the primary vertex fitting, represent the component of particles with a displaced origin (i.e. weak decay products of strange particles and heavy-flavor hadrons or particles from secondary interactions with the detector material). The most effective constraint for the selection of such particles is represented by the track impact parameter d_0. The impact parameter of a track is defined as the distance of closest approach of the track w.r.t. the interaction point. It can be defined separately in the transverse plane and in the direction along beam axis:

$$d_0(r\phi) = \rho - \sqrt{(x_\mathrm{v} - x_0)^2 + (y_\mathrm{v} - y_0)^2} \qquad d_0(z) = z_\mathrm{track} - z_\mathrm{v} \tag{3.4}$$

where ρ and (x_0, y_0) are the radius and the center of track projection in the transverse plane, (x_v, y_v, z_v) are the coordinates of the primary vertex position and z_track is the z position of the track after it has been propagated to the distance of closest approach in the transverse plane. The d_0 resolution depends both on the track position and on primary vertex position resolutions.
In open charm and open beauty analyses, and in particular in the analysis presented in this thesis, a good precision of the measurement of track impact parameter is of primary importance: the challenge is to reconstruct decay topologies displaced a few hundreds of μm from the primary vertex. In ALICE the measurement of the track impact parameter is provided by the ITS and mainly by the two layers of silicon pixel detectors (SPD) which have high granularity and are positioned in the proximity of the interaction region.

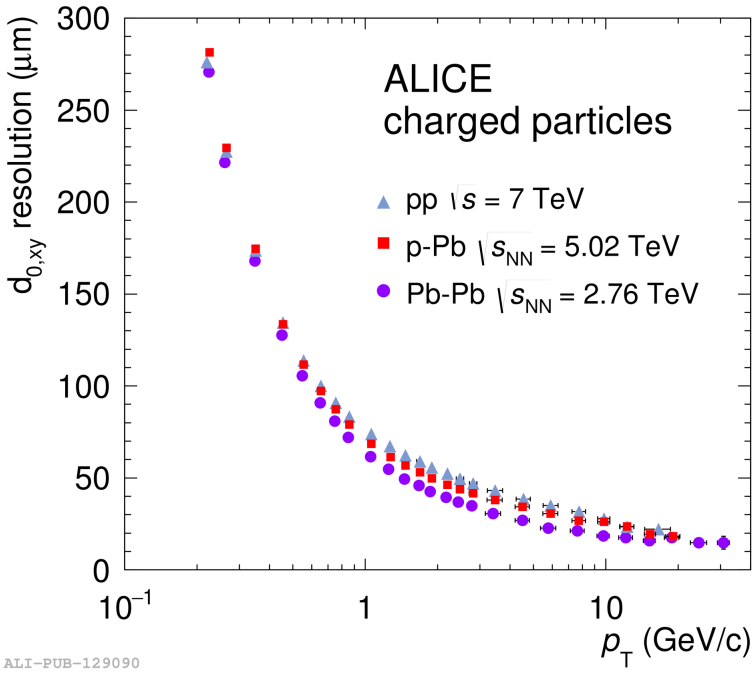

Figure 3.6: Impact parameter resolution as function of transverse momentum for different colliding systems [16]

The transverse impact parameter resolution $d_0(r\phi)$ is reported in Fig 3.6 as a function of transverse momentum, for charged particles in different colliding systems. The resolution is better than 60μm for $p_{\mathrm{T}} > 1$ GeV/c whereas it becomes worse for lower momentum. Such worsening can be attributed to the Coulomb multiple scattering, which dominantly affects low-momentum tracks. Despite the more complicated tracking procedure, the average $d_0(r\phi)$ resolution achieved in Pb-Pb and p-Pb collisions is actually improved with respect to that in pp, thanks to the more precisely determined vertex for higher multiplicity events.

Chapter 4

Analysis

As anticipated in section 2.3.1 at the LHC energies, a large fraction of J/ψ (~10% for the p_{T} integrated case) in proton-proton collisions comes from beauty hadron decays. The measurement of such fraction has a great importance for two reasons. In order to gain an accurate knowledge of the prompt charmonium production mechanisms, the adequate measurement and subtraction of the non-prompt J/ψ component from the inclusive one is mandatory. Besides this, the study of beauty hadrons decaying into J/ψ is interesting *per se* since it allows to accurately measure the beauty cross-section down to very low transverse momentum.

This chapter discusses first the concepts of prompt and non-prompt J/ψ and how to separate between them. Moving forward, the event selection and data sample will be presented in addition to the Monte Carlo sample and its tuning of the impact parameter resolution. Next, the inclusive J/ψ reconstruction with track and pair selection is listed. The analysis technique is then discussed, in particular the maximum-likelihood fit and acceptance and efficiency corrections. The different components of the likelihood function are presented and evaluated before presenting the final results of the likelihood fit. Finally, the acceptance and efficiency corrections are applied on the f_{B}.

4.1 Separation between prompt and non-prompt J/ψ

There are three different processes that contribute to the inclusive J/ψ yield measured at the LHC:

- Direct production: A c$\bar{\mathrm{c}}$ pair produced in the hard partonic scattering process combines to form a J/ψ state
- Decay from higher excited charmonium states: A produced $c\bar{c}$ pair hadronizes in a higher

mass state than J/ψ, for example χ_c or ψ(2S) state and then decays into a J/ψ state

- Decay from beauty-flavored hadrons: A $b\bar{b}$ pair from the initial hard scattering processes, hadronizes and produces a beauty flavored hadron, h_B, which decays weakly to a J/ψ state

The type of J/ψ mesons that is produced from these different processes are divided into two groups. The two former processes result in what is called "prompt" J/ψ since their production happens immediately after the collision, making it too hard to differentiate between the primary vertex and the secondary vertex. The contribution from higher charmonium states is about 35% as measured in pp collisions [41]. The latter type is referred as "non-prompt" J/ψ since beauty hadrons have a typical proper decay time of some picoseconds, which corresponds to an average proper decay length ($\sim c\tau$) of the order of several hundreds μm. After both prompt and non-prompt J/ψ mesons are produced, the charm quarks annihilate, resulting into pairs of leptons. The decay products cannot be separated experimentally from the J/ψ production vertex as the resonance is characterized by a decay width of 92.9 KeV [56]. When looking at the reconstructed dilepton tracks for prompt J/ψ, they seem to originate directly from the primary vertex. Instead, dilepton tracks from the non-prompt J/ψ point to a secondary vertex which looks displaced from the event vertex. This particular feature is exploited in the analysis discussed in this thesis in order to statistically differentiate between prompt and non-prompt J/ψ.

The signed projection $L_{xy}^{J/\psi}$ between the vertex displacement and the measured transverse momentum $\vec{p_T}^{J/\psi}$of J/ψ is a good tool used to identify the non-prompt component:

$$L_{xy}^{J/\psi} = \vec{L} \cdot \frac{\vec{p_T}^{J/\psi}}{|\vec{p_T}^{J/\psi}|}. \tag{4.1}$$

Here, $\vec{L}$ is a vector that points from the primary vertex to the secondary J/ψ reconstructed vertex. This is a good approximation of the travel length of B-hadrons before decaying to J/ψ mesons. Depending on the opening angle θ between the flight direction of the B-hadron and $\vec{p_T}^{J/\psi}$, L_{xy} can have negative and positive values. As the J/ψ is the heaviest product of b-hadron decay, it also carries most of the longitudinal momentum of the mother b-hadron, while lighter products have larger angles from the flight direction. J/ψ from high transverse momentum beauty hadrons travel almost collinear with respect to the flight direction of their mothers, resulting in positive and large measured values of L_{xy}. However, there is a significant amount of J/ψ with a large θ at low p_{T}, which contributes with small negative values of L_{xy}.

To reduce the dependence on the J/ψ transverse momentum in L_{xy}, a new variable called *pseudo proper decay length* x is introduced:

$$x = L_{xy}^{J/\psi} \cdot \frac{M_{J/\psi} c}{\vec{p}_T{}^{J/\psi}}, \tag{4.2}$$

where $M_{J/\psi}$ is the average mass of J/ψ mesons and $\vec{p}_T{}^{J/\psi}$ is the reconstructed momentum of the J/ψ meson. The name pseudo-proper decay length is used because if substituting mass and transverse momentum values of beauty hadrons in Eq. 4.1 and 4.2 in place of those of the J/ψ, x would actually be the proper decay length of the beauty hadron. Since neither the momenta nor the masses of beauty hadrons are exclusively reconstructed, the corresponding values of the J/ψ are used in the definition of the x.

As prompt J/ψ are created close to the primary interaction vertex, the distribution of the corresponding x should be close to a Dirac delta function centered around $x = 0$. Non-prompt J/ψ are vastly different, however. Their x distribution is shifted towards positive values, with an average that reflects the average b-hadron travel length before its decay into J/ψ. A graphical representation of the pseudo-proper decay length, as well as the comparison of the distributions from prompt and non-prompt J/ψ extracted from Monte Carlo simulations, are shown in Fig. 4.1, on left and right hand side respectively.

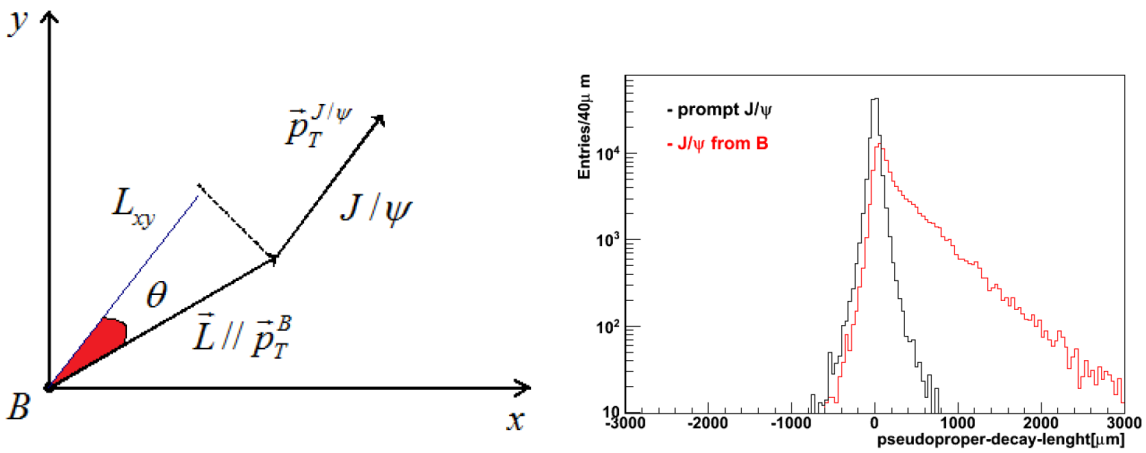

Figure 4.1: On the a graphical representation of L_{xy}. B represents the production site of the b-hadron, while xy is the transverse plane. The flight distance L of the b-hadron projects transversely with $L||P_T^B$. The transverse projected of the opening angle between the J/ψ flight directed and the b-hadron is indicated by the angle θ. On the right is the unity-normalised x distribution of prompt and non-prompt J/ψ from MC. The figure shows the qualitative difference between the two distributions. The transverse momentum is larger than 1.3 GeV/c.

4.2 Event selection and data sample

The data sample used for the analysis discussed in this thesis consists of pp collisions recorded by the ALICE detector during the year 2017. The trigger condition that is used to select events corresponds to V0-AND, which is defined to be the ALICE minimum-bias (MB) trigger. It requires hits in both the V0A and V0C detectors. The events collected in this period are further distinguished into two categories, namely MB-CENT and MB-FAST. The difference between the two configurations is related to the inclusion of the Silicon Drift Detector (SDD) in the acquisition. The SDD is the slowest among the ALICE detectors included in the data taking in pp collisions. In the MB-FAST configuration, when the SDD is busy, the event is collected without SDD. Therefore, the sample collected with the MB-FAST configuration contains all MB triggers, both with and without SDD. The sample which corresponds to MB-CENT configuration contains the events with SDD always included in the acquisition, therefore these events represent a sub-sample of MB-FAST. About 50% of the events are collected without SDD.
Three different reconstructed samples are available:

- CENT_wSDD: all events collected with the MB-CENT configuration, reconstructed *including* SDD in the tracking.
- CENT_woSDD: all events collected with the MB-CENT configuration, reconstructed *excluding* SDD from the tracking.
- FAST: all events that are collected *only* with the MB-FAST configuration (i.e. excluding common events acquired in the MB-CENT configuration).

In order to use a uniform data sample for the analysis, the sum of the events of the classes CENT_woSDD and FAST have been used [1].

The event selection also requires a reconstructed primary vertex based on global tracks with at least one of them contributing to the primary vertex. In order to have the same geometrical acceptance for all tracks, only events with a primary vertex reconstructed within a 10 cm distance along the beam line from the nominal interaction point are included. The total number of minimum bias triggered events analyzed is about $1.1 \cdot 10^9$, namely $0.394 \cdot 10^9$ and $0.699 \cdot 10^9$ for CENT_woSDD and FAST category respectively. The corresponding integrated luminosity, evaluated for inclusive J/ψ cross-section analysis [20] , is $L_{\text{int}} = 19.4 \pm 0.4 \text{nb}^{-1}$. The list of runs[2] are

[1] The same data sample was used also for inclusive J/ψ cross-section analysis [20].

[2] Here "run" referes to a discrete interval of data-taking. Usually run changes occur when something about the detector itself changes, such as trigger configuration or one or more sub-detectors need to be included / excluded from the data taking.

those suggested by the ALICE Data Preparation Group (DPG)[3] [1]. For the remaining sections, CENT will be used to indicate the CENT_woSDD sample.

4.3 Monte Carlo simulations

The Monte Carlo (MC) sample used in this analysis consists of about 50 million simulated events produced according to the PYTHIA generator [6], in which pure J/ψ signals decaying into e^+e^- pairs in the final state are injected. In particular: 70% of the generated events contain an injected prompt J/ψ generated according to p_T and rapidity distribution Y based on a phenomenological shape obtained by fitting RHIC, Collider Detector at Fermilab (CDF) and LHC data [27], while the remaining 30% of the events contain non-prompt J/ψ originating from the forced fragmentation of $b\bar{b}$ quark pairs, generated according to PYTHIA. The decay of both the prompt and non-prompt J/ψ signals is handled by the EvtGen package [3], employing PHOTOS [5] for the description of the final state radiation, accounting in particular for the NLO QED radiative J/ψ decay processes J/$\psi \rightarrow e^+e^-\gamma$ ("internal bremsstrahlung" processes). All the simulated particles are then propagated through a realistic description of the ALICE set-up, based on GEANT3 transport code [4], which takes into account the time evolution of the whole detector performance and data taking conditions. The generated Monte Carlo events are treated similarly to data by the offline framework, employing the same detector setup and configuration as the one in real data. There are two sets of MC, simulated according to the corresponding setup of CENT and FAST samples.

Tuning of the impact parameter resolution

Several key ingredients of the analysis are extracted from MC simulations. The method of tuning is in general a procedure that makes the MC mimic some features of real data. For the analysis presented in this thesis the resolution on the pseudo-proper decay length x, indicated in the rest of the document by $R(x)$, is one of the most important elements estimated from simulated data. $R(x)$ is strictly correlated to the impact parameter ($d_0(r\phi)$) resolution of the tracks in the transverse plane (discussed in Sec. 3.3).

By comparing single track impact parameter resolutions and averages from MC and data, one can quantify the discrepancy and correct it artificially. The procedure used for such correction, called "hybrid method" [40], consists in an on-the-fly rescaling of the residuals of the track impact parameters in the transverse plane with respect to their true kinematic values, in order to match the values observed on data. Thanks to this procedure it is possible to minimize possible biases in the estimation of the resolution R(x) from the MC sample.

[3] The Data Preparation group is responsible for steering and coordinating the reconstruction of the data collected by Alice and the preparation and the execution of the Monte Carlo simulations.

In particular the reconstructed impact parameter distributions of tracks are fitted with a gaussian shape term, related to prompt tracks, plus a symmetric exponential describing the long-range distribution tails. The fitted values of μ and σ of the gaussian are taken as average and resolution (RMS), respectively. The fits of impact parameter distributions, from both data and Monte Carlo, are reported in appendix A for all studied cases.

There are two separate comparisons considered in these studies:

- Data and MC-general purpose are compared separately for CENT and FAST samples. This is done because it is crucial to know whether we can rely on MC to determine the resolution of the pseudo-proper decay length (x). DCA corrections are used on MC to match IP resolution and average as observed in the data.
- CENT and FAST are also compared. If there are no significant differences, these two periods can be merged both for actual and simulated data in order to perform the analysis.

The quantities considered to perform such comparisons are the RMS and the average of the impact parameter distributions, determined as described above. In order to make a quantitative comparison the ratios of the RMS and the differences of the averages are considered.

As seen in Fig. 4.2, the impact parameter resolutions for single tracks are better in MC than actual data. The discrepancy is about 20% at high p_{T} for the RMS. Also the averages of IP distributions are not well reproduced, as indicated by the shift in the bottom-left figure, especially at lower p_{T}. Fig. 4.3 shows the results after the tuning procedure is applied on the MC. The discrepancy between data and MC is significantly reduced. From a residual discrepancy of about 20% before the correction, to a residual discrepancy of less than 3%, which is good enough to proceed with. The 3% discrepancy is taken into account in the study of systematic uncertainties on the resolution function.

As discussed above, the goal is to merge the CENT and FAST clusters when doing the analysis. The comparisons shown in Fig. 4.4 show that for both the MC after correction and the actual data, the CENT and FAST clusters have very similar trends of impact parameter resolutions and averages, with a residual difference less than 1%. The two periods will be merged to perform the likelihood fit analysis.

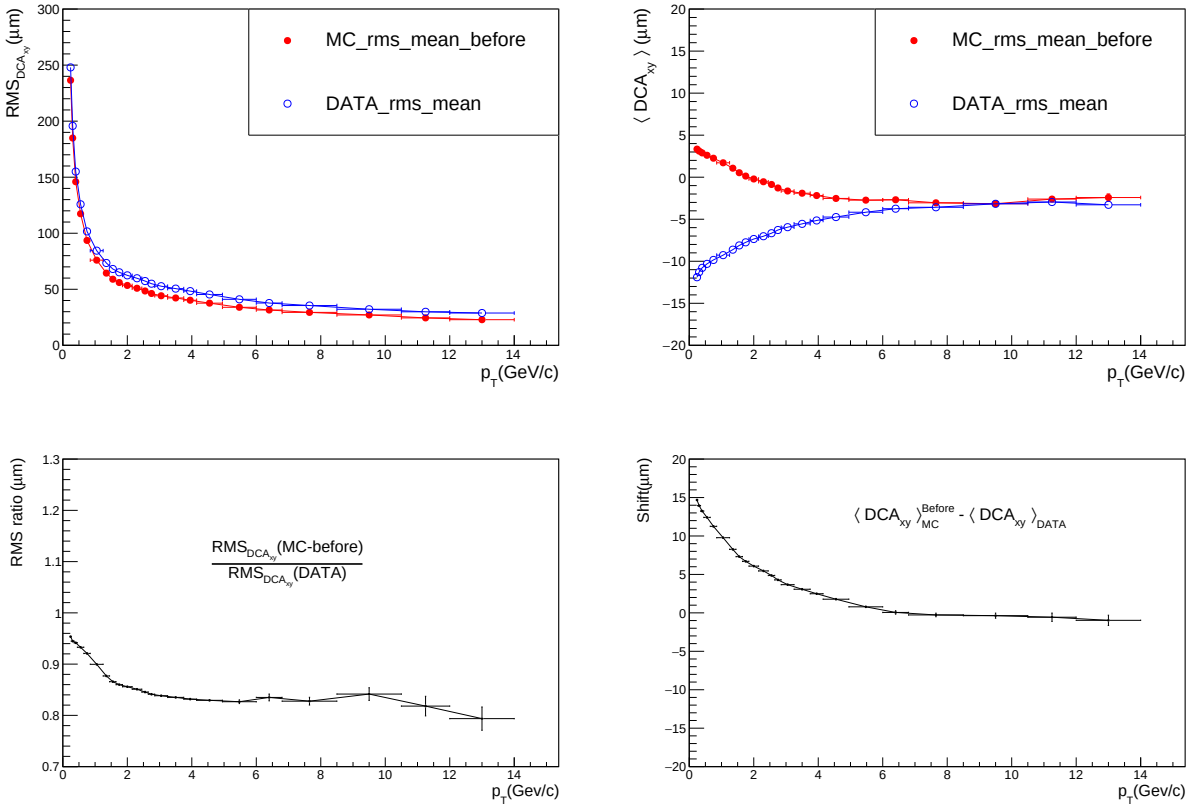

Figure 4.2: Comparison of the CENT MC sample before DCA corrections with the CENT data sample. On the left is a comparison of the RMS values and the ratio between them. On the right is a comparison of the averages and the difference between them.

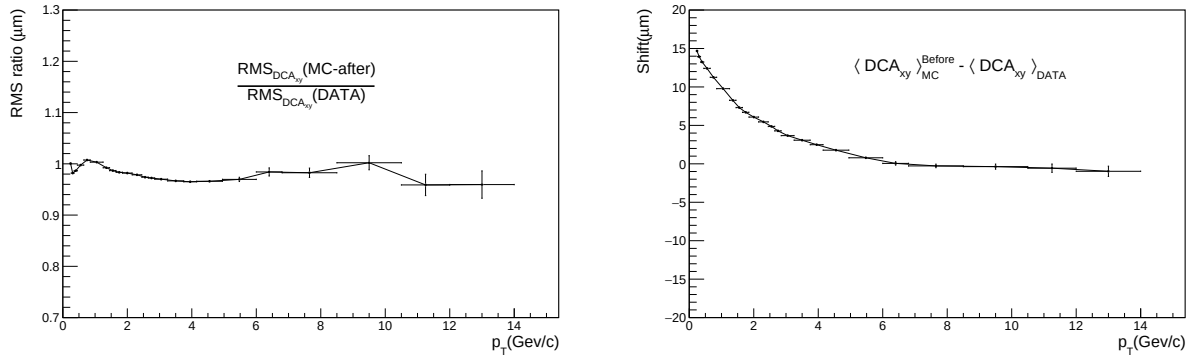

Figure 4.3: Comparison of the CENT MC sample after DCA corrections with the CENT data sample. On the left is the ratio between the RMS values. On the right is the difference between the averages.

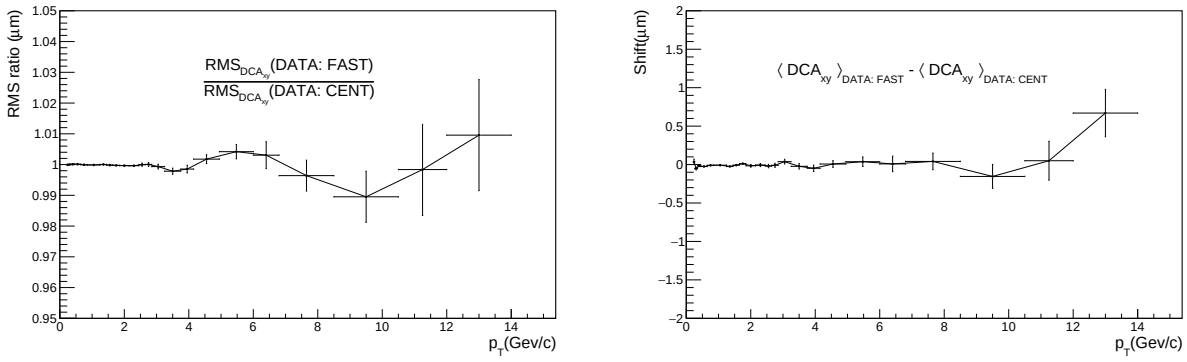

Figure 4.4: Comparison between the FAST and CENT data clusters. On the left is the ratio between the RMS values. On the right is the difference between the averages.

4.4 Inclusive J/ψ reconstruction

The extraction of the inclusive signal is performed by selecting all track pairs which are compatible with being the product of a J/ψ decaying into a e^+e^- pair. A pairing algorithm combines opposite sign track pairs that fulfill several different selection criteria. These are made in order to maximize the rejection of background without missing a significant fraction of signal candidates. Several kinematic and quality selections as well as particle identification procedures are applied in order to select electron candidates. Then the invariant mass for all selected electron-position pairs is evaluated and further cuts are applied at the level of dielectron pair variables, such as transverse momentum and rapidity. All selection criteria are summarized in table 4.1:

The following subsections provide explanations for the different selection criteria.

4.4.1 Track selection

Kinematic selection

In order to remove a non-negligible amount of combinatorial background from electrons with low momentum, we require that the transverse momentum p_T has to be above 1 GeV/c. As J/ψ mesons have large mass, each electron receives large momentum and not much signal of the J/ψ is lost due to the momentum selection. This also excludes partially kaons and protons. The pseudorapidity $|\eta| < 0.9$ corresponds to the requirement on the polar angle θ of the electron track between 45° and 135°.

Task	Action
p_T	> 1 GeV/c
$\|\eta\|$	< 0.9
$\|DCA_{xy}\|$	< 0.2 cm
$\|DCA_z\|$	< 0.4 cm
kITSrefit	request
TPCrefit	request
kink daughters	reject
matching with SPD	SPDany
ITS χ^2 per cluster	< 36
number of ITS shared clusters	At most 1
number of TPC clusters	> 70
TPC χ^2 per cluster	< 4
p_T of conversion partner	< 300 MeV/c
invMassPair	< 50 MeV/c^2
electron inclusion	-2,3 σ
p and π rejection	-3,3 σ

Table 4.1: A summary of the different conditions and restrictions applied for this analysis. The table is divided into several sections, which include (from the top) the kinematic selection, track quality selection, PID selection and rejection of electrons from photon conversions.

Track quality selection

TPC requirements: In order to count the event, each track needs to have 70 at the minimum of the in total 159 clusters in the TPC. The value of TPC χ^2 per cluster that is obtained in the momentum fit is required to be less than 4, which is the standard value employed in ALICE. A successful TPC refit is also required.

ITS requirements: A successful ITS refit is needed for all reconstructed tracks, which means at least two out of six possible clusters in the silicon layers of the ITS. ITS χ^2 per cluster needs to be below 36 and no more than one cluster can be shared in the ITS. In addition to this, the requirement of at least one hit in one of the two SPD layers, the two innermost layers of the ITS.

Impact parameter requirements: Distance of closest approach (DCA) restrictions to the primary vertex are applied both in the transverse ($|DCA_{xy}| < 0.2$ cm) and longitudinal ($|DCA_z| < 0.4$ cm) plane.

Rejection of "kink": tracks compatible with a kink [4] decay topology have been excluded.

[4] Kinks are topological signature of charged particles decaying into one charged plus one neutral particle, where the latter is not reconstructed. These decays are called kinks because the daughter track intersect the mother at a different angle, making a 'kink' in the decay vertex.

Particle identification selection

As discussed earlier, the strategy of PID is to identify particles based on the specific energy loss measured by TPC. The number of TPC sigmas, $n\sigma_{\mathrm{TPC}}$, is the basis for the selection and defined in Eq. 4.3:

$$n\sigma_{\mathrm{TPC,i}} = \frac{\frac{dE}{dx_{\mathrm{meas}}} - \langle \frac{dE}{dx_{exp,i}}(\beta\gamma, p_{in}, N_{\mathrm{clsPID}}, \eta)\rangle}{\sigma_i(\beta\gamma, p_{\mathrm{in}}, N_{\mathrm{clsPID}}, \eta)}, \tag{4.3}$$

where i accounts for the particle species and dE/dx_{meas} represents the TPC measured specific energy loss. The second term corresponds to expected energy for the particle species i parameterized as a function of the parameters β_γ at the inner wall of the TPC, the number of TPC clusters with PID information N_{clsPID} and the η of the track. The resolution is σ.

The number of σs in TPC are ideally Gaussian distributions with mean zero and width one. But in reality, this varies with η due to detector effects. In order to identify electrons properly, the TPC-PID is calibrated to account for dependencies.

In this analysis the tracks of electron candidates of J/ψ decays have to be within a range of [-2,3] σ from the expected values. Also, tracks having a $n\sigma_{\mathrm{TPC,p}}$ and $n\sigma_{\mathrm{TPC},\pi}$ lower than 3 are rejected. Thanks to this selection the hadron contamination is greatly reduced from the sample of selected candidates.

Rejection of electrons from photon conversions

In order to further identify and remove electrons from photon conversions, “pre-filter” cuts have been applied. Photons may induce additional background components by creating additional pairs of electrons, which can combine with other electron candidates selected in the same event, resulting in "fake" J/ψ decay candidates. All legs of dielectrons identified by an V0-finder algorithm [16] are discarded, rendering them ineligible for pairing. In addition some additional topological selections are applied: minimum transverse momentum of candidate electron larger than 300 MeV/c and requiring that the invariant mass of the pair is below 50 MeV/c^2. This results in a significant component of the background removed, in particular at lower p_{T}, with a negligible effect on the J/ψ yield, as studied in the previous pp analyses [12].

4.4.2 Pair selection

The cuts listed in table 4.2 give the basis for the pair selection.

Task	Action
$\|Y\|$	< 0.9
p_{T}	2-10 GeV/c
Candidates	FF and FS

Table 4.2: A summary of the pair selection conditions in this analysis.

There are some cuts done on the reconstructed J/ψ candidates after pairing. One of the conditions is the rapidity $|Y|$ of the mother which is required to be less than 0.9. The transverse momentum p_{T} is also a factor that is important to look at as at low p_{T} one could benefit from the higher statistics, but the resolution on the pseudo-proper decay length becomes worse, and the separation power between prompt and non-prompt J/$\psi$is limited. At high p_{T} the resolution improves, but there are few statistics. In this thesis the integrated p_{T} region is set to [2,10] GeV/c^2. In addition to that, there is one more important restriction that is done. The SPD has two layers and one can classify J/ψ candidates into three categories depending on if the first layer has a reconstructed point ("hit") or not. The candidates classified as first-first (FF) have both legs with one hit reconstructed in the first layer of the SPD. First-second candidates (FS) have only one track that satisfies this requirement, while the other one has a reconstructed hit only in the second layer of the SPD. The last type is the second-second candidates (SS), for which both legs only have hits in the second layer of the SPD. As the precision in the reconstructed decay vertex is better when reconstructed hits are closer to the primary vertex, the resolution is best for FF candidates with FS following closely. The SS candidates have very poor resolution. In addition the total amount of entries are only about 10% of all candidates. Thus, SS candidates are discarded for further analysis, and only the combination of FF and FS candidates are taken into account.

4.5 Analysis Technique

The goal of this analysis is to measure the fraction of the total reconstructed J/ψ that come from the beauty hadron decays. There are several different components that contribute to the reconstructed candidates and in this analysis these components are mainly classified based on the observable pseudo-proper decay length. In order to perform a statistical separation, the principle of maximum likelihood fit is used. In particular a simultaneous two dimensional fit to the pseudo-proper decay length and invariant mass of J/ψ candidates is performed. Given some statistical models, this estimates the non-prompt J/ψ fraction based on the sample that is experimentally measured. The standard approach, that will be explained in the following, was originally introduced by CDF Collaboration [22], and represents the fundamental approach adopted also by all the other LHC experiments in similar analyses.

4.5.1 Maximum-likelihood fit

An un-binned two-dimensional likelihood fit is used in order to measure the non-prompt fraction of the J/ψ yield. This is done on both the x distribution of selected dielectron pairs in addition to the invariant mass $m_{e^+e^-}$, which both are experimentally measured. The nature of the candidates are reasonably described by this statistical interpretation.

When specifying an invariant mass interval, the fractions of signal, background, prompt and non-prompt characterize the probability distribution of x or $m_{e^+e^-}$. The underlying Probability Distribution Function (PDF) will then have these as unknown parameters, which can be estimated practically. By having a sample of N repeated measurements, the estimation comes from maximizing the quantity:

$$\ln\{L\} = \sum_{i=1}^{N} \ln\{F(x^i, m^i_{e^+e^-})\}. \tag{4.4}$$

The total number of J/ψ candidates in the given invariant mass interval is represented by the sum of Eq. 4.4. The probability of observing a J/ψ candidate, which can either be signal or background, is described by the likelihood term F(x,$m_{e^+e^-}$) with the given value of invariant mass and pseudo-proper decay length. Given that the two variables are independent, which is for certain in Monte Carlo, one can then express F:

$$F(x, m_{e^+e^-}) = f_{\text{Sig}} \cdot F_{\text{Sig}}(x) \cdot M_{\text{Sig}}(m_{e^+e^-}) + (1 - f_{\text{Sig}}) F_{\text{Bkg}}(x) \cdot M_{\text{Bkg}}(m_{e^+e^-}). \tag{4.5}$$

Eq. 4.5 consists of one-dimensional density functions. $F_{\text{Sig}}(x)$ and $F_{\text{Bkg}}(x)$ are PDFs that describes the pseudo-proper decay length x distribution of respectively signal and background candidates. $M_{\text{Sig}}(m_{e^+e^-})$ and $M_{Bkg}(m_{e^+e^-})$ are also PDFs, but these represent the dielectron invariant mass distributions for signal and background. f_{Sig} is the fraction of signal candidates inside the given mass interval. This fraction is congruent with Signal/(Signal+Background), a ratio used to find how much signal there is compared to the background. (1-f_{Sig}) equals f_{Bkg} and stands for the background fraction.

It is also possible to factorize $F_{\text{Sig}}(x)$ into parts describing prompt and non-prompt J/ψ with respect to x:

$$F_{\text{Sig}}(x) = f^{'}_{\text{B}} \cdot F_{\text{B}}(x) + (1 - f^{'}{}_{\text{B}}) \cdot F_{\text{Prompt}}(x). \tag{4.6}$$

In this case $F_{\text{Prompt}}(x)$ is the PDF for prompt J/ψ and $F_{\text{B}}(x)$ is the PDF for non-prompt J/ψ signal. $f^{'}_{\text{B}}(x)$ stands for measured fraction of J/ψ from decays from beauty-hadrons:

$$f'_{\mathrm{B}} = \frac{N_{\mathrm{J}/\psi<-h_{\mathrm{B}}}}{N_{\mathrm{J}/\psi<-h_{\mathrm{B}}} + N_{\mathrm{Prompt\,J}/\psi}}. \tag{4.7}$$

In section 4.1 one key difference between non-prompt and prompt J/ψ is that a prompt J/ψ decays at once, at the primary vertex. As a consequence, the pseudo-proper decay length distribution $F_{Prompt}(x)$ can be treated as coincident with the pseudo-proper decay length resolution function $R(x)$:

$$F_{\mathrm{Prompt}}(x) = \delta(x') \otimes R(x'-x) = R(x), \tag{4.8}$$

which describes the experimental accuracy by which x can be reconstructed. The resolution function is used in all the x-related PDFs in the convolutional product with their kinematic distributions.

In theory, one can select by using the maximum likelihood method the best set of estimators of unknown parameters given the knowledge of the true underlying PDFs. This is because of the fact that the shape of each PDF is coincident with the shape of the distribution of an infinite number of observations plotted with infinitesimally small intervals. In practice, the model is not known and information comes from parametrization of functional shapes with some reasonable parameters. The unknown parameters are then extracted. In this case possible biases will have to be taken into account in the systematic uncertainties.

In this analysis, evaluating the PDF terms in Eq. 4.6 through fits on distributions taken from data or MC, and fixing them in the un-binned likelihood fit, leads to the extraction of the non-prompt fraction $f'_{\mathrm{B}}(x)$. Leaving $f'_{\mathrm{B}}(x)$ and $f_{\mathrm{Sig}}(x)$ as free parameters, the likelihood fit is performed on all candidates in the chosen invariant mass range 2.2 $GeV/c^2 < m_{\mathrm{e^+e^-}} < 4.0\ GeV/c^2$. Statistical uncertainties on the two free parameters and the effects of their correlations are evaluated together. The study of systematic uncertainties in chapter 5 will then look at all assumptions made on the former fixed PDFs.

4.5.2 Correction of acceptance and efficiency

Likelihood fits give the measured fraction $f'_{\mathrm{B}}(x)$ of J/ψ which is the non-prompt fraction of the reconstructed inclusive J/ψ yield. However, the actual fraction $f_{\mathrm{B}}(x)$ of J/ψ from decay of beauty hadrons is different. The difference comes from acceptance and reconstruction efficiencies $< A \times \epsilon >$ between prompt and non-prompt J/ψ. In order to find the actual fraction $f_{\mathrm{B}}(x)$, one has to apply a correction that accounts for the different average $< A \times \epsilon >$, a step that is needed to do for each p_T interval.

$$f_B = \left(1 + \frac{1 - f'_B}{f'_B} \cdot \frac{\langle A \times \epsilon \rangle_B}{\langle A \times \epsilon \rangle_{Prompt}}\right)^{-1} \tag{4.9}$$

Eq. 4.9 is the relation between $f'_{\mathrm{B}}(x)$ and $f_{\mathrm{B}}(x)$. Given that all J/ψ are assumed to be unpolarized, the only difference to <A x ϵ> between non-prompt and prompt J/ψ is the kinematic p_T distribution. This assumption is justified by the latest J/ψ polarization measurement in pp collisions at the LHC [45], where polarization was found to be very small. As distributions in kinematic p_T are quite similar for prompt and non-prompt J/ψ, the actual value of the non-prompt fraction $f_{\mathrm{B}}(x)$ is very similar to $f'_{\mathrm{B}}(x)$, with the relative change being in the range of a few percent.

4.6 Components of the Likelihood Function

Eq. 4.5 is a function consisting of multiple components put together. This section goes through all of them, explaining their origins, and how they are determined for the unbinned likelihood fit. Evaluation of the components is done on all p_{T}bins (2-4, 4-5, 5-7, 7-10) GeV/c in addition to the integrated case (2-10) GeV/c.

4.6.1 Resolution function R(x)

$R(x)$ in Eq. 4.5 is a PDF and represents the experimental resolution on the pseudo-proper decay length. This function is extracted from MC simulations with injected J/ψ, after the procedure of tuning of the impact parameter resolution discussed in section 4.3 is applied. The resolution on x is basically coincident with the PDF that describes the pseudo-proper decay length distribution of prompt J/ψ reconstructed after all selection cuts. R(x) is studied as a function of the transverse momentum and separately for each candidate type (FF, FS and SS[5] candidates).

The functional form employed to describe $R(x)$ is based on the same parametrization used by the CDF experiment:

$$R(x) = \omega_1 \cdot G_1(x; \mu_1, \rho_1) + \omega_2 \cdot G_2(x; \mu_2, \rho_2) + \omega_3 \cdot f(x; \alpha, \lambda)\,. \tag{4.10}$$

Here both G_1 and G_2 are Gaussian functions:

$$G(x; \mu, \rho) = \frac{1}{\sqrt{2\pi\rho^2}} e^{-\frac{(x-\mu)^2}{2\rho^2}}\,. \tag{4.11}$$

[5] SS candidates have been excluded for the final result. However, for completeness the study of the resolution was carried on including them as well.

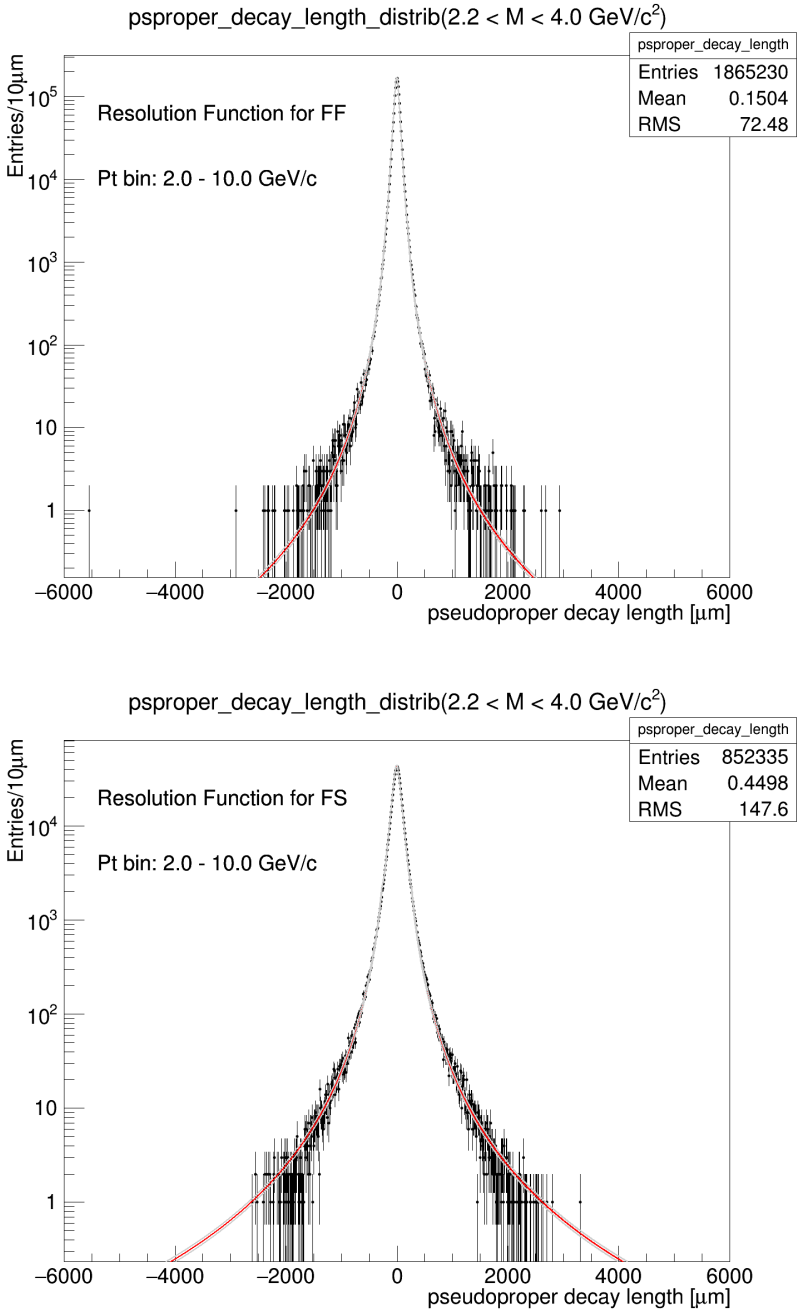

Figure 4.5: Resolution function fitted on FF and FS candidates for the integrated case.

The symmetric power law term has a step-wise form:

$$f(x;\alpha;\lambda) = \begin{cases} \frac{\lambda-1}{2\alpha\lambda} & |x| < \alpha \\ \frac{\lambda-1}{2\alpha\lambda}\alpha|x|^{-\lambda} & |x| > \alpha \end{cases} . \tag{4.12}$$

The coefficients ω_1, ω_2 and ω_3 are all weights that make the sum of the weights in Eq. 4.10 equal

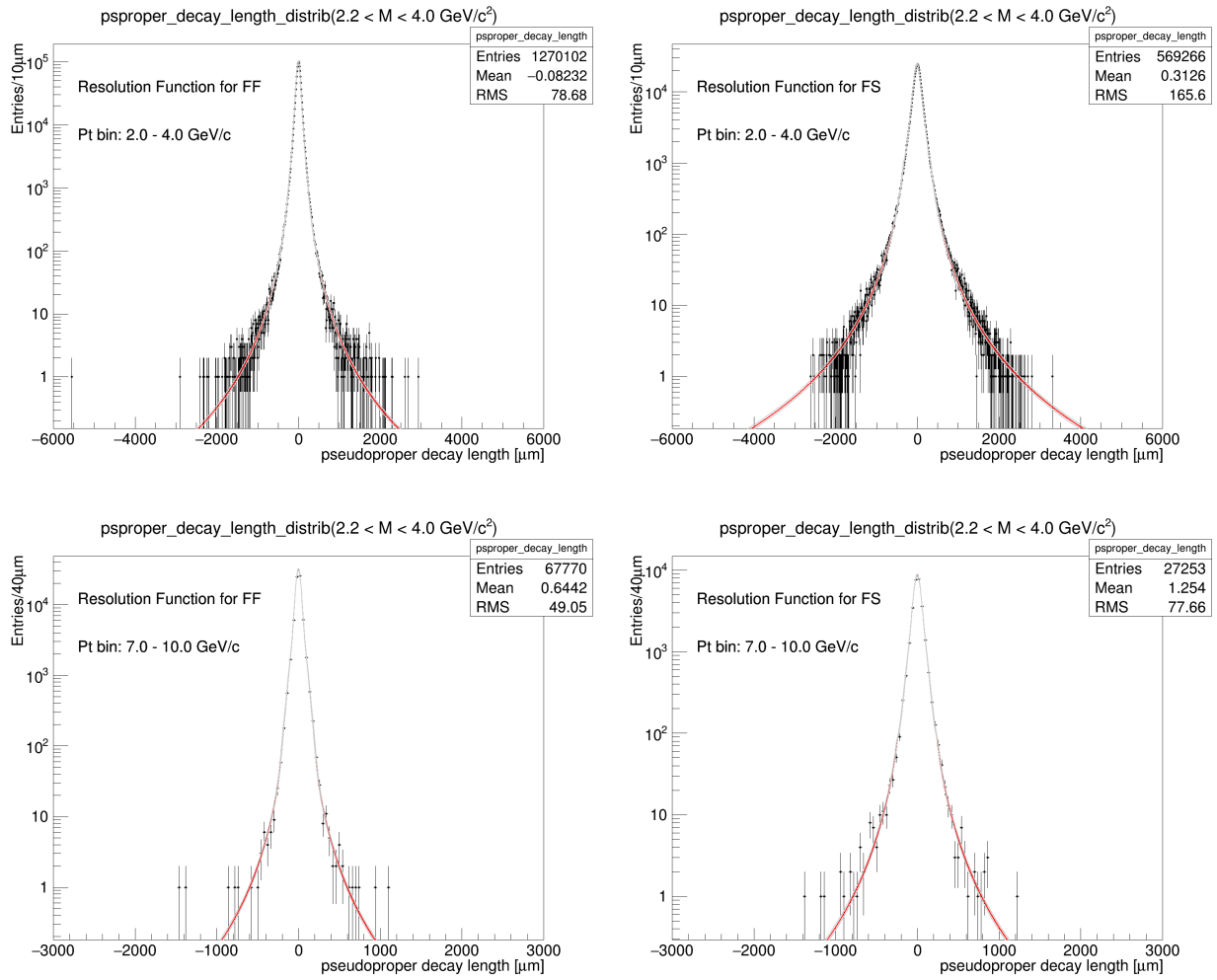

Figure 4.6: Resolution function fitted on FF and FS candidates for p_{T} [2,4] and [7,10] GeV/c.

to 1 since PDFs have to have such a property of unity. Some fit examples of the resolution function for FF (top panel) and FS (bottom panel) candidates are shown in Fig. 4.5, which refers to the case integrated over p_{T}. The corresponding fits in the lowest and highest p_{T} bins used in this analysis are shown in Fig. 4.6. Resolution functions for all p_{T} bins are reported in appendix A. In Fig. 4.7 the widths (Root Mean Square (RMS)) of the resolution function before and after the impact parameter tuning procedure are shown for different candidate types. From the figures it is clear how the smearing procedure results in a higher RMS value, which lies more closely to the resolution of the actual data.

In Fig. 4.8 the RMS of the resolution function are compared between CENT and FAST samples, for all candidate types. From the comparison it is possible to conclude that the CENT and FAST clusters are very similar, further reinforcing that it is possible to safely merge them.

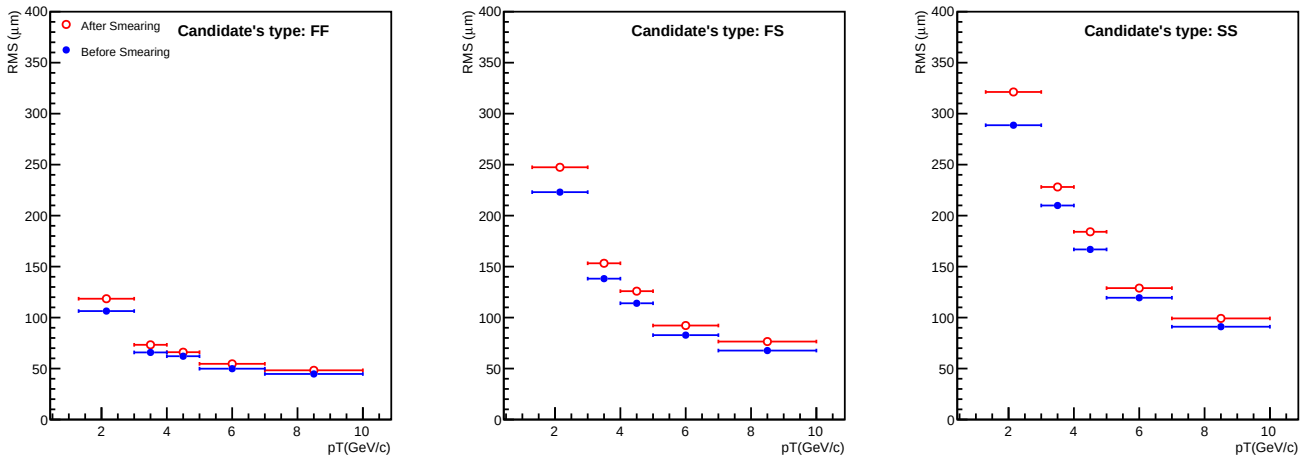

Figure 4.7: Comparison of RMS of resolution functions for all candidate types, including SS. The comparison is between MC resolutions before and after the DCA corrections are applied. Notice the high RMS values of the SS candidates.

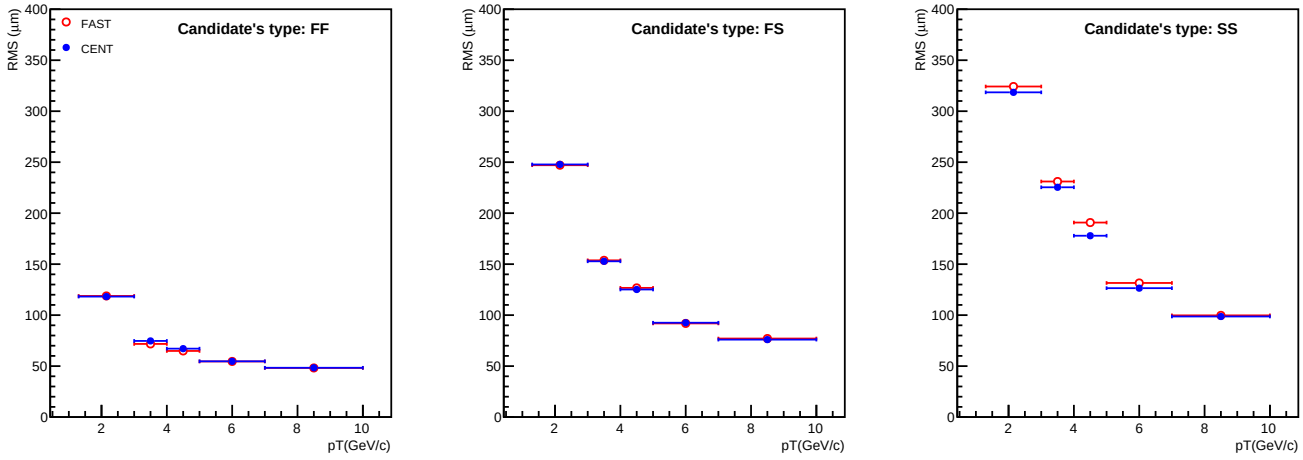

Figure 4.8: Comparison of RMS of resolution functions on all candidate types, including SS that is discarded later. The comparison is between the CENT and FAST MC clusters after the DCA corrections are applied.

4.6.2 Background x PDF F_{Bkg}

In order to obtain a good fit to the data outside the signal region, a more complicated parametrization for the background of the pseudo-proper decay length component is needed. The CDF parametrization is used for the fitting of $F_{\mathrm{Bkg}}(x)$, in particular four parts compose the pseudo-proper decay time background function: The zero lifetime component, an exponential function

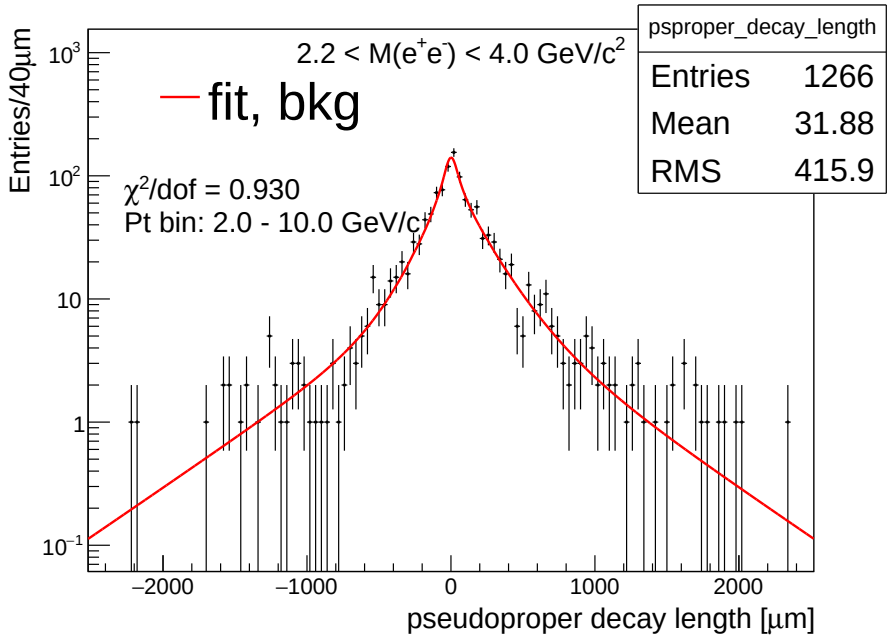

Figure 4.9: Pseudo-proper decay length background fits performed on J/ψ candidates in the integrated case.

with a positive slope, a negative slope exponential function and a symmetric exponential function with both positive and negative slopes. Background from other long-lived b-hadron events producing opposite sign muons such as b$\rightarrow c\mu^{-}\overline{\nu}X$ and $c \rightarrow \mu^{+}\nu X$ is modeled by the positive slope exponential function. The zero lifetime component is chosen to be the same shape as the resolution function. Finally, the symmetric and negative slope exponential functions parameterize the components that remain of the background pseudoproper decay time distributions, originating from sources that are unknown. The tails of the background exponentials are convoluted with the resolution function as well.

The functional form described above is given by:

$$\begin{aligned} F_{\mathrm{Bkg}[m_{\mathrm{inv}},p_T,type]}(x) &= \frac{f_+}{\lambda_+} e^{-\frac{x'}{\lambda_+}} \cdot \theta(x') + \frac{f_-}{\lambda_-} e^{\frac{x'}{\lambda_-}} \cdot \theta(-x') + \frac{f_{\mathrm{Sym}}}{2\lambda_{\mathrm{Sym}}} e^{-\frac{|x'|}{\lambda_{\mathrm{Sym}}}} \\ &+ (1 - f_+ - f_- - f_{\mathrm{Sym}}) \cdot \delta(x')]_{m_{\mathrm{inv}}} \otimes R_{p_T,type}(x - x') \,. \end{aligned} \tag{4.13}$$

The first term is proportional to $R(x)$. The remaining three exponential functions, (symmetric, positive, and negative) are convoluted with the resolution function. The coefficients (f_-, f_+, f_{Sym}) represent the weights of each component and their sum is set to 1 in order to assure the proper normalization for the total PDFs.

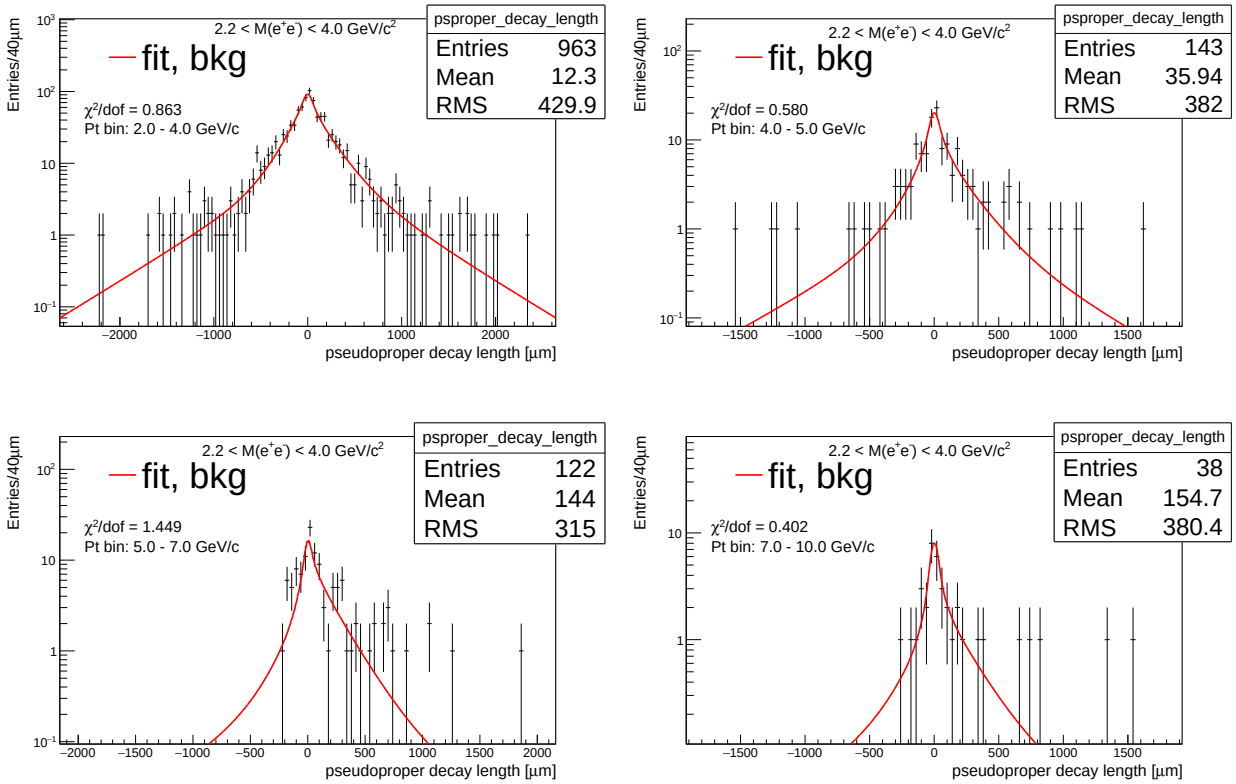

Figure 4.10: Pseudo-proper decay length background fits performed on J/ψ candidates in p_{T}intervals [2,4], [4,5], [5,7] and [7,10] GeV/c

The complex nature of this parametrization stems from an order of different factors. Random combinations of electrons from semi-leptonic decays of beauty and charm hadrons introduce asymmetries in the observed distributions that should result in making the positive tail more pronounced. Tracks that are either secondary or not reconstructed properly can give x values on both sides of the vertical axis. Fig. 4.9 and 4.10 show the results for the p_{T} integrated and p_{T} differential case, respectively.

4.6.3 Non-prompt x PDF F_B

$F_{\mathrm{B}}(x)$ in Eq. 4.5 is the probability function that is related to the reconstructed non-prompt J/ψ distribution. It is defined by Eq. 4.14:

$$F_{\mathrm{B}[p_T,type]}(x) = \chi_B(x') \otimes R_{p_T,type}(x)\,. \tag{4.14}$$

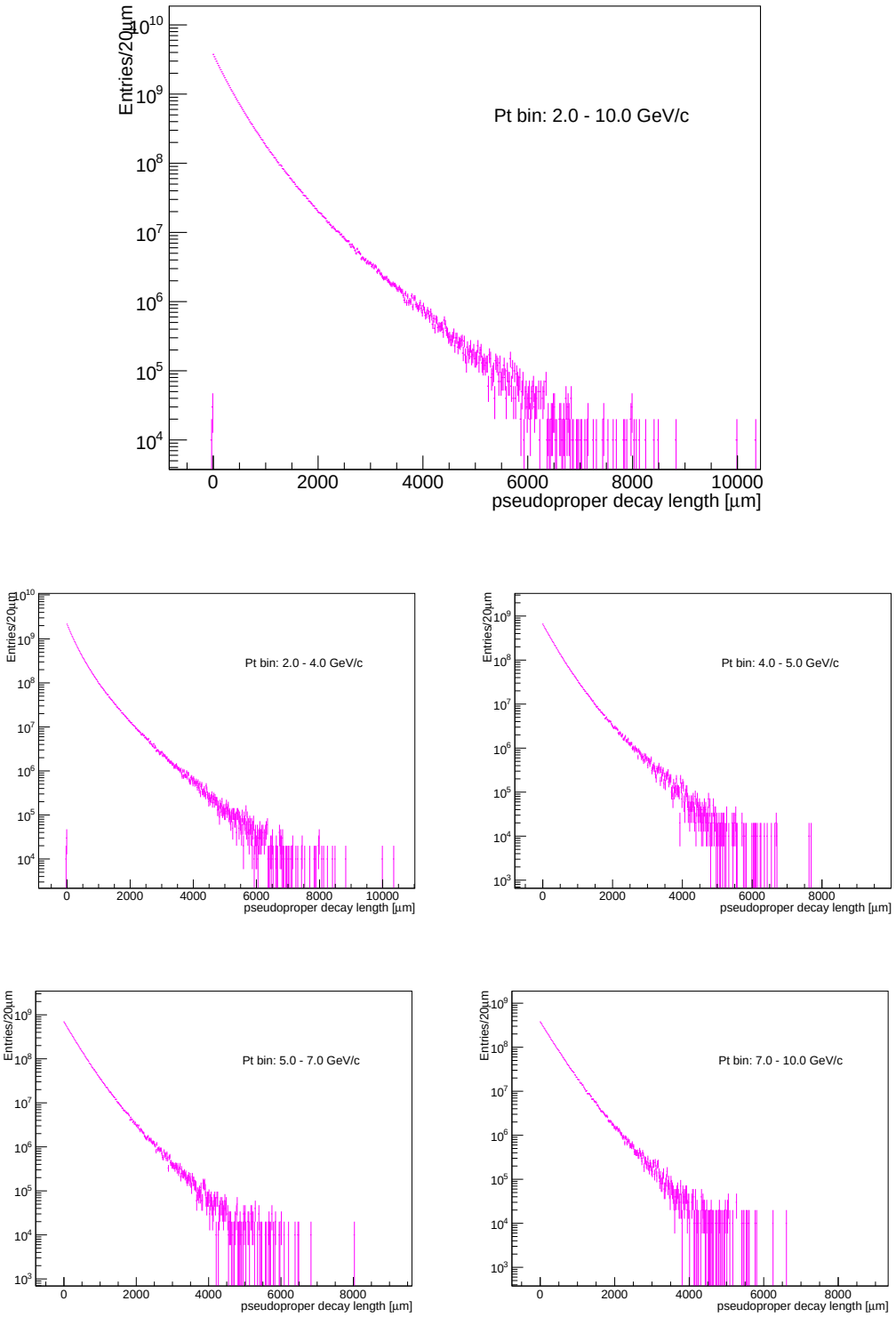

Figure 4.11: Kinematic pseudo-proper decay length distributions $\chi_B(x)$ of secondary J/ψ extracted from the employed MC sample for the integrated case (top) and for the different p_{T} bins (below).

As seen in Eq. 4.14, $F_{\mathrm{B}}(x)$ can be expressed as the convolution of the kinematic x distribution of the J/ψ from b-hadron decays $\chi_B(x)$, which is based on PYTHIA simulations. $\chi_{\mathrm{B}}(x)$ is used as an external template in the likelihood fit, with the resolution function $\mathrm{R}(x)$.

The $\chi_B(x)$ for the p_{T}-integrated case is shown in the top panel of Fig. 4.11. The corresponding p_{T}-differential results are shown in the bottom panels of the same figure. Since the templates are extracted from the simulated MC events without including reconstruction, they are only dependent on kinematic selections and the transverse momentum distribution of the secondary J/ψ. Some templates have entries at negative x values. This comes from low momentum J/ψ that have a large opening angle between their flight direction and the one of the mother b-hadron.

4.6.4 Invariant mass signal $M_{Sig}(m_{\mathrm{e^+e^-}})$

Eq. 4.5 has a $M_{\mathrm{Sig}}(m_{\mathrm{e^+e^-}})$ term that represents the invariant mass distribution of the inclusive J/ψ signal. The term is evaluated through binned fits on J/ψ distributions from MC. The simulations account for various factors such as effects from the detector resolution and radiative decays of J/ψ. The cause for the latter effect are both "internal bremsstrahlung" processes (described in section 4.3) and "external bremsstrahlung" processes arising from radiation from electrons produced inside the detector material.

Now, as these effects give an asymmetry in the form of a tail in the lower invariant masses, a simple symmetric function cannot work. In order to parameterize the signal PDF, a Crystal Ball function is applied:

$$f(m_{\mathrm{e^+e^-}};\alpha,n,\overline{m},\sigma,N) = N\cdot\begin{cases} exp(-\frac{(m_{\mathrm{e^+e^-}}-\overline{m})^2}{2\sigma^2}) & for \quad \frac{m_{\mathrm{e^+e^-}}-\overline{m}}{\sigma} > -\alpha \\ A\cdot(B-\frac{m_{\mathrm{e^+e^-}}-\overline{m}}{\sigma}^{-n} & for \quad \frac{m_{\mathrm{e^+e^-}}-\overline{m}}{\sigma} \leq -\alpha \end{cases}, \tag{4.15}$$

with

$$A = \Big(\frac{n}{|\alpha|}\Big)^n \cdot exp\Big(-\frac{|\alpha|^2}{2}\Big),\ B = \frac{n}{|\alpha|} - |\alpha|\,. \tag{4.16}$$

The Crystal Ball function is a PDF that in general is often used to model various lossy processes in high-energy physics. It is composed by a Gaussian function in the core and a power-law low-end tail. Both the function and its first derivative are continuous.

Invariant mass signal shape parameters from the other signal PDFs are fixed from fits done on MC data. By doing this on each p_{T} interval, one can observe only small variations in the different p_{T} regions. The Gaussian core has a width due to uncertainties in track reconstruction. The results are listed in Fig. 4.12.

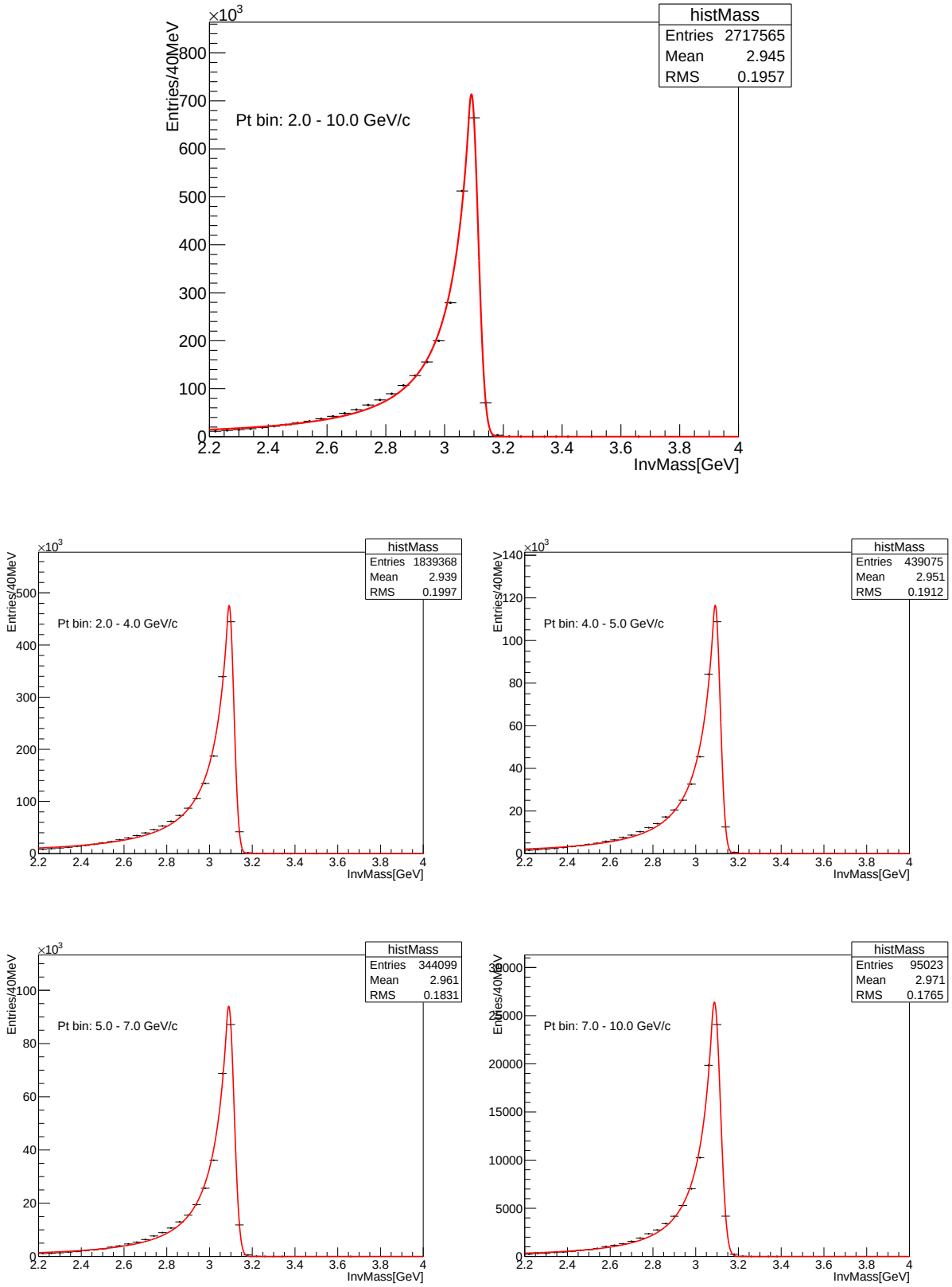

Figure 4.12: Invariant mass distributions of reconstructed J/ψ from MC. It is fitted with a Crystal Ball function. Showing results for the p_{T}-integrated case in the top panel and the corresponding p_{T}-differential results below.

4.6.5 Invariant mass background $M_{Bkg}(m_{e^+e^-})$

In this analysis the shape of the invariant mass signal was found through fits on simulated data. However, it is not the preferred method when looking at the invariant mass background. It would be an extremely difficult approach since one would need knowledge of all the underlying processes that contribute to the background in addition to a great precision when doing so.

Consequently, a data-driven approach is chosen when the invariant mass background PDF is evaluated. The signal shape from section 4.6.4 is fixed and scaled to match with the actual data. The $M_{\mathrm{Bkg}}(m_{e^+e^-})$ shape is then found by doing binned fits on the total (signal and background together) dielectron pair invariant mass distribution in the data. In order to parameterize the PDF, a simple exponential function is applied:

$$M_{Bkg}(m_{e^+e^-};\lambda,A) = A\cdot e^{\frac{m_{e^+e^-}}{\lambda}}. \tag{4.17}$$

In the invariant mass range used in this analysis (2.2 - 4) GeV/c^2, the exponential function fits the background nicely. This is visible in Fig. 4.13 (for the p_{T}-integrated case) and 4.14 (for the different p_{T} bins), which show the results of the fits of the invariant mass distributions of J/ψ candidates from data, used to fix the invariant mass background shape.

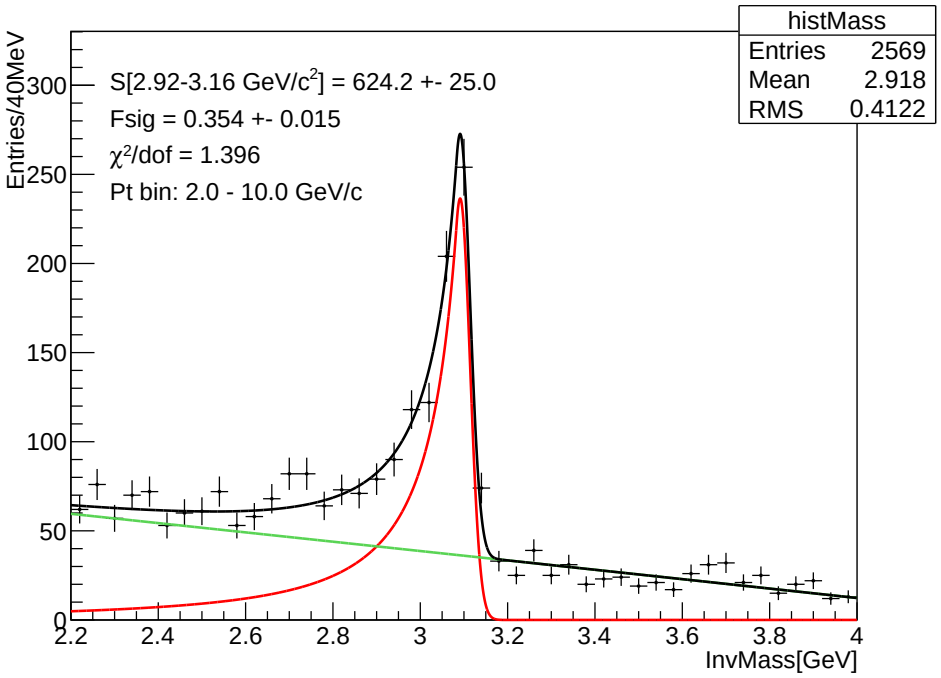

Figure 4.13: Invariant mass distribution with the corresponding fits for the integrated case.

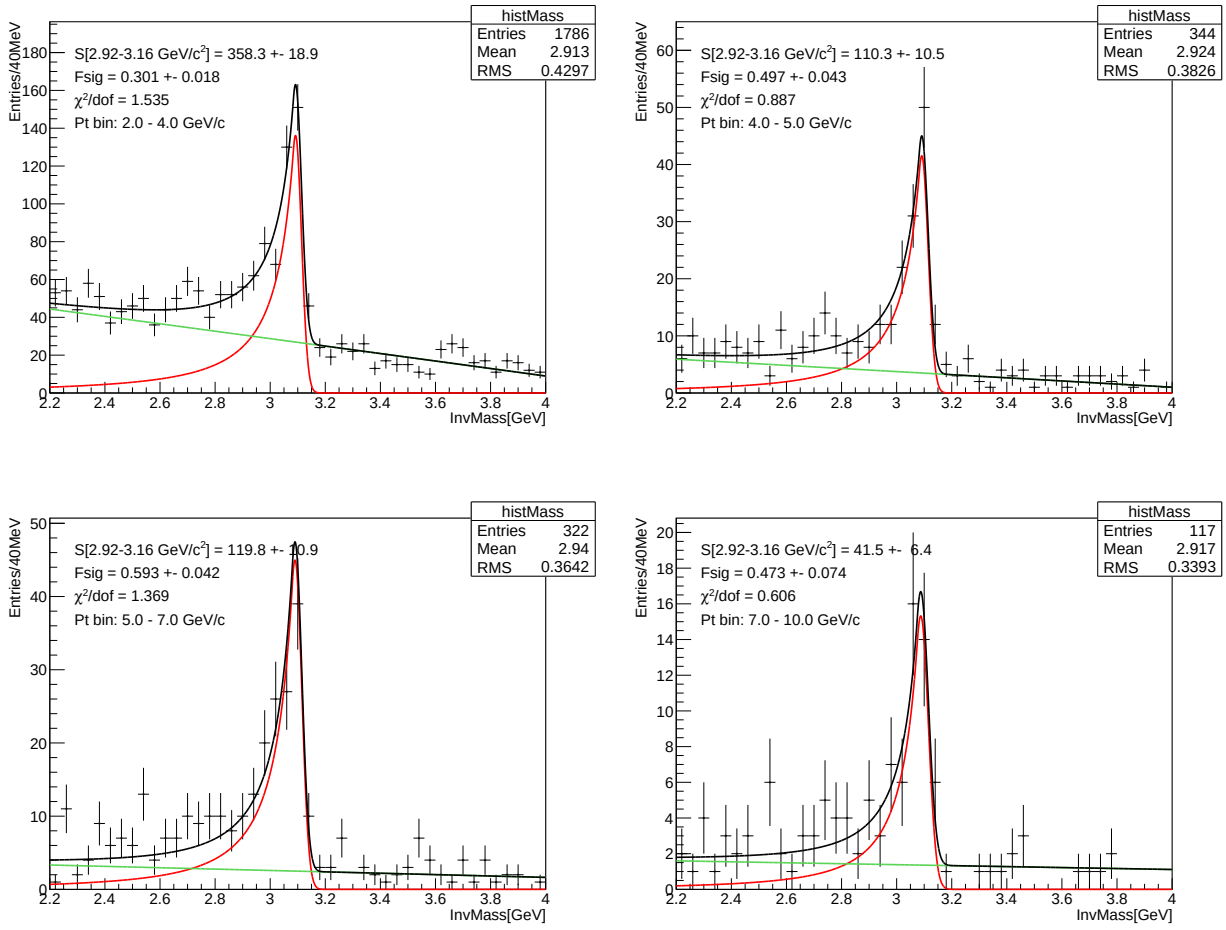

Figure 4.14: Invariant mass distribution with the corresponding fits for the different p_{T} bins.

4.7 Likelihood fit results

The maximum likelihood fits are performed on each chosen p_T interval. All the PDFs of Eq. 4.5 are fixed. The maximum likelihood fit results for the different bins are shown in Fig. 4.16 which represent the projection of the likelihood fit function after the fitting procedure (which is unbinned) both on the pseudo-proper decay length x and the invariant mass $m_{e^+e^-}$ axes. The projection on the pseudo-proper decay length axis is done considering only the candidates in the invariant mass window [2.92,3.16] GeV/c^2, in order to highlight the signal part. The only free parameters in the fits are F_{Sig} and f_B. F_{Sig} is properly rescaled when showing the projection on the x-axis in the signal region.

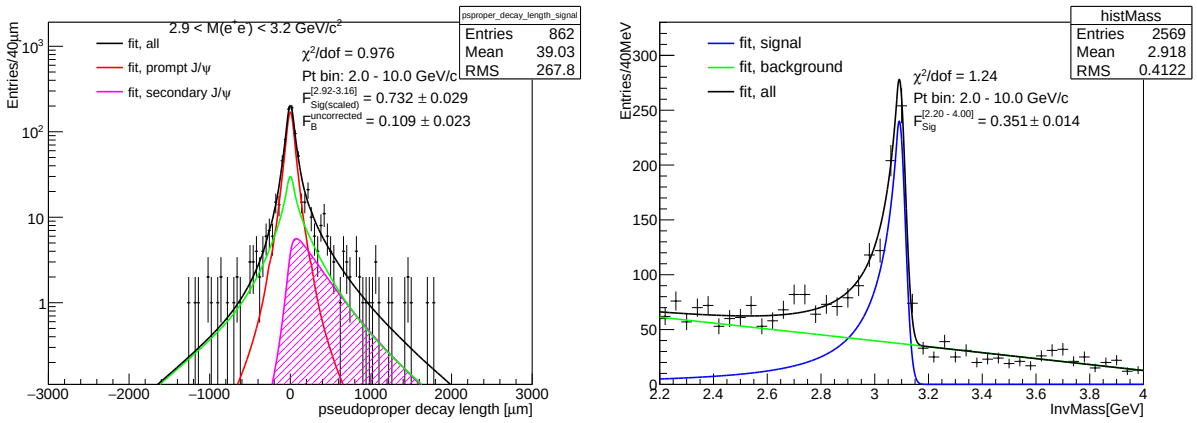

Figure 4.15: Results of the likelihood fit projected on the pseudo-proper decay length in the signal mass region (left) and projected over the invariant mass (right), both for the integrated case [2,10] GeV/c.

The likelihood fit results for the integrated case are shown in Fig. 4.15. Looking at the projection over the pseudo-proper decay length axis (left-hand side), the red line represents the resolution function which describes the prompt J/ψ. The green line is the x-background function and the magenta shaded area (labeled secondary J/ψ) signifies the asymmetry remaining, representing the non-prompt J/ψ from which the fraction f_B originates. On the right side the likelihood fits results are projected over the invariant mass. A χ^2 value is also shown in the histograms, giving an estimation of the quality of the fits. The likelihood fit is also repeated for the different p_T bins, shown in Fig. 4.16.

The results for the different p_T bins are listed in Fig. 4.16. At lower p_T there is better statistics. However, both the resolution and S/B (signal over background ratio) are worse. At higher p_T the statistics are lower, but both F_{Sig} and the resolution on x are better. While also histograms considering the whole invariant mass region are produced, results projected over the signal region shows the asymmetry better while still not omitting any significant signal.

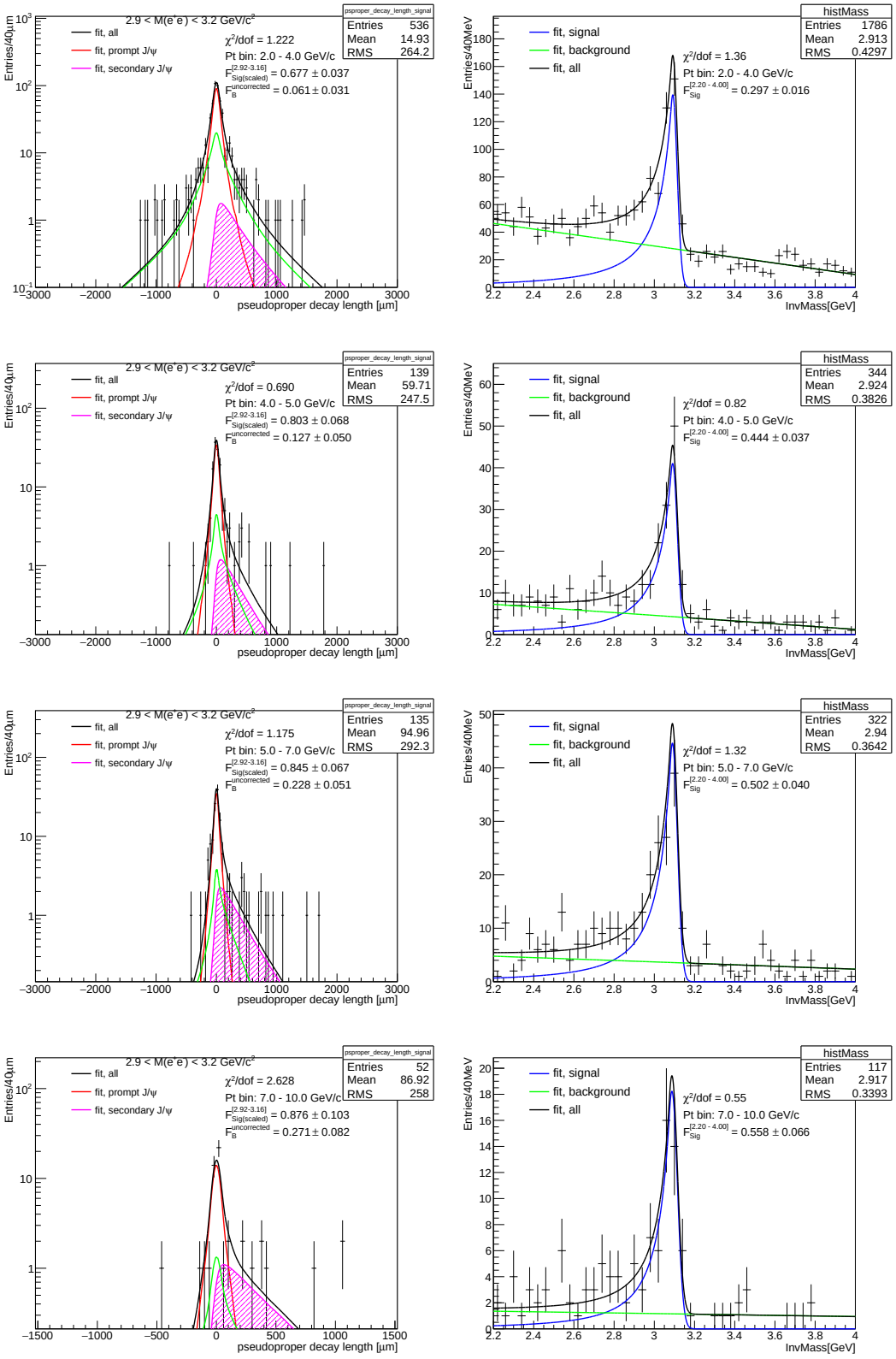

Figure 4.16: All results of the likelihood fit projected on the pseudo-proper decay length in the signal mass region (left) and projected over the invariant mass (right). Showing results for the different p_{T} bins [2,4],[4,5],[5,7] and [7,10] GeV/c.

p_T [GeV/c]	$f'_B \pm \sigma_{stat}$
2-10	0.108 ± 0.023
2-4	0.060 ± 0.031
4-5	0.127 ± 0.050
5-7	0.228 ± 0.051
7-10	0.271 ± 0.081

Table 4.3: A summary of the raw f_{B} for each p_{T} bin with their respective statistical uncertainty.

The raw values of f_{B} (f'_{B}) are shown in table 4.3.

4.8 Correction of the fit results

The values of f_{B} retrieved from the likelihood fit are raw fractions that need to be corrected for differences between non-prompt and prompt J/ψ in acceptance and reconstruction efficiencies. The correction formula is given by Eq. 4.9, discussed in section 4.5.2. The correction factor on f_{B} depends only on the relation in Eq. 4.18:

$$R = \frac{\langle A \times \epsilon \rangle_{\mathrm{B}}}{\langle A \times \epsilon \rangle_{\mathrm{prompt}}}. \tag{4.18}$$

The R-factor is a ratio between the mean acceptance and efficiency factors between non-prompt and prompt J/ψ. This correction factor is computed for each chosen p_{T} interval in addition to the p_{T} integrated case.

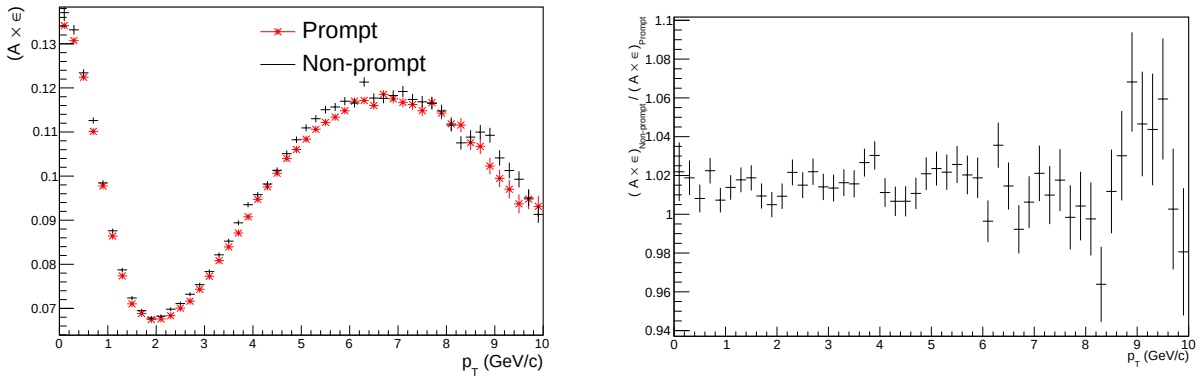

Figure 4.17: p_{T} differential efficiencies for prompt and non-prompt J/ψ (left) and the corresponding ratio (right).

As seen in Fig. 4.17 (left-hand side), the p_{T} differential efficiencies are very similar for prompt and non-prompt J/ψ, a notion that is consolidated by the ratio. The ratio on the right side in

p_T [GeV/c]	R	corrected $f_B \pm \sigma_{stat}$
2-10	1.049	0.103 ± 0.022
2-4	1.021	0.059 ± 0.030
4-5	1.012	0.126 ± 0.049
5-7	1.020	0.224 ± 0.050
7-10	1.004	0.270 ± 0.081

Table 4.4: R-factor and f_B after Acceptance × Efficiency correction.

Fig. 4.17 is in average about 1.02, a 2% difference. However, the p_T distribution is quite different for prompt and non-prompt J/ψ in MC, as seen in Fig. 4.18. This difference has a consequence on the computation on R, as shown in the second column of table 4.4.

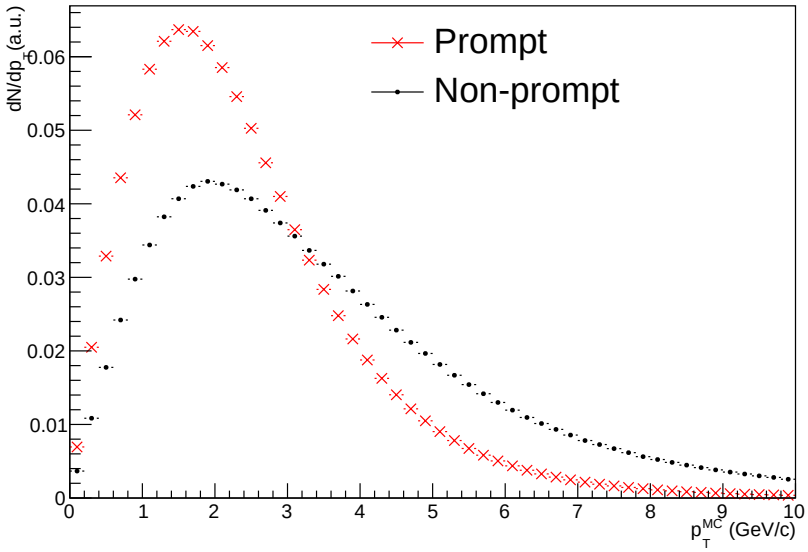

Figure 4.18: The p_T distribution for prompt and non-prompt J/ψ in MC, highlighting the difference between them.

In order to compute the R-factors the average efficiencies are evaluated by weighting the differential efficiency $(A \times \epsilon)(p_T)$ over the kinematic p_T spectrum $(\frac{dN}{dp_T})_{J/\psi}$ of each signal component, according to the formula 4.19:

$$\langle A \times \epsilon \rangle = \frac{\int_{p_T^{min}}^{p_T^{max}} (A \times \epsilon)(p_T) \cdot (\frac{dN}{dp_T})^{5.02TeV}_{J/\psi}}{\int_{p_T^{min}}^{p_T^{max}} (\frac{dN}{dp_T})^{5.02TeV}_{J/\psi}} \tag{4.19}$$

The integrations and differential efficiencies are evaluated separately for each different p_T interval and cut choice in which the analysis is performed.

Table 4.4 lists both the R-factors and corrected f_{B} for the corresponding p_{T} bins. The differences between the raw f_{B}, f'_{B}, and the corrected f_{B} are quite small, in the order of a few percent. Since the p_{T} differential acceptance times efficiency corrections are very similar for prompt and non-prompt, the value of the R factors (and consequently, of the corrections) depends on the difference between the p_{T} shapes between prompt and non-prompt J/ψ. The correction results therefore to be significant only in the p_{T} integrated case, i.e. the widest p_{T} window considered. The MC shapes shown in Fig. 4.18 are not used for this correction. Instead, more realistic p_{T} shapes are applied, which will be discussed in chapter 5.

Chapter 5

Systematic uncertainties

All the different PDFs of Eq. 4.5 are fixed using reasonable assumptions when doing the unbinned maximum likelihood fit. However, the fixed PDFs may not be fully accurate and a series of systematic uncertainties has to be calculated specifically for each different PDF. Furthermore, also a systematic uncertainty on the acceptance and efficiency correction computed on MC (Eq. 4.7) has to be applied. In this chapter all systematic uncertainties on the computation of f_{B}, both for p_{T}-differential and p_{T}-integrated cases, will be discussed.

5.1 Systematic uncertainty on the resolution function

The resolution function is determined from the pseudo-proper decay length distributions of prompt J/ψ from MC simulations after applying the impact parameter tuning procedure described in section 4.3. In order to determine the systematic uncertainty on f_{B} due to potential misevaluation of the resolution function $R(x)$, the likelihood fits are repeated using an artificially modified $R(x)$, according to the formula:

$$R'(x) = \frac{1}{1+\delta} R\Big(\frac{x}{1+\delta}\Big), \tag{5.1}$$

with x being the pseudo-proper decay length and δ representing the relative variation of the variance in the function. The multiplicative factor $\frac{1}{1+\delta}$ ensures that the PDF is properly normalized to one. From section 4.6.1, the residual discrepancy between data and MC regarding the impact parameter resolution of single leg, after the tuning procedure, is about 3% at high p_{T}, so we could assume the same discrepancy also at the level of the resolution function for the x.

In order to compute the systematic uncertainty, the relative variation of the variance δ is set

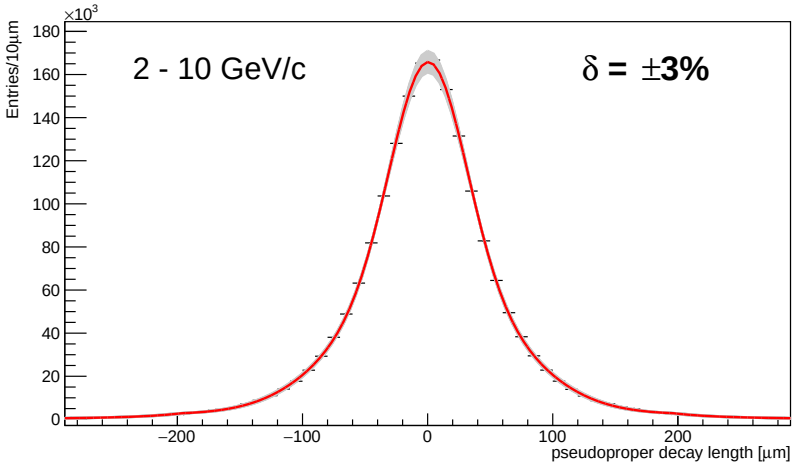

Figure 5.1: Variation of the resolution function R(x) for the p_{T} range [2,10] GeV/c, obtained after varying the δ parameter in Eq. 5.1 from -3% to +3%.

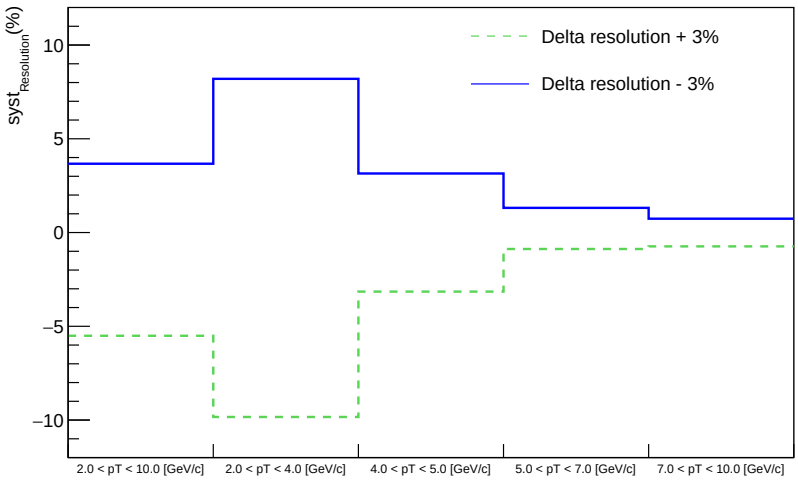

Figure 5.2: The relative deviation for each p_{T} bin corresponding to δ +3% and -3% (see text for details).

to +3% and -3% and the modified resolution function is replaced in the likelihood fit. Fig. 5.1 shows $R(x)$ for the p_{T}-integrated case (red line) with the corresponding variations according to Eq. 5.1 with $-3 < \delta < 3$ (gray band). In Fig. 5.2 the relative variations obtained on f_{B} after changing the resolution function are shown for the two extreme cases ($\delta = \pm 3\%$) as a function of p_{T}. In Fig. 5.3 the final assigned systematic uncertainty is shown, which is obtained by taking the average of the absolute variations shown on the left. The systematic uncertainty on the resolution function is higher at low p_{T} where the resolution on the x rapidly deteriorates (see Fig. 4.7 and 4.8 in section 4.6.1).

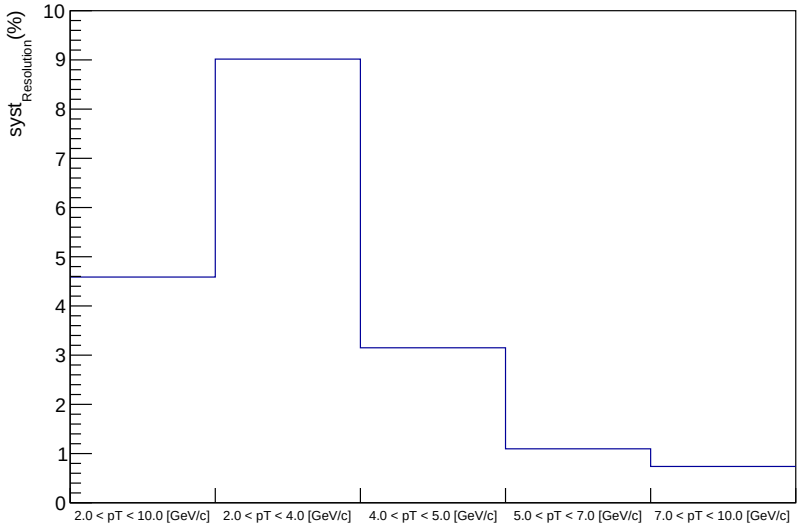

Figure 5.3: The assigned systematic uncertainty for the resolution function, obtained by taking the average of the absolute variations shown in Fig. 5.2.

5.2 Systematic uncertainty on the x background

As discussed in section 4.6.2, the pseudo-proper decay length background PDF is evaluated from the fit of the x distributions of J/ψ candidates extracted from the invariant mass sidebands. These invariant mass windows ([2.2,2.6] and [3.2,4] GeV/c^2) are adjacent to the invariant mass region where most of the signal candidates reside.

In order to calculate the systematic for this PDF the parameters of $F_{\rm Bkg}(x)$, Eq. 4.13, are changed within the uncertainties obtained from the fitting procedure. In order to estimate the systematic uncertainty, three parameters have been changed, namely λ_+, λ_- and $\lambda_{\rm sym}$, which represent positive, negative, and symmetric exponential slopes of the background function. These three parameters are correlated, so they cannot be changed independently within one σ. In order to account for the proper correlations, contour plots are used. The contour plots for (λ_+, λ_-)), $(\lambda_{\rm sym}, \lambda_-)$) and $(\lambda_{\rm sym}, \lambda_+)$), are shown in Fig. 5.4[1].

The likelihood fits are then repeated after changing artificially fitting parameters, two at a time. The third is kept at its original value. With sixty 2D-Gaussian distributed points inside the contours (plotted in Fig. 5.4), the total amount of likelihood fits performed for each $p_{\rm T}$ bin amounts to 180. It was verified that the obtained $f_{\rm B}$ values have a Gaussian distribution, which is centered

[1] In principle, the 3D contour should be used to account for the correlations among all three parameters simultaneously. With the current procedure the systematic uncertainty might be overestimated. This will be updated for the final publication.

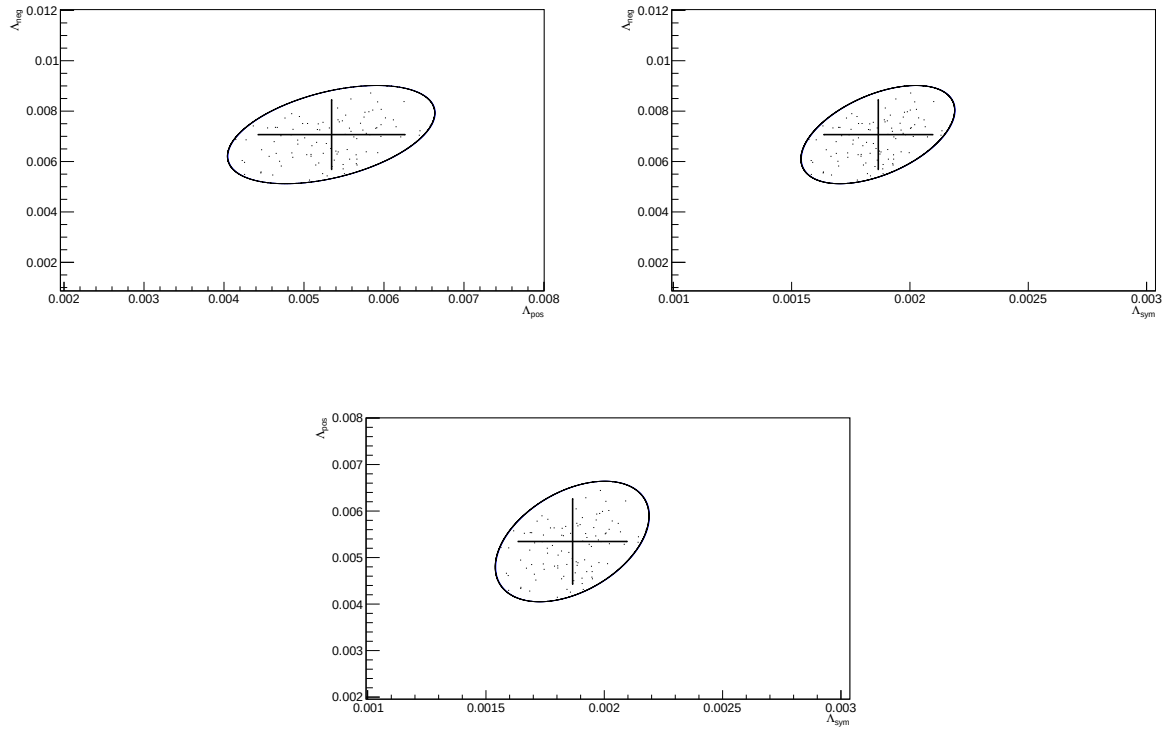

Figure 5.4: Contour plots describing the correlation between λ_+ and λ_- (top left), λ_{sym} and λ_- (top right), λ_{sym} and λ_+ (bottom). Each plot contains also the 60 gaussian distributed points used to assign the systematic uncertainty. The data points superimposed represent the values and the corresponding uncertainties of the parameters obtained from the fit of $F_{Bkg}(x)$ (see text for details).

around the central $f_{\rm B}$ value estimated from the fit. The RMS of such distribution gives the basis for the estimate of the systematic uncertainty due to the $F_{\rm Bkg}(x)$ component, which is shown in Fig. 5.5 in different $p_{\rm T}$ bins. As expected it increases at low $p_{\rm T}$, where the signal to background ratio becomes lower.

5.3 Systematic uncertainty on the non-prompt J/ψ x template

The resolution function is convoluted with the kinematic template $\chi_{\rm B}(x)$ to evaluate the pseudo-proper decay length PDF of non-prompt J/ψ. The $\chi_{\rm B}(x)$ used to determine the central value of $f_{\rm B}$ is taken from MC-truth x distributions of non-prompt J/ψ from MC simulations, as described in Section 4.6.3. The shape of $\chi_{\rm B}(x)$ template depends mainly on the b-hadron $p_{\rm T}$ distributions and, at second order, on the decay kinematic as implemented in MC simulations.

In order to compute the systematic uncertainty on the $F_{\rm B}(x)$ PDF, the likelihood fits are repeated

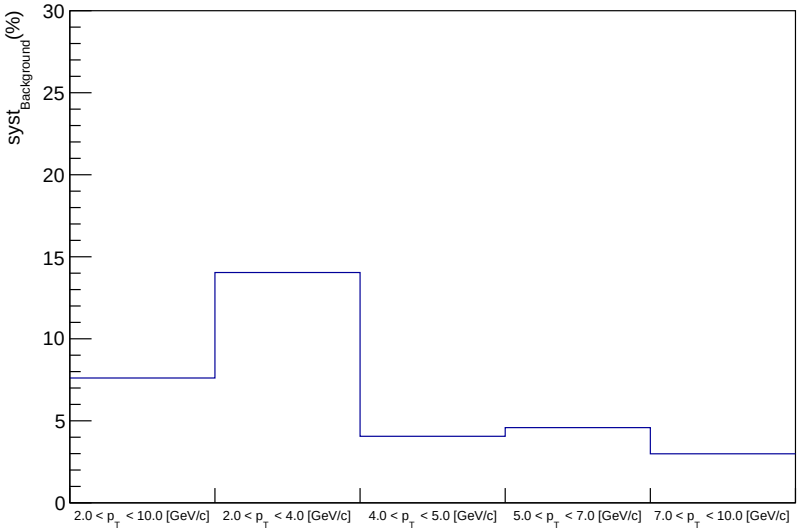

Figure 5.5: Systematic uncertainty assigned on $F_{\mathrm{Bkg}}(x)$ for different p_{T} bins.

with a different $\chi_{\mathrm{B}}(x)$ distribution, which is obtained by re-weighting the p_{T} distribution from MC in order to obtain a p_{T} shape compatible with the spectra predicted by FONLL [29, 30] at $\sqrt{s}$ = 5.02 TeV. The difference between the two p_{T} shapes will be discussed in detail in section 5.6. In the top panel of Fig. 5.6 non-prompt J/ψ x templates from MC before and after the re-weighting are superimposed. A more quantitative comparison is shown by the ratio plotted in the bottom panel of the same figure. The difference observed between the two templates is within ~5% over a wide x range.

The systematic uncertainties on f_{B} is found well below 1% for all p_{T} bins. The small value of this systematic uncertainty, which is indeed negligible compared to other sources, reflects the small difference observed at the level of x templates discussed above.

5.4 Systematic uncertainty on invariant mass signal

The PDF of the invariant mass signal, described by a Crystal-Ball function, is fixed from MC simulations. The MC takes into account detector resolution effects and radiative decays generated by the EvtGen+PHOTOS package. The uncertainty in the signal shape lies in how well these processes are simulated, in particular the reproduction of the electron interactions in the ALICE detector material.

The method of calculating uncertainty is conceptually equivalent to the one used for the resolution function on x. The likelihood fit is repeated with an artificially modified fraction of signal

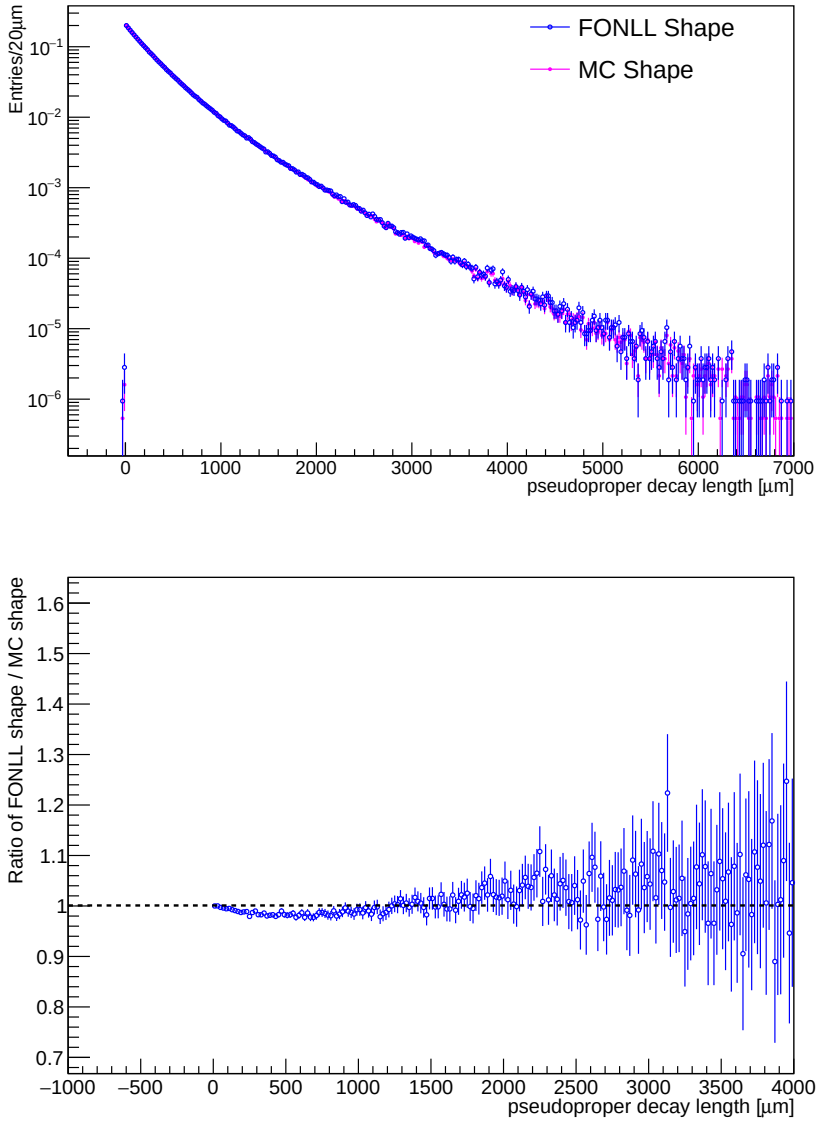

Figure 5.6: Non-prompt J/ψ x templates from PYTHIA and FONLL superimposed (top) and their ratio (bottom).

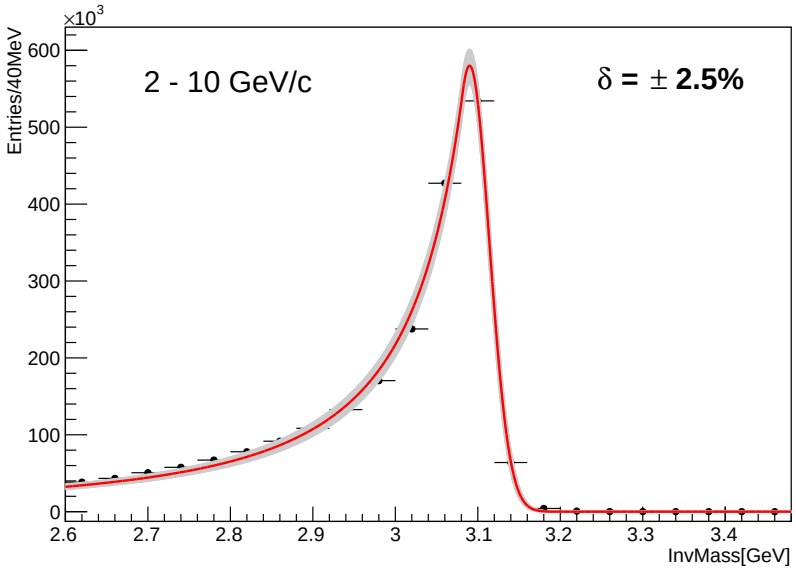

Figure 5.7: Example of variation of the $M_{\mathrm{Sig}}(m_{\mathrm{e^+e^-}})$ function in the p_{T} range [2,10] GeV/c. It is obtained after changing the relative fraction $\Delta f_{\mathrm{Sig}}/f_{\mathrm{Sig}}$ of signal within the mass peak region [2.92, 3.16] GeV/c^2 within ±2.5%.

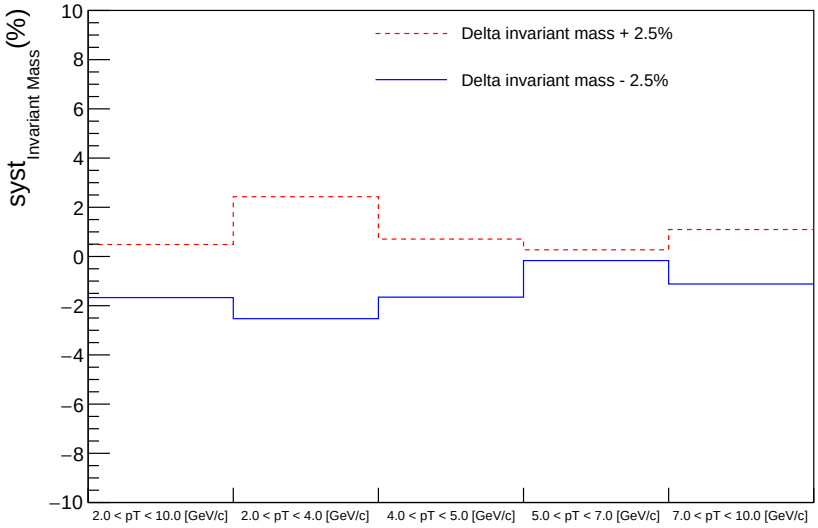

Figure 5.8: The systematic uncertainty on f_{B} for each p_{T} bin corresponding to δ +2.5% and -2.5% (see text for details).

within the invariant mass window 2.92-3.16 GeV/c^2 ("signal" region). In this analysis the varying factor is set to ±2.5% according to what was estimated in the inclusive J/ψ analysis in pp collisions at $\sqrt{s}$ = 5 TeV [20]. Fig. 5.7 shows the variations of the signal shape (red function) obtained

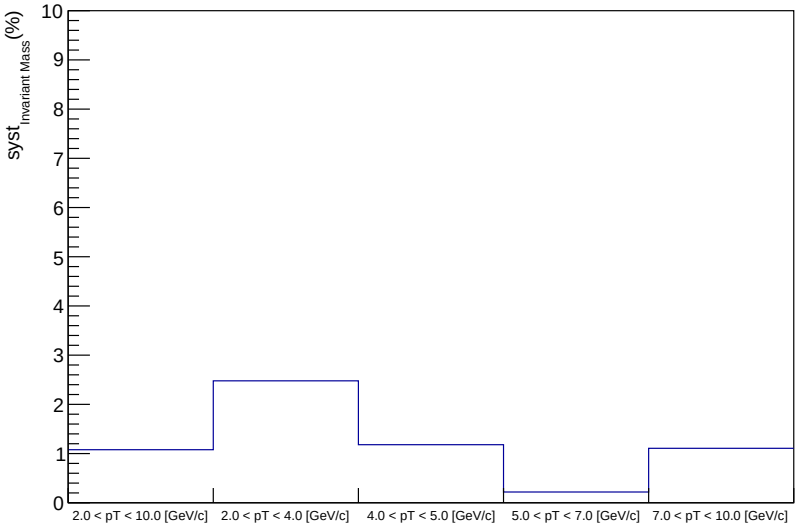

Figure 5.9: The systematic uncertainty on f_{B} for each p_{T} bin, obtained from the average of Fig.5.8

for the p_{T}-integrated case by changing $\Delta f_{\mathrm{Sig}}/f_{\mathrm{Sig}}$ in 2.92-3.16 GeV/c^2 between -2.5% and +2.5%.

In Fig. 5.9 the relative variations obtained for f_{B}, for each of the two extreme cases, are shown. The assigned systematic uncertainty, which is taken as the average of the two extreme absolute variations, is plotted in Fig. 5.9.

5.5 Systematic uncertainty on invariant mass background

As discussed in section 4.6.5, in order to fix the invariant mass background shape, the invariant mass distribution m_{ee} from data is fitted by a function which is the sum of signal (Crystal-Ball) and background (exponential) functions. The signal shape is fixed from MC simulations therefore from the fits on data the parameters of the invariant mass background function are determined.

In order to estimate the uncertainty related to the background shape like-signed (LS) pairs were considered. When a J/ψ decays, it always produces a dilepton pair of opposite sign (OS) daughters, an electron and a positron. However, when looking at LS pairs, we search for a pair of two electrons or two positrons.

A comparison between OS and LS invariant mass distributions for the p_{T}-integrated case is shown in Fig. 5.10. The LS distribution is scaled in order to match the integral of the OS in the invariant mass region 3.2-4 GeV/c^2 (the scaling factor is indicated in the figure and amounts

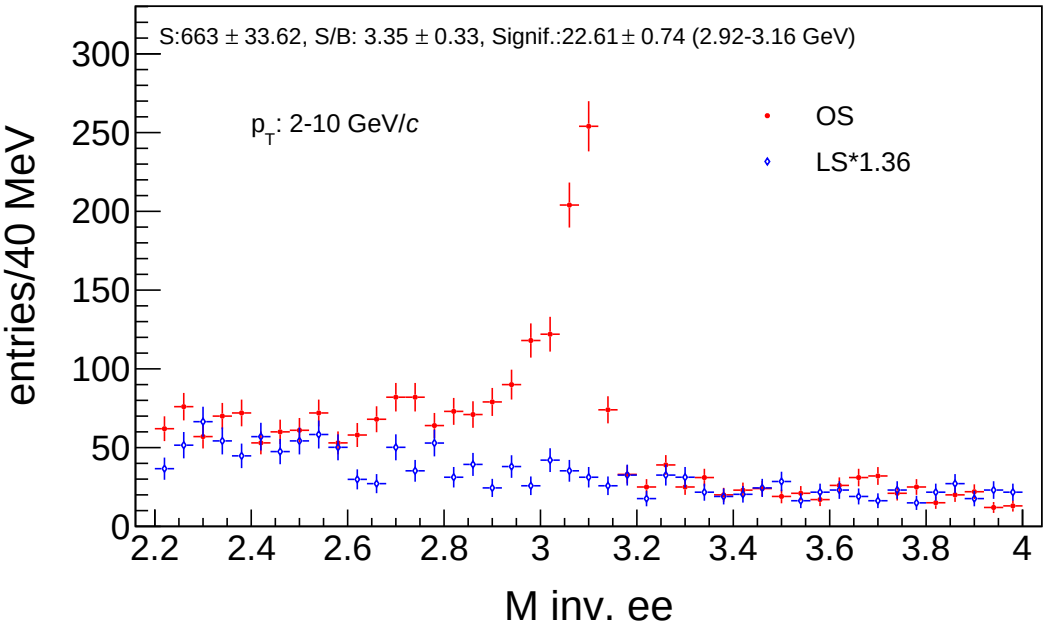

Figure 5.10: Comparison between the invariant mass distributions of OS (red) and LS pairs (blue).

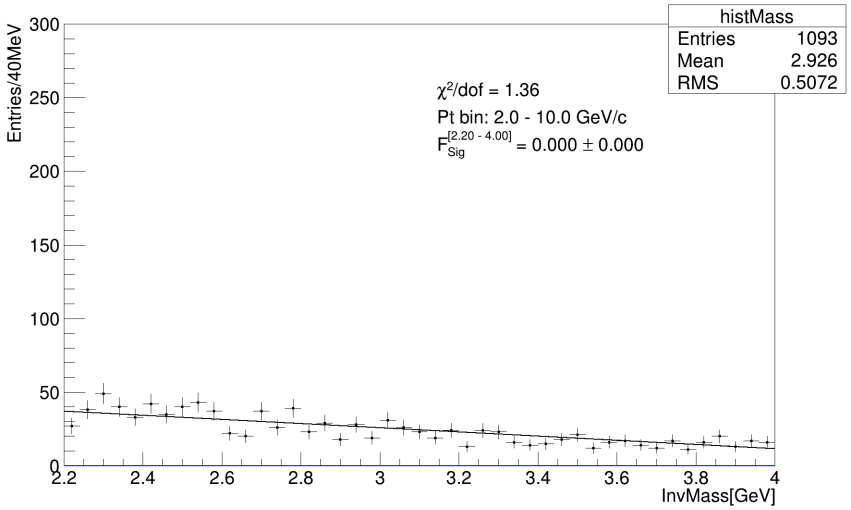

Figure 5.11: Invariant mass distribution for LS pairs fitted by an exponential for the p_{T} integrated case.

to about 1.4). In order to estimate the systematic uncertainty on f_{B} the original invariant mass background PDF, based on the fit of OS pairs, is replaced in the likelihood fit by the PDF determined from fitting LS pairs. The scaling factor mentioned above is indeed not relevant for this

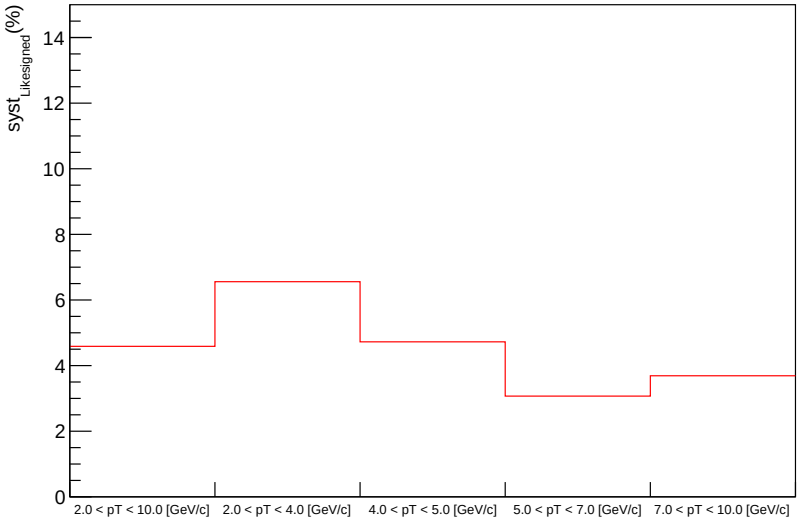

Figure 5.12: Systematic uncertainty assigned for the invariant mass background function in different p_T bins.

analysis since only its shape is used in the likelihood fit. The fit of the LS distribution is done using an exponential function, as in the default case. An example of this fit is shown for the p_T-integrated case in Fig. 5.11. The relative difference obtained on the corresponding f_B values, shown in Fig. 5.12, is taken as systematic uncertainty.

5.6 Systematic uncertainty on p_T shapes of prompt and non-prompt J/ψ

The un-binned maximum likelihood fit procedure, discussed in section 4.7, produces raw values of f_B. These values are corrected as shown in section 4.8 to account for differences for the acceptance times efficiency correction between prompt and non-prompt J/ψ. The factors used to correct depend on the average $< A \times \epsilon >$ in each p_T bin. Assuming no polarization, the p_T-differential efficiencies for prompt and non-prompt J/ψ are very similar (see Fig. 4.17). However, different p_T distributions for prompt and non-prompt J/ψ makes the average $< A \times \epsilon >$ different over a finite-sized p_T range. The difference between the uncorrected and corrected f_B is small, but a systematic is included to take into account the non-perfect knowledge of p_T shapes for both prompt and non-prompt J/ψ.

Figure 5.13 shows the different alternatives considered to estimate the systematic uncertainty for non-prompt and prompt J/ψ (left and right-hand side respectively). In particular for the

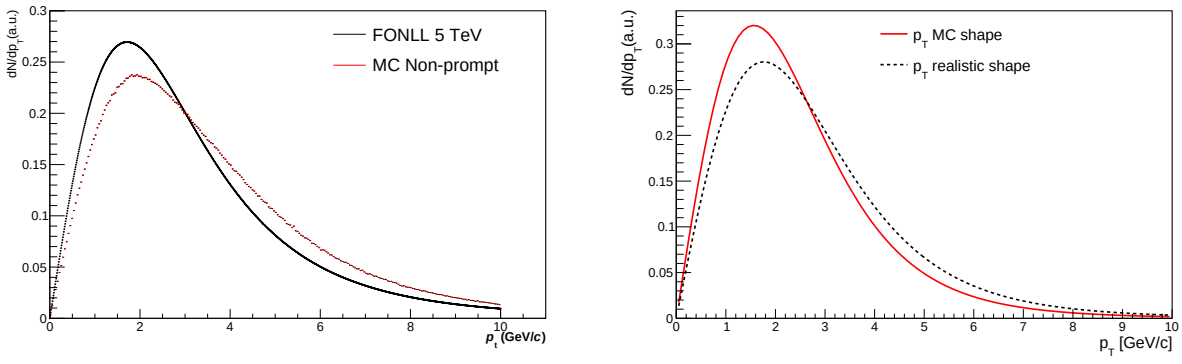

Figure 5.13: Left: comparison between p_{T} spectra for non-prompt J/ψ according to PYTHIA (red points) and FONLL (black, continuous line). Right: comparison between the prompt J/ψ spectra from MC and the more realistic shape (see text for details).

non-prompt J/ψ the MC p_{T} shape, based on PYTHIA, is replaced by a p_{T} shape computed according to FONLL model, considering $\sqrt{s} = 5$ TeV. Regarding the prompt J/$\psi$the p_{T} shape in the MC is based on the "universal" fitting function described by equation 5.2[27]:

$$\frac{\langle p_{\mathrm{T}} \rangle}{d\sigma/dy} \cdot \frac{d^2\sigma}{dy dp_{\mathrm{T}}} = \frac{2(n-1) \cdot B^2 \cdot p_{\mathrm{T}}/\langle p_{\mathrm{T}} \rangle}{(1 + B^2 \cdot (p_{\mathrm{T}}/\langle p_{\mathrm{T}} \rangle)^2)^n}, \tag{5.2}$$

where n is a free parameter, $\langle p_{\mathrm{T}} \rangle$ and $d\sigma/dy$ are the values of measured average p_{T} and cross-sections, and B is defined as:

$$B = \Gamma(3/2)\Gamma(n-3/2)/\Gamma(n-1)\,. \tag{5.3}$$

In Eq. 5.3, Γ is the gamma function. In the case of this approach, all the available experimental data ($d^2\sigma/dydp_T, \langle p_{\mathrm{T}} \rangle$) for inclusive J/$\psi$ production in pp collisions with a p_{T} reach down to zero are collected. The p_{T}-differential cross-sections are normalized to unity and then the transformation of $p_{\mathrm{T}} \rightarrow \langle p_{\mathrm{T}} \rangle / p_{\mathrm{T}}$ is done to obtain a universal scaling.

This model is used to extrapolate the inclusive J/ψ cross-section at a specific center-of-mass energy. However, the p_{T} shape in the MC is not realistic since it was obtained by fitting only forward rapidity results available in reference [27]. Therefore the default prompt J/ψ p_{T} shape from MC (red function in the left-hand side of Fig. 5.13) is substituted by a more realistic shape (black function), obtained by fitting the p_{T} spectra of inclusive J/ψ measured in pp collisions at $\sqrt{s} = 5$ TeV [20], i.e. based on the same data sample used for this analysis.

Therefore in total there are four different possible combinations to compute average efficiency, namely:

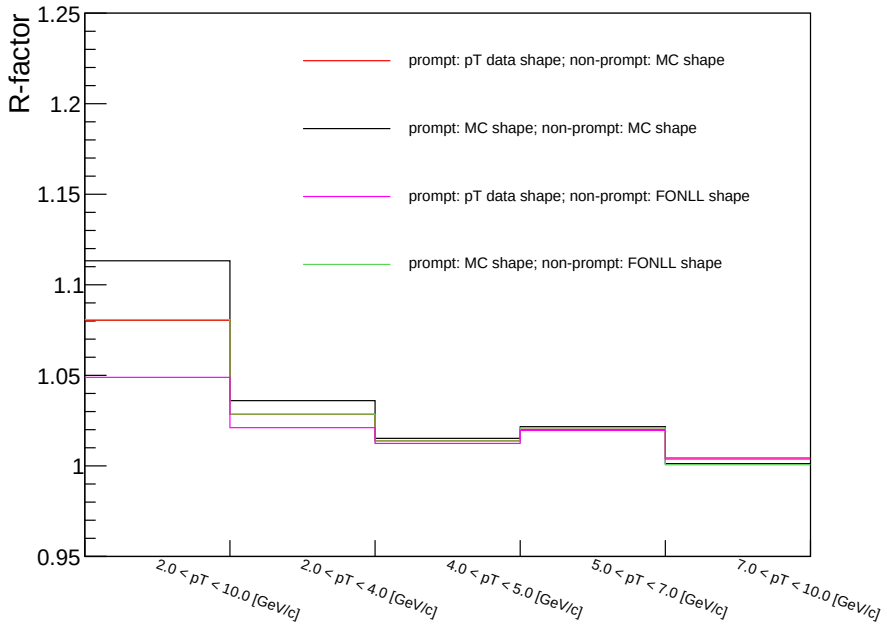

Figure 5.14: R-factors as a function of p_T for the the different combinations of prompt and non-prompt J/ψ spectra. The red line shows the R-factors for a p_T "realistic" shape for prompt J/ψ combined with the default MC shape for non-prompt J/ψ. The black line is for MC-generated shapes for both types. The magenta use p_T data shape for prompt and FONLL for non-prompt, while the green use MC shape for prompt and FONLL shape for non-prompt J/ψ.

1. realistic p_T shape for prompt J/ψ and MC p_T shape for non-prompt J/ψ.
2. MC p_T shape for both prompt and non-prompt J/ψ.
3. p_T realistic shape for prompt J/ψ and FONLL p_T shape for non-prompt J/ψ.
4. MC p_T shape for prompt J/ψ and FONLL p_T shape for non-prompt J/ψ.

The R-factor, computed by Eq. 4.18 in section 4.8, represents the ratio between average efficiencies of non-prompt and prompt J/ψ. The R-factors in different p_T bins are plotted in Fig. 5.14 for all possible combinations discussed above. As expected the correction is higher in the p_T-integrated case due to the wider p_T range.

The combination number (3), plotted in magenta in Fig. 5.14, is the one chosen as central value for the acceptance and efficiency correction of f_B. The choice relies on the consideration that the FONLL represents the most updated model employed to describe open heavy-flavor hadron production (including non-prompt J/ψ). Furthermore, the p_T shape used for prompt J/ψ represents a more realistic approximation than the generated MC shape, since it is computed on the same data sample used for this analysis. The remaining three combinations are used for

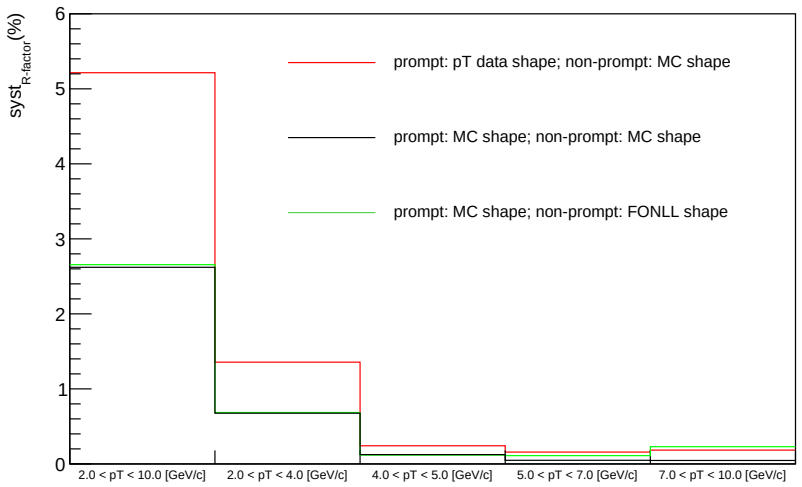

Figure 5.15: Relative deviation observed for the remaining three combinations used to determine the systematic uncertainty (see text for details). The maximum deviation (red line) is used to assign the final systematic uncertainty.

the evaluation of the systematic uncertainty on the correction factor. The relative deviation obtained for each of the remaining combinations is shown in Fig. 5.15. The systematic uncertainty is obtained by taking the maximum deviation, which is represented by the red line in the same figure. This corresponds to the case when the realistic p_{T} shape and PYTHIA MC are used for prompt and non-prompt J/ψ respectively. As expected the systematic uncertainty is higher in the p_{T}-integrated case and it amounts to about 5%, instead it is of the order of 1% or below in all narrower p_{T} bins.

5.7 Summary of systematic uncertainty

The overall systematic uncertainty is obtained by summing in quadrature all components discussed in this chapter.

An overview of all systematic contributions, as well as their quadratic sum, is provided in table 5.1. A graphical representation of all contributions is also provided in Fig. 5.16. The main contributions to the overall systematic uncertainty come from x background shape ($F_{\mathrm{Bkg}}(x)$) and resolution function $R(x)$, in particular in the low p_{T} region. All other contributions are in most of the cases below 5%, being almost negligible in the total systematic calculation. These observations, as well as the p_{T} dependence found for the systematic uncertainties, are in line with previous published ALICE measurements [14].

Systematic Unc. (%)	$p_T > 2$ GeV/c	[2-4] GeV/c	[4-5] GeV/c	[5-7] GeV/c	[7-10] GeV/c
R(x)	4.6	9.0	3.2	1.1	0.7
$F_{\mathrm{Bkg}}(x)$	7.6	14.0	4.1	4.6	3.0
$F_{\mathrm{B}}(x)$	0.2	< 0.1	0.1	0.1	0.1
M_{Sig}	1.1	2.5	1.2	0.2	0.2
M_{Bkg}	4.6	6.6	4.7	3.1	3.1
MC p_T spectra	2.6	0.7	0.1	< 0.1	< 0.1
Total	10.1	18.1	7.1	5.6	4.4

Table 5.1: Final values of the systematic uncertainties on f_{B} expressed in percentiles, for all p_T bins considered in this analysis.

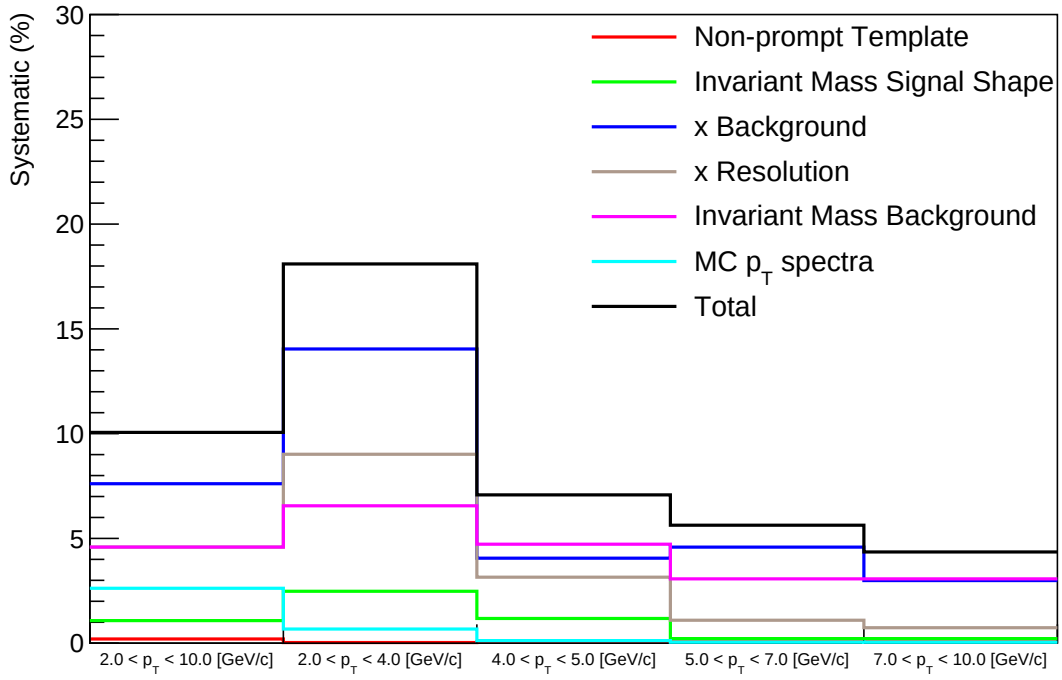

Figure 5.16: Summary of the systematic uncertainty studies in this analysis. The black line represents the total systematic uncertainty and corresponds to the sum in quadrature of the single components in the figure. Some smoothing in the higher p_T bins have been applied on some components.

Chapter 6

Results and Outlook

In this chapter the results obtained from the analysis described in this thesis will be discussed. In particular the fraction of non-prompt J/ψ as a function of p_{T} will be presented and compared with similar mid-rapidity measurements from other experiments, also considering several center-of-mass energies. In addition prompt and non-prompt J/ψ cross-sections, obtained by combining results of inclusive J/ψ cross-sections and f_{B}, will be presented. The comparison with QCD theoretical models describing the production of both prompt charmonia and open-heavy flavour, will be also discussed.

6.1 Non-prompt J/ψ fraction as a function of p_{T}

A summary of non-prompt J/ψ fractions as a function of p_{T} and for the p_{T}-integrated cases are shown in table 6.1, along with the absolute statistical and systematic uncertainties. It is clear from the table that for all p_{T} bins the overall uncertainty is dominated by the statistical uncertainty.

p_T [GeV/c]	$f_{\mathrm{B}} \pm \sigma_{\mathrm{stat}} \pm \sigma_{\mathrm{syst}}$
2-10	$0.103 \pm 0.022 \pm 0.011$
2-4	$0.059 \pm 0.030 \pm 0.011$
4-5	$0.126 \pm 0.049 \pm 0.009$
5-7	$0.224 \pm 0.050 \pm 0.013$
7-10	$0.270 \pm 0.081 \pm 0.012$

Table 6.1: Final f_{B} values for each p_{T} interval considered in this analysis with both statistical and systematic uncertainties.

In Fig. 6.1 and 6.2 the non-prompt J/ψ fractions obtained from this analysis are compared to similar measurements performed at mid-rapidity by other experiments. The error bars in both

figures, and for all experimental results, represent the total uncertainty, meaning the sum in quadrature of the systematic and statistical uncertainties.

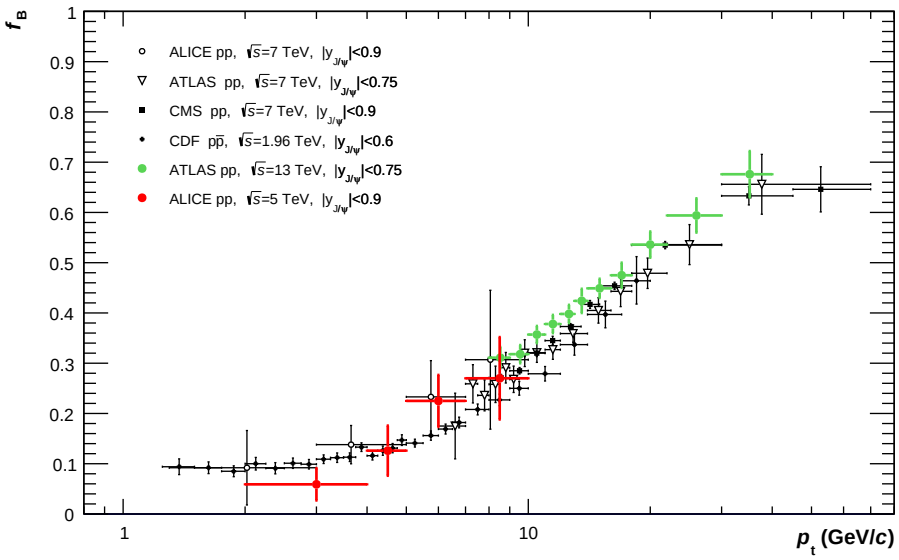

Figure 6.1: Non-prompt J/ψ fraction as a funtion of p_{T} from this analysis compared with results in pp collisions from other experiments at mid-rapidity, namely: ATLAS, both $\sqrt{s}$ = 7 TeV [11] and $\sqrt{s}$ = 13 TeV [35], CMS [31] and ALICE [14] at $\sqrt{s}$ = 7 TeV. The comparison with CDF [23] (p$\bar{\mathrm{p}}$ at $\sqrt{s}$ = 1.96 TeV) is also shown.

In Fig. 6.1 the comparison is done with other measurements available in pp collisions at different center-of-mass energies. In particular there are results from ALICE [14], ATLAS [11] and CMS [31] at $\sqrt{s}$ = 7 TeV and recent ATLAS [35] measurements at $\sqrt{s}$ = 13 TeV. In addition there are the lower energy results from CDF [23] in $p\bar{p}$ collisions at $\sqrt{s}$ = 1.96 TeV. The non-prompt J/ψ fraction exhibits a very similar trend despite the different center-of-mass energy. However, a small energy dependence is visible from Fig. 6.1, in particular the non-prompt J/ψ fraction seems to increase slightly with $\sqrt{s}$. This is visible for example by comparing ATLAS measurements at $\sqrt{s}$ = 13 and 7 TeV for p_{T} > 6.5 GeV/c, and could be related to a different dependence of the charm and beauty production cross-sections as a function of $\sqrt{s}$. The results obtained from this analysis look in line with previous results and the overall uncertainty is smaller compared to previous ALICE measurements at $\sqrt{s}$ = 7 TeV. However, due to the present uncertainties it is not possible to conclude about any energy dependence in the low p_{T} region.

In Fig. 6.2 a comparison with other recent mid-rapidity measurements in pp at $\sqrt{s}$ = 5 TeV from ATLAS [10] and CMS [55] is shown. The results from this analysis at high p_{T} match those from both CMS and ATLAS within the uncertainties. This comparison shows clearly that the ALICE measurements have a unique kinematic coverage at the LHC, and nicely complement the other

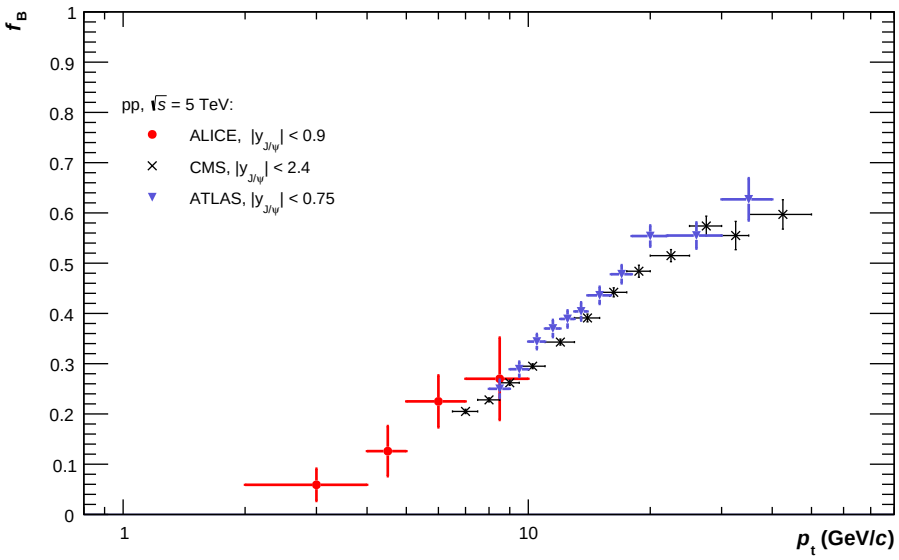

Figure 6.2: Non-prompt J/ψ fraction as a funtion of p_T from this analysis compared with mid-rapidity measurements in pp collisions from CMS [55] and ATLAS [10] at $\sqrt{s} = 5$ TeV.

measurements at mid-rapidity, which are available only for $p_T > 6.5$ GeV/c.

6.2 Prompt J/ψ cross-sections

The prompt J/ψ cross-section integrated over p_T can be obtained by combining the measurement of the inclusive J/ψ cross-section ($\sigma_{J/\psi}$) [20] and the f_B value, both measured for $2 < p_T < 10$ GeV/c, according to the following formula [1]:

$$\sigma^{\text{prompt}}_{J/\psi} = (1 - f_B) \cdot \sigma_{J/\psi} \,. \tag{6.1}$$

In order to calculate both statistical and systematic uncertainties on the prompt J/ψ cross-section, the uncertainties on f_B and $\sigma_{J/\psi}$ are added in quadrature assuming that the two quantities are not correlated. In the measured region the integrated cross-section is:

$$\sigma_{\text{prompt}J/\psi}(|y| < 0.9, 2 < p_T < 10 \text{ GeV}/c) = 5.09 \pm 0.69 \text{ (stat.)} \pm 0.49 \text{ (syst.)} \; \mu\text{b} \,.$$

The double differential cross-section $\frac{d^2\sigma_{J/\psi}}{dp_T dy}$ for prompt J/ψ is produced in a similar way, by com-

[1] The inclusive J/ψ cross-section integrated over p_T (2-10 GeV/c) is not published, but specifically produced for this analysis. The published p_T-integrated value here [20] refers to $p_T > 0$.

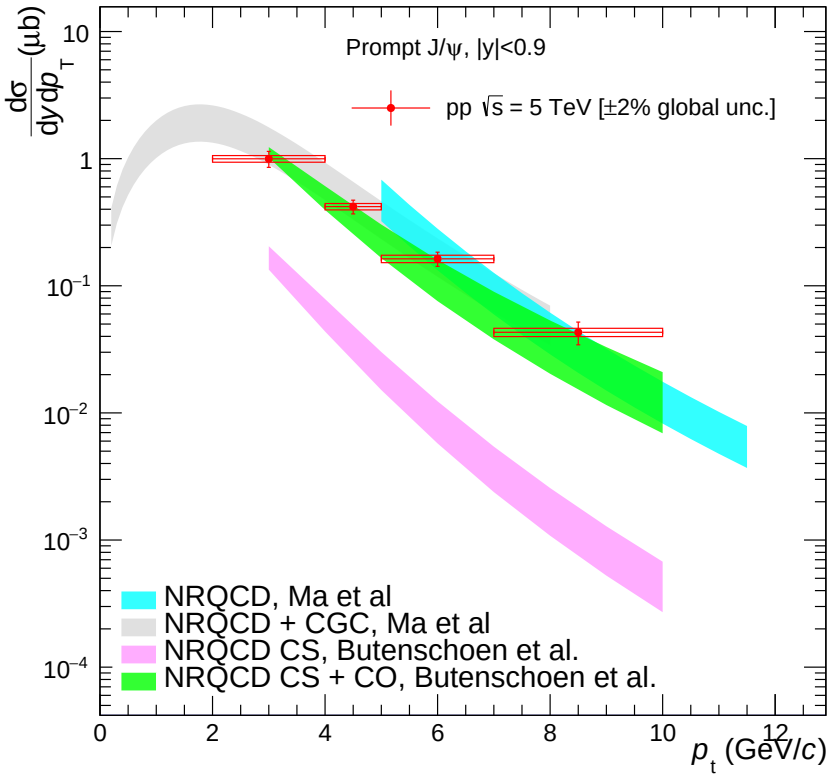

Figure 6.3: $\frac{d^2\sigma_{J/\psi}}{dp_T dy}$ of prompt J/ψ shown as a function of p_T compared to theoretical calculations. The error bars represent the statistical uncertainty and the boxes represent the systematic uncertainty.

bining p_T differential results according to the formula 6.2. For this combination the published values of inclusive J/ψ cross-section have been used. The prompt J/ψ cross-section is shown as a function of p_T in Fig. 6.3, where the error bars (boxes) represent statistical (systematic) uncertainties. The systematic uncertainty on the integrated beam luminosity, determined through the V0 detector, amounts to 2.1% [9], and it is taken as a global uncertainty for the cross-sections. For the p_T integrated case this uncertainty is included in the total systematic error. In opposition, for the p_T-differential cross-section it is not shown (it is correlated among all p_T bins). The results assume no polarization.

The prompt J/ψ cross-section is compared in Fig. 6.3 with several QCD based models, namely:

1. NLO NRQCD calculations from Ma et al. [51] (cyan band).

2. LO NRQCD calculations couple to a Color Glass Condensate (CGC) description of the proton from Ma and Venugopalan [50] (gray band).

3. NLO NRQCD calculations from Butenschoen and Kniehl [28] (green band). For this model also the partial results with only the Color Singlet (CS) contribution are shown (magenta band).

The models shown in Fig. 6.3 seem in general compatible with the results from this analysis over the full p_{T} range. The comparison with CS from Butenschoen and Kniehl suggests that the Color Octet (CO) processes are indispensable to describe the data in the whole measured p_{T} range. It is also worth to point out that the model uncertainties are much larger compared to the uncertainties from data.

6.3 Non-Prompt J/ψ cross-sections

The cross-section of J/ψ from b-hadron decays is obtained using a similar combination as the one discussed for the prompt J/ψ:

$$\sigma_{\mathrm{J}/\psi \leftarrow h_B} = f_{\mathrm{B}} \cdot \sigma_{\mathrm{J}/\psi}\,. \tag{6.2}$$

In the measured region the non-prompt J/ψ cross-section is:

$$\sigma_{\mathrm{J}/\psi \leftarrow h_B}(|y| < 0.9, 2 < p_{\mathrm{T}} < 10\ \mathrm{GeV}/c) \;=\; 0.58 \;\pm\; 0.15 \;\pm\; 0.08\,.$$

Regarding the statistical and systematic uncertainties on the non-prompt J/ψ cross-section, these were obtained using the same procedure followed for prompt J/ψ. This measurement can be compared to theoretical calculations based on the factorization approach, in particular the FONLL model which provides: $0.75^{+0.33}_{-0.24}$. For this calculation CTEQW6.6 [53] PDFs are used, with the theoretical uncertainties coming from varying the factorization and renormalization scales μ_F and μ_B independently in the ranges $0.5 < \mu_F/m_t < 2$, $0.5 < \mu_R/m_t < 2$, with the constraint $0.5 < \mu_F/\mu_R$, where $m_t = \sqrt{p_T^2 + m_b^2}$. The beauty quark mass was varied within $4.5 < m_b < 5.0$ GeV/c^2. The measured value sits in the lower band of FONLL. However, the measured and predicted values are compatible within the uncertainties, which are larger for FONLL compared to data.

The non-prompt J/ψ p_{T}-differential cross-section is shown in Fig.6.4. Due to large statistical uncertainties in the low p_{T} region, the non-prompt J/ψ cross-sections in the two lowest p_{T} bins (2-4 GeV/c and 4-5 GeV/c) have been merged to provide the final result. The error bars and boxes represent statistical and systematic uncertainties, respectively. The p_{T} differential results are compared to FONLL for which the corresponding uncertainty contains the contributions

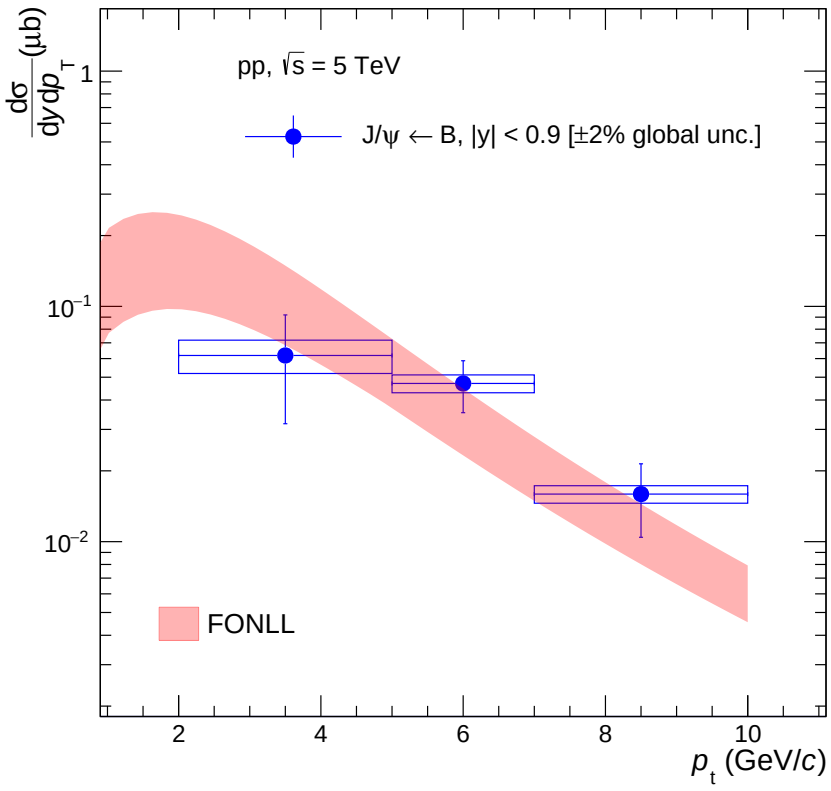

Figure 6.4: $\frac{d^2\sigma_{J/\psi}}{dp_T dy}$ of non-prompt J/ψ shown as a function of p_T compared to FONLL. The error bars represent the statistical uncertainty and the boxes represent the systematic uncertainty.

discussed above. The measurements seems to be compatible with the model, but it should be noted that the uncertainties are quite large, from both data and theoretical prediction sides.

6.4 Conclusions and outlook

The study of prompt and non-prompt J/ψ production in pp collisions at $\sqrt{s}$ = 5 TeV, using the ALICE detector, has been addressed in this thesis. The measurement was performed at mid-rapidity and down to p_T = 2 GeV/c, a kinematic region accessible only by the ALICE detector at the LHC. The results obtained from this analysis nicely complement similar measurements provided by ATLAS and CMS experiments, available at higher p_T, and are found to be compatible within the uncertainties with QCD models that describe the production of open-heavy flavour hadrons and prompt charmonia.

There are some improvements that need to be addressed for the final publication, related to

the systematic uncertainties. In particular for the non-prompt J/ψ x template, PYTHIA Monte Carlo simulations are currently used, but the plan is to use more realistic Monte Carlo simulation based on EvtGen (see details about EvtGen in section 4.3). However, the systematic uncertainty on this specific source is indeed below 1%, so this will not have a real effect on the total systematic uncertainty. For the systematic uncertainty related to the x background, as discussed in section 5.2, a more proper way to account for the correlations among fitted parameters (λ_+, λ_- and $\lambda_{\rm sym}$) will be considered. This is expected to reduce the systematic uncertainty on $F_{\rm Bkg}(x)$, and since it is the largest contribution, the overall systematic uncertainty should be improved as well, especially at low $p_{\rm T}$.

For future work, it is possible to go one step further and extrapolate measured $p_{\rm T}$-integrated non-prompt J/ψ cross-section down to $p_{\rm T}$ = 0. Since the measurements have been performed down to very low $p_{\rm T}$, it is possible to compute the extrapolation factor following the same approach described in [14]. This method relies on some theoretical model predictions, such as FONLL, and the extrapolation factor can be determined with relatively small systematic uncertainties, since most of them (highly correlated with Y and $p_{\rm T}$) cancel out in the extrapolation procedure. Furthermore, by using a similar technique the beauty-quark production cross-sections at mid-rapidity $\left(\left.\frac{{\rm d}\sigma_{\rm b\bar{b}}}{{\rm d}y}\right|_{|y|<0.9}\right)$ and in the total phase-space ($\sigma_{\rm b\bar{b}}$) can be determined down to $p_{\rm T}({\rm b})$ = 0. In particular the former will provide a "reference" measurement for beauty quark production at mid-rapidity in pp at $\sqrt{s}$ = 5 TeV.

Appendix A

Impact parameter and x-resolution studies

In this appendix fit results are reported for: *(i)* impact parameter distributions for single tracks for all data and Monte Carlo samples discussed in this thesis; *(ii)* pseudo-proper decay length resolutions for prompt J/ψ for all p_{T} bins.

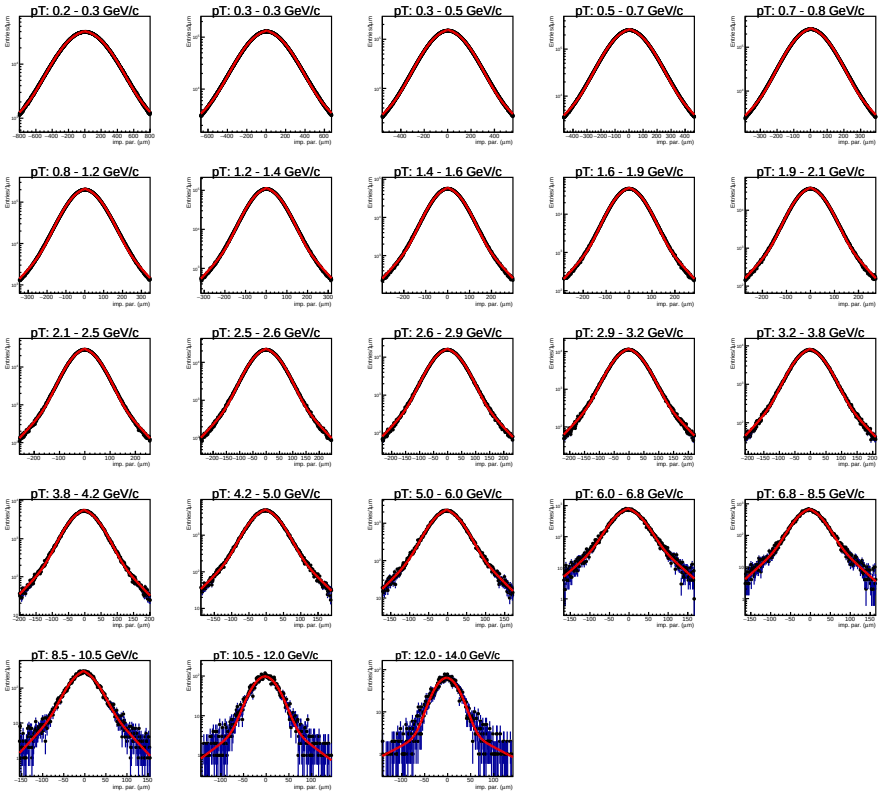

Figure A.1: Impact parameters distributions fitted by a Gaussian plus a symmetric exponential on a range of p_{T} intervals for MC CENT before corrections.

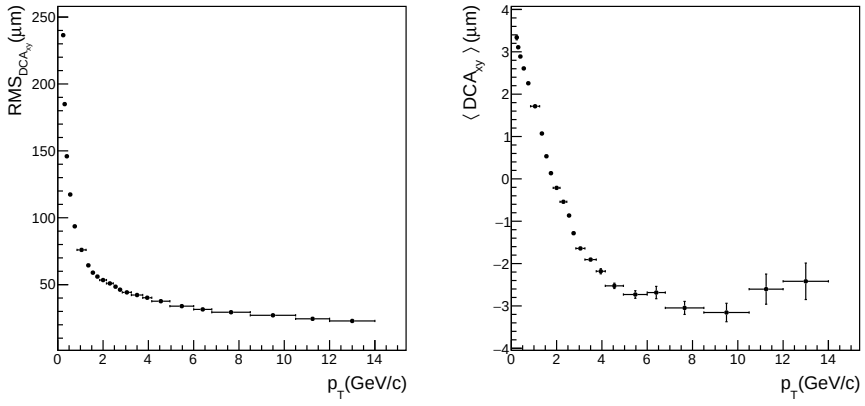

Figure A.2: The single track impact parameter resolutions and averages for the CENT MC sample before DCA corrections. On the left the RMS values versus p_{T}. On the right the averages versus p_{T}.

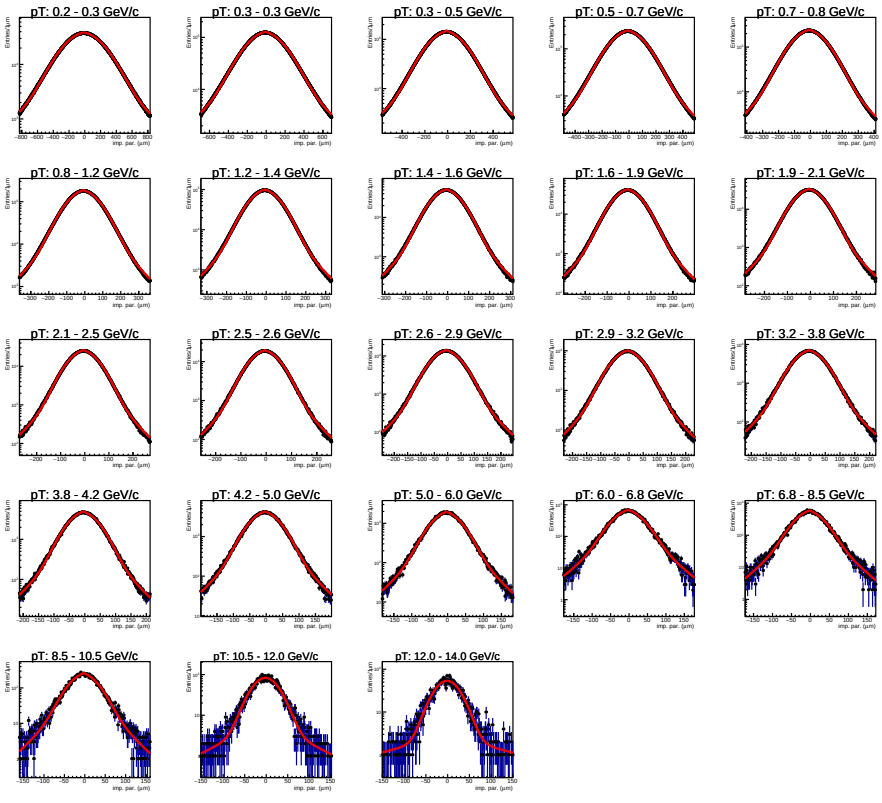

Figure A.3: Impact parameters distributions fitted by a Gaussian plus a symmetric exponential on a range of p_{T} intervals for MC CENT after corrections.

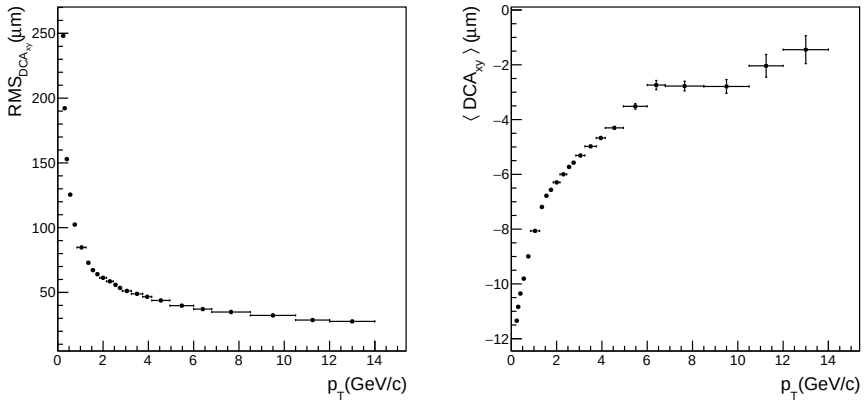

Figure A.4: The single track impact parameter resolutions and averages for the CENT MC sample after DCA corrections. On the left the RMS values versus p_{T}. On the right the averages versus p_{T}.

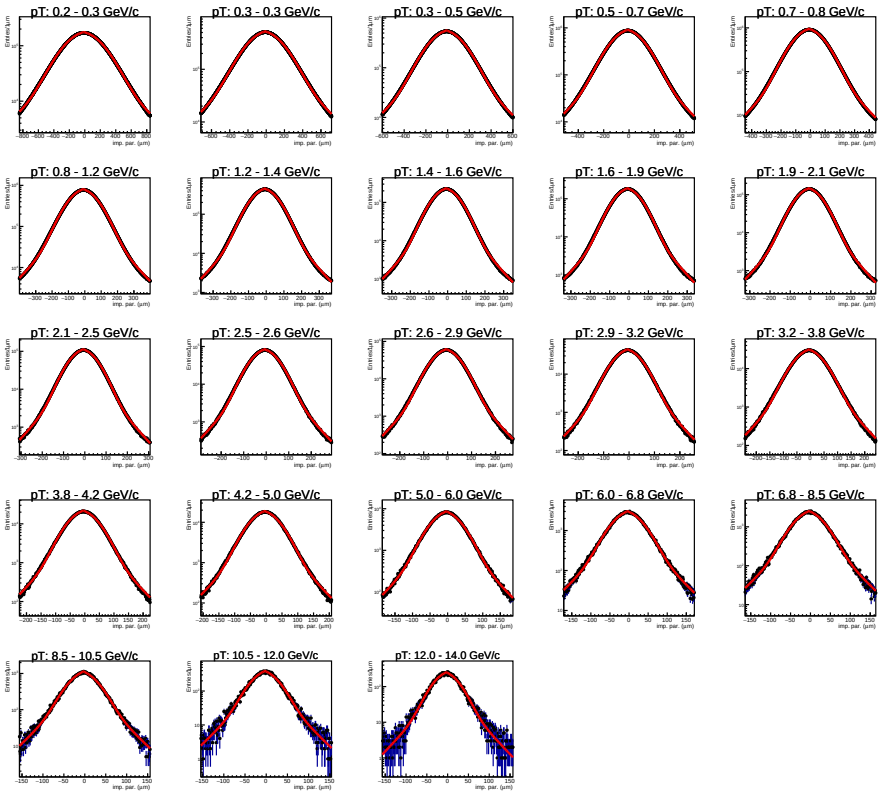

Figure A.5: Impact parameters distributions fitted by a Gaussian plus a symmetric exponential on a range of p_{T} intervals for CENT DATA.

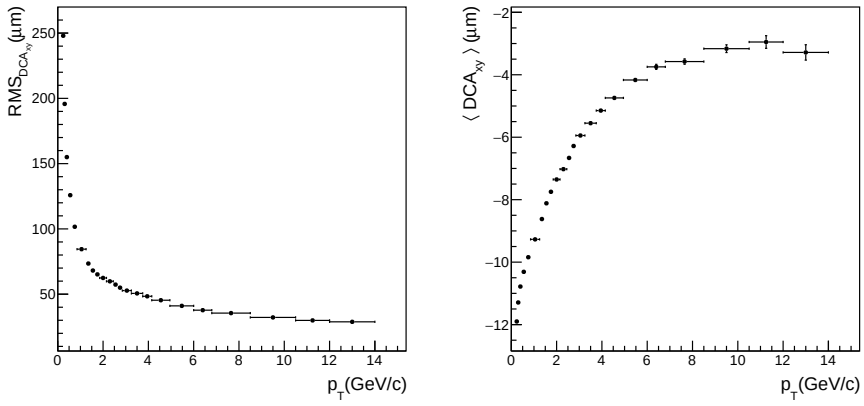

Figure A.6: The single track impact parameter resolutions and averages for the CENT DATA. On the left the RMS values versus p_{T}. On the right the averages versus p_{T}.

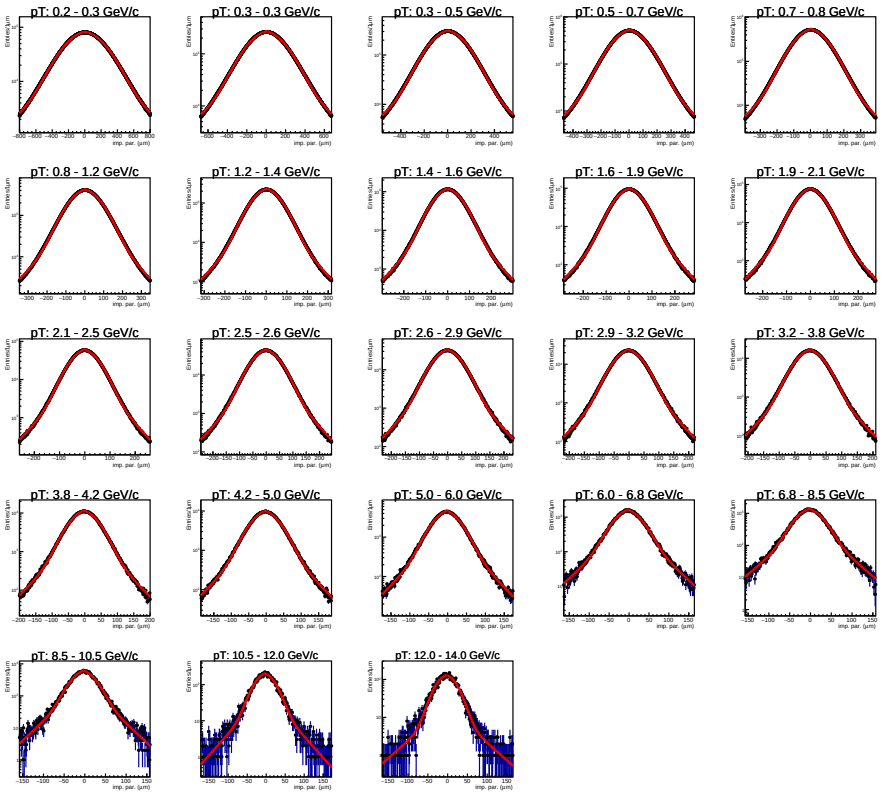

Figure A.7: Impact parameters distributions fitted by a Gaussian plus a symmetric exponential on a range of p_{T} intervals for MC FAST before corrections.

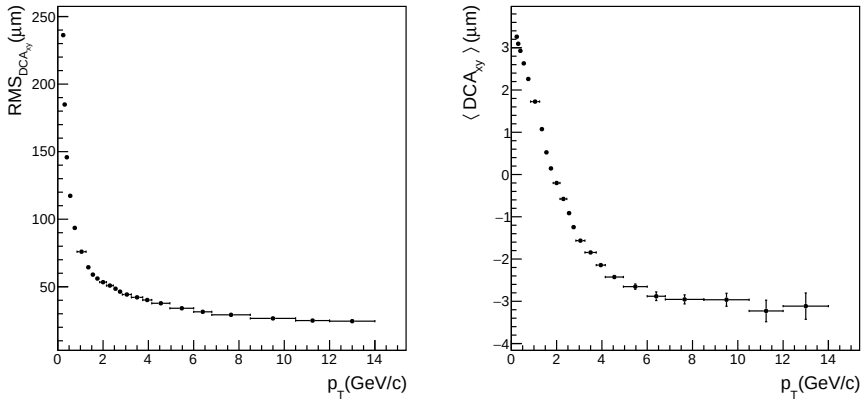

Figure A.8: The single track impact parameter resolutions and averages for the FAST MC sample before DCA corrections. On the left the RMS values versus p_{T}. On the right the averages versus p_{T}.

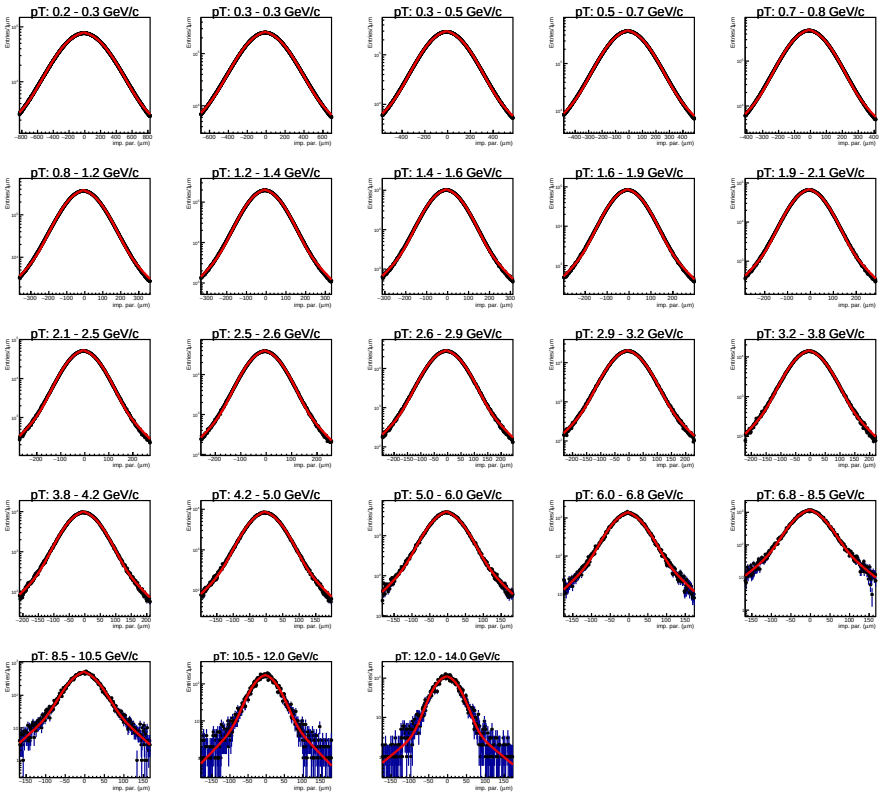

Figure A.9: Impact parameters distributions fitted by a Gaussian plus a symmetric exponential on a range of p_{T} intervals for MC FAST after corrections.

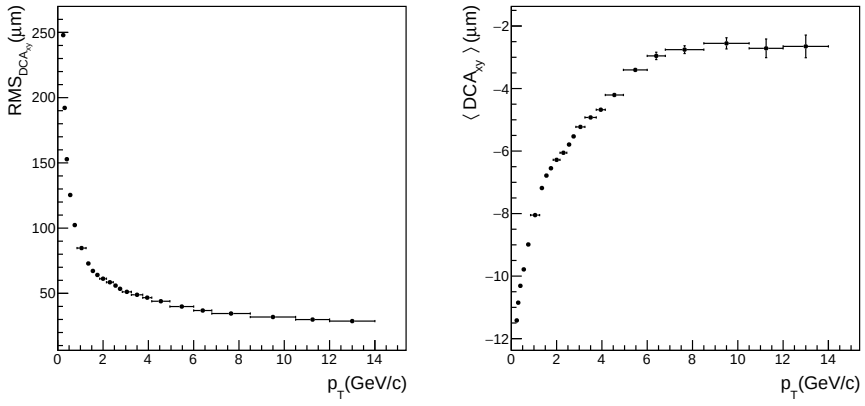

Figure A.10: The single track impact parameter resolutions and averages for the FAST MC sample after DCA corrections. On the left the RMS values versus p_{T}. On the right the averages versus p_{T}.

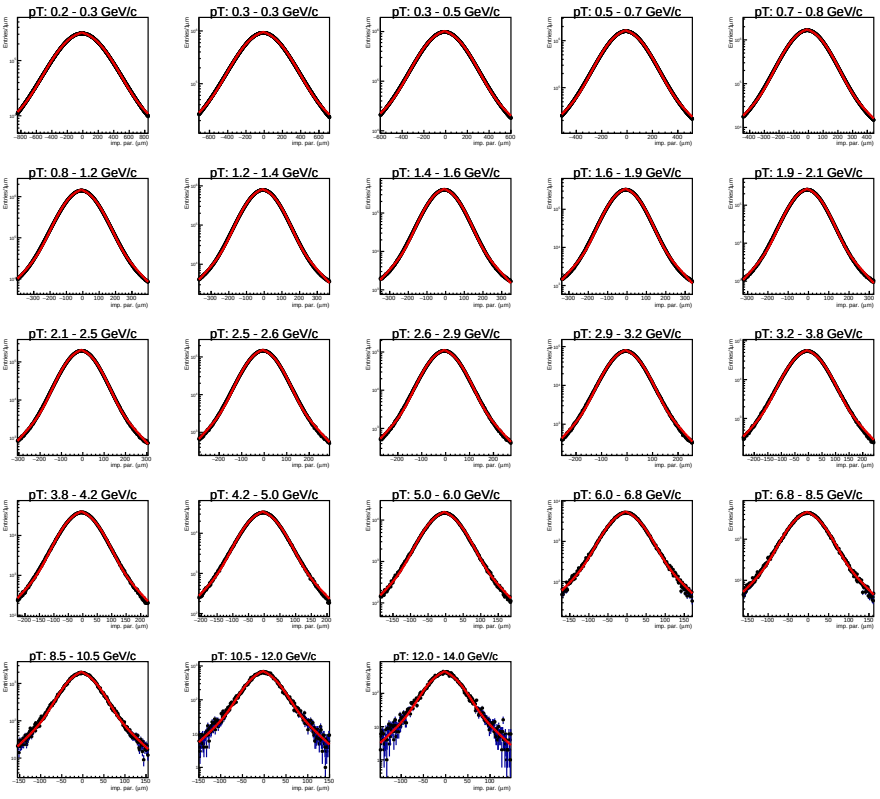

Figure A.11: Impact parameters distributions fitted by a Gaussian plus a symmetric exponential on a range of p_{T} intervals for FAST DATA.

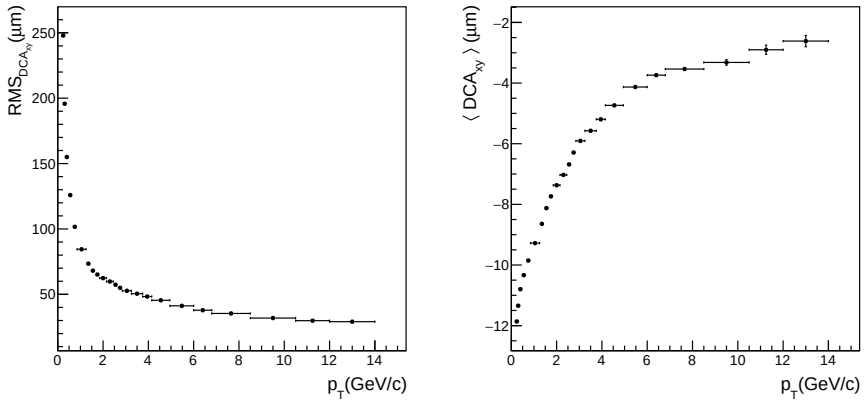

Figure A.12: The single track impact parameter resolutions and averages for the CENT DATA. On the left the RMS values versus p_{T}. On the right the averages versus p_{T}.

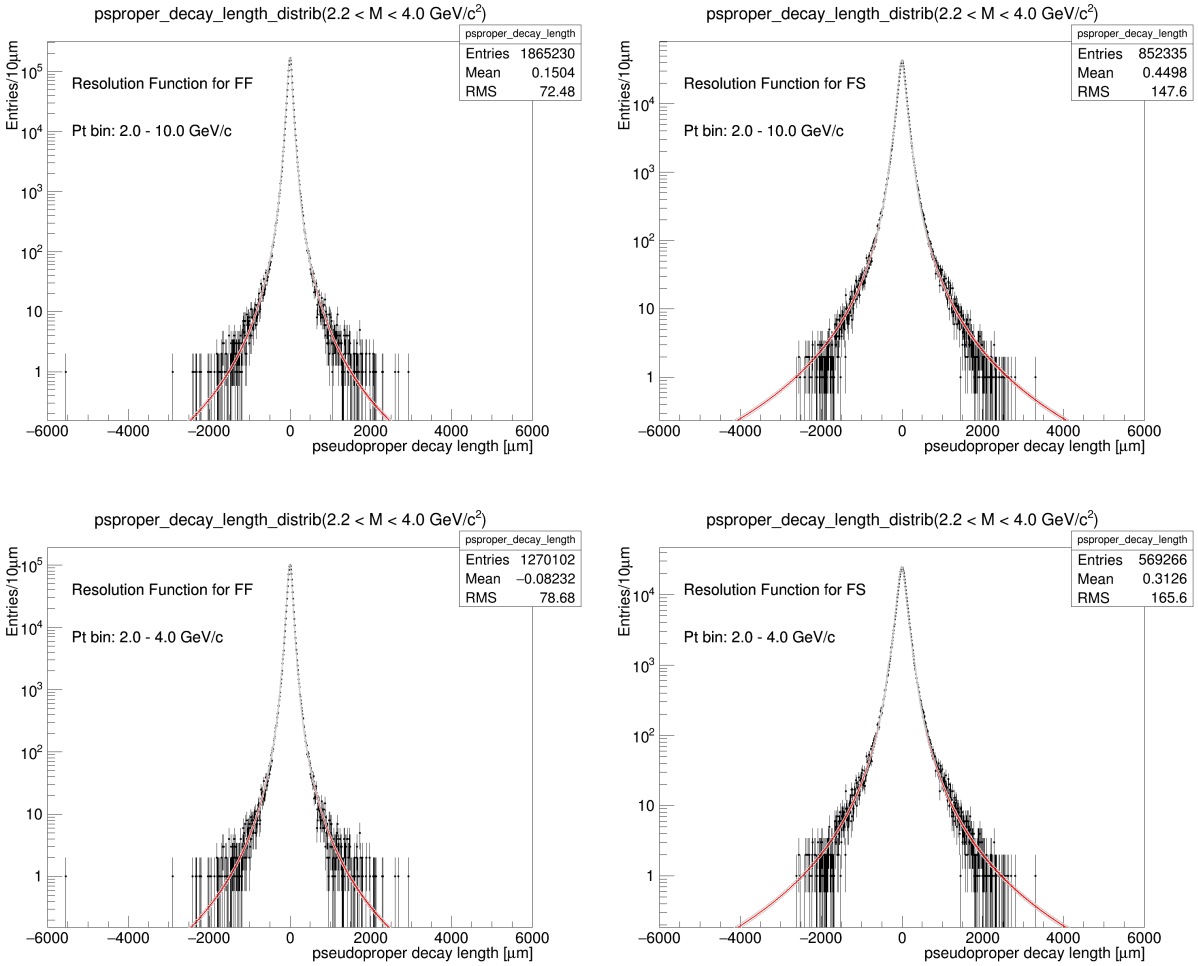

Figure A.13: Resolution function fitted on FF and FS candidates for the integrated case and [2,4] GeV/c.

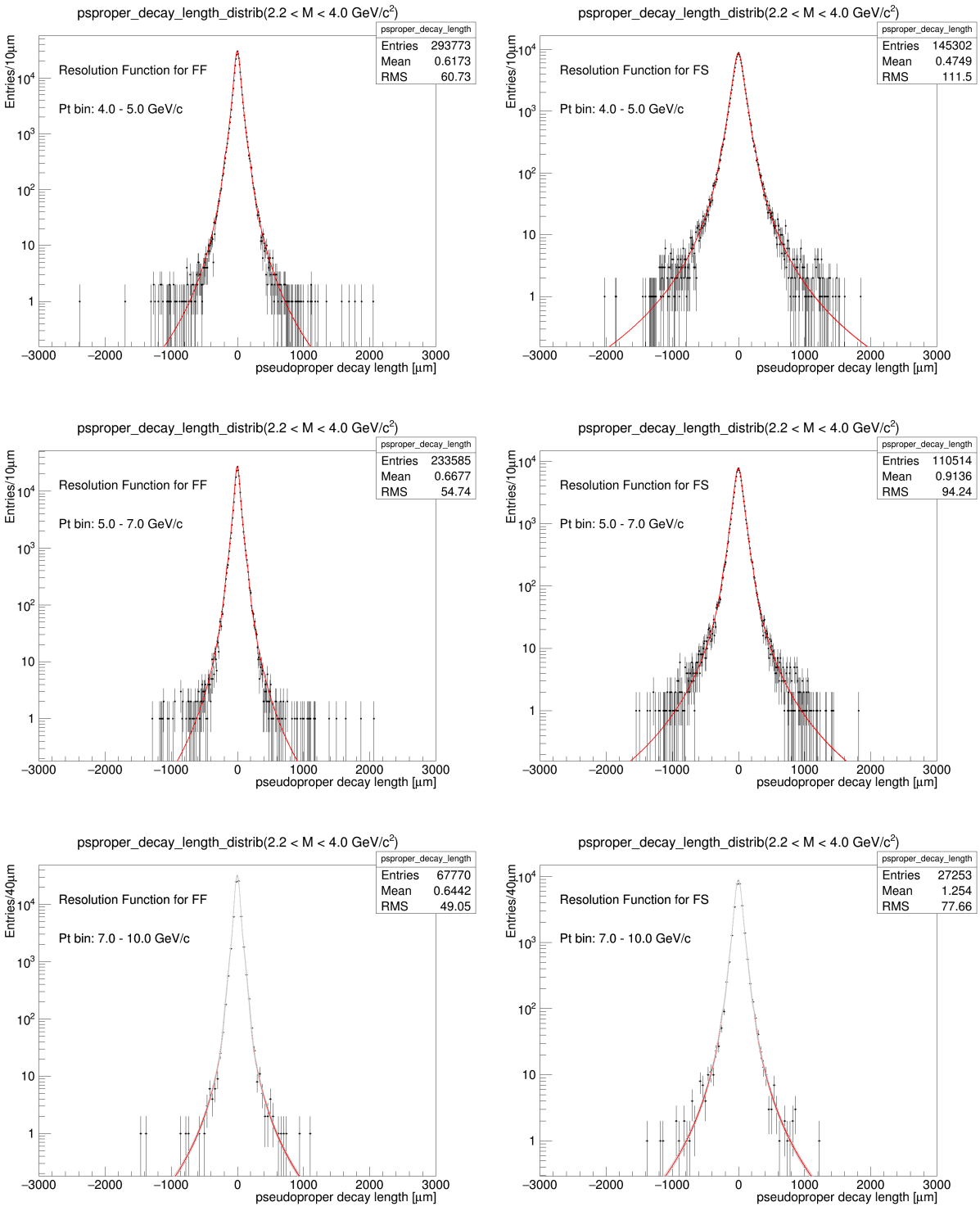

Figure A.14: Resolution function fitted on FF and FS candidates for p_{T} [2,4], [4,5], [5,7] and [7,10] GeV/c.

List of abbreviations

AGS	Alternating Gradient Synchotron
ALICE	A Large Ion Collider Experiment
ATLAS	A Toroidal LHC Apparatus
BNL	Brookhaven National Laboratory
CEM	Color Evaporation Model
CERN	Conseil Européen pour la Recherche Nucléaire
CGC	Color Glass Condensate
CMS	Compact Muon Solenoid
CO	Color-Octet
CP	Charge-Parity
CS	Color-Singlet
CSM	Color-Singlet Model
DCA	Distance of Closest Approach
DGLAP	Dokshitzer-Gribov-Lipatov-Altarelli-Parisi
DPG	Data Preparation Group
DIS	Deep Inelastic Scattering
FF	First-First
FONLL	Fixed-Order Next-To-Leading-Logarithm
FS	First-Second

GM-VFNS	General-Mass Variable-Flavor-Number Scheme
ITS	Inner Tracking System
LDME	Long-Distance Matrix Elements
LHC	Large Hadron Collider
LHCb	Large Hadron Collider beauty
LQCD	Lattice Quantum Chromodynamics
LS	Like-signed
MC	Monte Carlo
MWPC	Multi-Wire-Proportional Chamber
NLO	Next-to-leading-order
NNLO	Next-to-next-to leading order
NRQCD	Non-Relativistic Quantum Chromodynamics
OS	Opposite Sign
PDF	Parton/Probability Distribution Function
PID	Particle Identification
pQCD	Pertubative Quantum Chromodynamics
p_{T}	Transverse momentum
QCD	Quantum Chromodynamics
QED	Quantum Electrodynamics
QGP	Quark Gluon Plasma
RHIC	Relativistic Heavy Ion Collider
RMS	Root Mean Square
RS	Resummation
SDD	Silicon Drift Detector

SPD Silicon Pixel Detector

SPS Super Proton Synchotron

SS Second-Second

SSD Silicon Strip Detector

TOF Time of Flight

TPC Time Projection Chamber

TRD Transition Radiation Detector

Bibliography

[1] Alice data preparation group link. https://twiki.cern.ch/twiki/bin/viewauth/ALICE/AliDPGRunLists. Accessed: 2010-05-30.

[2] Comparisons between alice inclusive psi(2s)-to-j/psi cross section ratio as a function of pt in pp collisions at $\sqrt{s}$=13 tev and nrqcd model calculation. https://alice-figure.web.cern.ch/node/10835. Accessed: 2019-5-25.

[3] Evtgen. https://evtgen.hepforge.org/. Accessed: 2019-5-7.

[4] Geant3. https://cds.cern.ch/record/118715?ln=en. Accessed: 2019-6-7.

[5] Photos. http://photospp.web.cern.ch/photospp/. Accessed: 2019-5-7.

[6] Pythia. http://home.thep.lu.se/~torbjorn/Pythia.html. Accessed: 2019-5-7.

[7] Qgpphysics. https://www.physi.uni-heidelberg.de/~reygers/lectures/2015/qgp/qgp2015_06_space_time_evo.pdf. Accessed: 2019-5-19.

[8] Tpc-de/dx distribution as a function of momentum for charged particles in pb-pb collisions at $\sqrt{s}_{NN} = 5.02 tev$. https://alice-figure.web.cern.ch/node/13562. Accessed: 2019-6-1.

[9] ALICE 2017 luminosity determination for pp collisions at $\sqrt{s}$ = 5 TeV. Nov 2018.

[10] M. Aaboud et al. Measurement of quarkonium production in proton–lead and proton–proton collisions at 5.02 tev with the atlas detector. *The European Physical Journal C*, 78(3):171, Feb 2018.

[11] Georges Aad et al. Measurement of the differential cross-sections of inclusive, prompt and non-prompt J/ψ production in proton-proton collisions at $\sqrt{s}$ = 7 TeV. *Nucl. Phys.*, B850:387–444, 2011.

[12] K. Aamodt et al. Rapidity and transverse momentum dependence of inclusive J/ψ production in pp collisions at $\sqrt{s}$ = 7 TeV. *Phys. Lett.*, B704:442–455, 2011. [Erratum: Phys. Lett.B718,692(2012)].

[13] B. Abelev et al. Measurement of electrons from beauty hadron decays in pp collisions at $\sqrt{s}$ = 7 tev. *Physics Letters B*, 721(1):13 – 23, 2013.

[14] Betty Abelev et al. Measurement of prompt J/ψ and beauty hadron production cross sections at mid-rapidity in pp collisions at $\sqrt{s}$ = 7 TeV. *JHEP*, 11:065, 2012.

[15] Betty Bezverkhny Abelev et al. Measurement of quarkonium production at forward rapidity in pp collisions at $\sqrt{s}$ = 7 TeV. *Eur. Phys. J.*, C74(8):2974, 2014.

[16] Betty Bezverkhny Abelev et al. Performance of the ALICE Experiment at the CERN LHC. *Int. J. Mod. Phys.*, A29:1430044, 2014.

[17] H. Abramowicz et al. Combination of measurements of inclusive deep inelastic $e^{\pm}p$ scattering cross sections and QCD analysis of HERA data. *Eur. Phys. J.*, C75(12):580, 2015.

[18] S. Acharya et al. Measurement of the inclusive J/ ψ polarization at forward rapidity in pp collisions at $\sqrt{\mathbf{s}}$ = **8** TeV. *Eur. Phys. J.*, C78(7):562, 2018.

[19] Shreyasi Acharya et al. Energy dependence of forward-rapidity J/ψ and ψ(2S) production in pp collisions at the LHC. *Eur. Phys. J.*, C77(6):392, 2017.

[20] Shreyasi Acharya et al. Inclusive J/ψ production at mid-rapidity in pp collisions at $\sqrt{s}$ = 5.02 TeV. 2019.

[21] Shreyasi Acharya et al. Measurement of D^0 , D^+ , D^{*+} and D_s^+ production in pp collisions at $\sqrt{s}$ = 5.02 TeV with ALICE. *Eur. Phys. J.*, C79(5):388, 2019.

[22] D. Acosta et al. Measurement of the j/ψ meson and b-hadron production cross sections in $p\overline{p}$ collisions at $\sqrt{s}$ = 1960 GeV. *Phys. Rev. D*, 71:032001, Feb 2005.

[23] D. Acosta et al. Measurement of the J/ψ meson and $b-$hadron production cross sections in $p\bar{p}$ collisions at $\sqrt{s}$ = 1960 GeV. *Phys. Rev.*, D71:032001, 2005.

[24] R. Baier and R. Ruckl. Hadronic Collisions: A Quarkonium Factory. *Z. Phys.*, C19:251, 1983.

[25] Richard D. Ball et al. Parton distributions from high-precision collider data. *Eur. Phys. J.*, C77(10):663, 2017.

[26] H. Bethe. Zur theorie des durchgangs schneller korpuskularstrahlen durch materie. *Annalen der Physik*, 397(3):325–400, 1930.

[27] F. Bossu, Z. Conesa del Valle, A. de Falco, M. Gagliardi, S. Grigoryan, and G. Martinez Garcia. Phenomenological interpolation of the inclusive J/ψ cross section to proton-proton collisions at 2.76 TeV and 5.5 TeV. 2011.

[28] Mathias Butenschoen and Bernd A. Kniehl. Reconciling J/ψ production at HERA, RHIC, Tevatron, and LHC with NRQCD factorization at next-to-leading order. *Phys. Rev. Lett.*, 106:022003, 2011.

[29] Matteo Cacciari, Stefano Frixione, and Paolo Nason. The p(T) spectrum in heavy flavor photoproduction. *JHEP*, 03:006, 2001.

[30] Matteo Cacciari, Mario Greco, and Paolo Nason. The P(T) spectrum in heavy flavor hadroproduction. *JHEP*, 05:007, 1998.

[31] Serguei Chatrchyan et al. Performance of CMS muon reconstruction in pp collision events at $\sqrt{s} = 7$ TeV. *JINST*, 7:P10002, 2012.

[32] A. Chodos, R. L. Jaffe, K. Johnson, C. B. Thorn, and V. F. Weisskopf. New extended model of hadrons. *Phys. Rev. D*, 9:3471–3495, Jun 1974.

[33] The ALICE Collaboration. The ALICE experiment at the CERN LHC. *Journal of Instrumentation*, 3(08):S08002–S08002, aug 2008.

[34] The ATLAS Collaboration. The ATLAS experiment at the CERN large hadron collider. *Journal of Instrumentation*, 3(08):S08003–S08003, aug 2008.

[35] The ATLAS collaboration. Measurement of the differential non-prompt J/ψ production fraction in s = 13 TeV pp collisions at the ATLAS experiment. 2015.

[36] The CMS Collaboration. The CMS experiment at the CERN LHC. *Journal of Instrumentation*, 3(08):S08004–S08004, aug 2008.

[37] The LHCb Collaboration. The LHCb detector at the LHC. *Journal of Instrumentation*, 3(08):S08005–S08005, aug 2008.

[38] P Cortese et al. ALICE: Physics performance report, volume I. *J. Phys.*, G30:1517–1763, 2004.

[39] David d'Enterria, Peter Z. Skands, S Alekhin, Andrea Banfi, S Bethke, Johannes Bluemlein, K G. Chetyrkin, D d'Enterria, G Dissertori, X Garcia i Tormo, A H. Hoang, M Klasen, T Klijnsma, S Kluth, J L. Kneur, B A. Kniehl, D W. Kolodrubetz, J Kühn, P Mackenzie, and I W. Stewart. High-precision α_s measurements from lhc to fcc-ee. 12 2015.

[40] B Abelev et al and. Technical design report for the upgrade of the ALICE inner tracking system. *Journal of Physics G: Nuclear and Particle Physics*, 41(8):087002, jul 2014.

[41] Pietro Faccioli, Carlos Lourenço, João Seixas, and Hermine K Wöhri. Study of $\psi\prime$ and χc decays as feed-down sources J/ψ hadro-production. *Journal of High Energy Physics*, 2008(10):004–004, oct 2008.

[42] Harald Fritzsch. Producing heavy quark flavors in hadronic collisions—' A test of quantum chromodynamics. *Physics Letters B*, 67(2):217 – 221, 1977.

[43] R. Fruhwirth. Application of Kalman filtering to track and vertex fitting. *Nucl. Instrum. Meth.*, A262:444–450, 1987.

[44] Francois Gelis, Edmond Iancu, Jamal Jalilian-Marian, and Raju Venugopalan. The Color Glass Condensate. *Ann. Rev. Nucl. Part. Sci.*, 60:463–489, 2010.

[45] Grazzini, Massimiliano, Ilnicka, Agnieszka, and Spira, Michael. Higgs boson production at large transverse momentum within the smeft: analytical results. *Eur. Phys. J. C*, 78(10):808, 2018.

[46] F. Halzen and Alan D. Martin. *QUARKS AND LEPTONS: AN INTRODUCTORY COURSE IN MODERN PARTICLE PHYSICS*. 1984.

[47] B. A. Kniehl, G. Kramer, I. Schienbein, and H. Spiesberger. Collinear subtractions in hadroproduction of heavy quarks. *Eur. Phys. J.*, C41:199–212, 2005.

[48] B. A. Kniehl, G. Kramer, I. Schienbein, and H. Spiesberger. Inclusive Charmed-Meson Production at the CERN LHC. *Eur. Phys. J.*, C72:2082, 2012.

[49] Michael Krämer. Quarkonium production at high-energy colliders. *Prog. Part. Nucl. Phys.*, 47:141–201, 2001.

[50] Yan-Qing Ma and Raju Venugopalan. Comprehensive Description of J/ψ Production in Proton-Proton Collisions at Collider Energies. *Phys. Rev. Lett.*, 113(19):192301, 2014.

[51] Yan-Qing Ma, Kai Wang, and Kuang-Ta Chao. $J/\psi(\psi')$ production at the Tevatron and LHC at $\mathcal{O}(\alpha_s^4 v^4)$ in nonrelativistic QCD. *Phys. Rev. Lett.*, 106:042002, 2011.

[52] A.D. Martin, R.G. Roberts, W James Stirling, and R.S. Thorne. Nnlo global parton analysis. *Physics Letters B*, 531:216–224, 04 2002.

[53] Pavel M. Nadolsky, Hung-Liang Lai, Qing-Hong Cao, Joey Huston, Jon Pumplin, Daniel Stump, Wu-Ki Tung, and C. P. Yuan. Implications of CTEQ global analysis for collider observables. *Phys. Rev.*, D78:013004, 2008.

[54] E. Norrbin and T. Sjöstrand. Production and hadronization of heavy quarks. *The European Physical Journal C - Particles and Fields*, 17(1):137–161, Oct 2000.

[55] Albert M Sirunyan et al. Measurement of prompt and nonprompt J/ψ production in pp and pPb collisions at $\sqrt{s_{\mathrm{NN}}} = 5.02\,\mathrm{TeV}$. *Eur. Phys. J.*, C77(4):269, 2017.

[56] M. Tanabashi et al. Review of particle physics. *Phys. Rev. D*, 98:030001, Aug 2018.